

# Structural order and thermal disorder at selected crystal surfaces: theory and simulations

Daniele Passerone

October 1998



# Contents

<b>1</b>	<b>Introduction</b>	<b>1</b>
1.1	Outline . . . . .	2
<b>2</b>	<b>Surface simulations with MD: technical</b>	<b>7</b>
2.1	The glue potentials . . . . .	9
2.2	Single-step PBC . . . . .	11
2.3	Algorithm for extracting step profiles . . . . .	12
2.4	An algorithm for detecting and classifying holes and islands . .	13
<b>3</b>	<b>Vicinals, faceting and its precursors</b>	<b>17</b>
3.1	The Au(100) surface . . . . .	17
3.2	The single step on a Au(100) surface: non-standard PBC . . . . .	24
3.2.1	Simulation of ( $K11$ ) vicinals of (100) . . . . .	24
3.3	Vicinals of Au(100) simulated with a single step . . . . .	25
3.3.1	Surface density . . . . .	26
3.4	Interplay between reconstruction and step . . . . .	29
3.5	The shrinking of a terrace with retraction of a step . . . . .	32
3.6	The ( $53\ 1\ 1$ ) vicinal . . . . .	38
3.6.1	Example of evolution at 970 K and at 1250 K . . . . .	39
3.7	Higher step density: the ( $17\ 1\ 1$ ) vicinal surface . . . . .	42
3.7.1	Reconstruction-induced faceting: experimental review .	43
3.7.2	Simulation of vicinal surfaces . . . . .	46
<b>4</b>	<b>The Grand Canonical Monte Carlo method applied to surfaces</b>	<b>53</b>
4.1	Introduction . . . . .	53
4.2	Algorithm . . . . .	54
4.3	Proposal matrix and detailed balance . . . . .	55

4.4	Implementation of the GC algorithm . . . . .	58
4.5	Demonstration of the method . . . . .	59
4.5.1	Reconstruction of Au(110) . . . . .	59
4.5.2	Hexagonal reconstruction of Au(100) . . . . .	61
4.5.3	High temperature GCMC simulation for metals. Equi- libration problems . . . . .	65
<b>5</b>	<b>The Ar(111) surface. Preroughening and surface melting</b>	<b>67</b>
5.1	LJ systems and Grand Canonical simulations . . . . .	67
5.2	Results . . . . .	71
5.3	Growth on a substrate . . . . .	75
<b>6</b>	<b>Adsorption-induced deconstruction</b>	<b>83</b>
6.1	Experimental framework . . . . .	83
6.2	MD simulations . . . . .	88
6.2.1	Microscopic details of crater formation . . . . .	89
6.2.2	Homogeneous island nucleation . . . . .	97
6.2.3	Details of deconstruction under an island . . . . .	97
6.3	Connection with the step correlation length $\xi$ . . . . .	98
<b>7</b>	<b>Theory of variable curvature MD</b>	<b>105</b>
7.1	Introduction . . . . .	105
7.2	Theory . . . . .	107
7.2.1	Lagrangian . . . . .	109
7.2.2	Construction of the $\hat{H}$ matrix . . . . .	110
7.2.3	Explicit form of the equations of motion . . . . .	111
7.2.4	Constrained molecular dynamics and PBC . . . . .	114
7.3	Phenomenology of a bent plate . . . . .	116
7.4	Application to metal surfaces . . . . .	119
7.4.1	Implementation . . . . .	119
7.4.2	A clean surface: change of surface stress with recon- struction . . . . .	121
7.4.3	Change of surface stress with adsorption . . . . .	124
7.5	Conclusions . . . . .	125
7.5.1	The velocity Verlet as a predictor-corrector. . . . .	128

---

7.5.2	The bent plate case. . . . .	128
<b>8</b>	<b>Molecular crystals: theory of surface rotational disordering</b>	<b>131</b>
8.1	Free energy, mean field and results . . . . .	134
<b>9</b>	<b>Summary</b>	<b>141</b>



# Chapter 1

## Introduction

Surface physics has become in the last decades a more and more mature field of research; phenomena occurring at surfaces are often practical realizations of important theories, universality classes of statistical mechanics are physically realized (*e.g.*, the roughening transition in the KT universality class) and modern theories such as the renormalization group theory find their application in interface phenomena (for a review on phase transitions at surfaces, see *e.g.* [1]). Experimental techniques such as STM and photoelectron emission allow detailed inspection in surface structure, and all diffraction techniques have reached a remarkable level of technical depth.

Molecular Dynamics (MD) simulation techniques based on classical, empirical potentials have been increasingly used, though ab-initio Car Parrinello (CP) MD extended its power at the same pace of computational resources growth. CP simulation has the advantage of allowing very realistic predictions and of providing quantitative results about electronic structure, chemical interactions and modifications, but (at least at the present state of the art) has no chance with systems composed by a very large number of particles (*i.e.* more than  $\sim 1000$  atoms) and for true evolutions longer than a few picoseconds due to the

excessive computer resources required. Surface physics is a typical field where classical simulation work can still bring its contribution: collective phenomena can be studied, high temperature simulations allow the study of phase transitions, large systems can be used to investigate the role of steps, islands and craters in structural phase transitions, growth and re-ordering; moreover, non-standard geometries can be used for an efficient reproduction of experimental techniques, and new experiments can be suggested by the simulations.

In this thesis, we would like to present a set of studies of a variety of physical phenomena occurring at surfaces. The thorough comprehension of these phenomena, both on the microscopic and on the macroscopic side, requires various theoretical models and simulation techniques, which will be presented throughout this work. Physical situations we have encountered include steps formation and evolution, reconstruction and deconstruction, islands and craters growth, strain and stress and their interplay with surface structure, faceting, orientational and positional disordering, surface melting.

## 1.1 Outline

Several different computational methods and models have been widely used in this work. In particular, the tools of classical molecular dynamics (MD) and classical Monte Carlo (MC) have been adapted to the different physical situations we have dealt with, and new methods of simulation have been introduced and developed; therefore, part of the thesis is devoted to the description of these methods.

For what concerns MD, odd periodic boundary conditions simulations (PBC) have been implemented and applied to stepped surfaces.

A new simulation scheme, which treats the curvature of a slab as a separate degree of freedom has been developed, and the surface stress dependence of structural properties has been studied.

An original scheme for off-lattice Monte Carlo simulations, applied to surfaces in the Grand Canonical ensemble, has been recently developed in our group. The systems for which this system has been applied are Lennard-Jones crystals, both semi-infinite and adsorbed on a substrate, and metal surfaces subject to reconstruction. In both cases the method has shown to be powerful. At

the technical level, particular care has been required in the balance between diffusive moves and grand canonical atom creation/destruction moves, and in the strategies for improving the acceptance rate of the latter.

Several physical systems and situations have been studied in this work; in the remainder of this introduction they will be listed in their order of appearance in later chapters.

Chapter 2 is devoted to MD simulation techniques and models of interatomic forces. In particular, the handling of many body ‘glue’ potentials, suitable for metals, in particular for a noble metal like gold, are briefly introduced.

In Chapter 3 we study step bunching as a precursor to surface faceting in a reconstructed surface. Au (100), which is our chosen example, undergoes a deconstruction transition from quasihexagonal to disordered  $T_d = 1173 K$ . According to X-Ray diffraction measurements, a  $(m\ 1\ 1)$  surface, miscut by an angle  $\theta = \arctan\left(\frac{\sqrt{2}}{m}\right)$  with respect to the flat (100), is unstable against faceting below a particular temperature  $T_f$  which depends on  $\theta$  with a power law  $T_d - T_f = \theta^{1/\gamma}$ , where  $T_d$  is the deconstruction temperature of the (100) flat surface and  $\gamma$  is an exponent  $\simeq 0.44$ . We have studied the microscopic precursors of this kind of faceting by MD simulation, and find that it consists of step bunching taking place on the time scale of ns. Moreover, we have speculated on the possible interplay between the exponent  $\gamma$  and the nature of the deconstructed phase: the exponent  $\gamma$  is found to be incompatible either with a flat deconstructed surface or with a rough surface; this fact suggests the possibility of a disordering transition of the flat (100) to a DOF (prerough) phase.

In Chapter 4 we present a realistic Monte Carlo simulation of surfaces in the Grand Canonical ensemble. Technical details of this method, together with suggested improvements to its efficiency, are presented.

The applicability of the grand canonical method in structural phase transitions involving strong changes in the lateral density of metal surfaces is also tested and demonstrated in two well-known cases: the square-to-hexagonal transition of the Au (100) and the  $(1 \times 1)$ -to-missing row reconstruction of the Au (110). We have also tried to use this method to understand the nature of the high temperature hex-square disordering. The results are still partly contradictory, and this remains an open problem.

In Chapter 5 we describe its application, carried out in our group, to reentrant

layering in rare gas multilayer deposition on a substrate, as well as the free surface of a rare gas solid. (111) Lennard-Jones surface, chosen as a model for rare gas surface, was investigated; both the free surface and the substrate adsorption case were studied. In the former case, clear evidence for a preroughening transition was found, with layer occupancies very close to one half at a temperature in good agreement with experimental observations concerning Argon. In the latter case, reentrant layering transitions at half occupancy are found, again in agreement with the experiments. The most important result is the confirmation that a preroughening transition is indeed at the origin of reentrant layering. However, we also found that melting of the top layer occurs at preroughening. The low preroughening temperature of these surfaces may therefore be a consequence of that.

In Chapter 6 we study adsorption-induced deconstruction. The study is inspired by experimental work concerning adsorption of molecules on the surface of reconstructed metals. As well as by homoepitaxial growth, which is the case addressed by our simulations. In particular, the formation mechanism of islands and craters on the hex-reconstructed surface can be answered using temperature as a driving force for density changes; the microscopic details of interplay between islands (and holes) formation and reconstruction is elucidated, and the role of the structural transformation in the nonlinear growth rate dependence upon coverage, recently found by King [2], is discussed.

In Chapter 7 a new variable curvature slab MD scheme is presented. The development of this technique is, perhaps, the most important original contribution in this thesis, especially because of its immediate applicability to real physical situations. We show that the method is very accurate in determining the surface stress differences, as tested with differently reconstructed surfaces, and checked against the standard Kirkwood-Buff [3] formula. The results are encouraging. Surface stress of adsorbate-covered surfaces is a strong function of coverage. In a simple case, we show that the method can be also applied to heterogeneous systems (in our case Pb covered Au surfaces are used for demonstration).

In addition to ‘quasi static’ properties of bending systems, *i.e.* equilibrium curvature and surface stress, variable curvature MD allows to reproduce efficiently the dynamics of strain induced phenomena such as deconstruction. As an example, we have started the study of Au(111) strain induced deconstruc-

tion, but we do not report on it in this work, although preliminary results are encouraging.

The rotational disordering transition of the surface of a molecular crystals has been studied with the methods of statistical mechanics. A layer-dependent mean field theory has been used in Chapter 8 in order to study the rotational disordering of a  $C_{60}$  (111) surface, occurring experimentally at about 0.9 the corresponding bulk disordering temperature.

*The material collected in this thesis is partly published or being published in [4] (Chapter 3), [5, 6] (Chapter 5), [7] (Chapter 8) and [8] (Chapter 7).*



# Chapter 2

## Surface simulations with MD: technical

In the studies presented in the following chapters, we have made a large use of computer simulations, hence we will give here a brief description of the methods we have used.

In most cases we have performed classical molecular dynamics (MD) simulations, *i.e.* we have integrated numerically the Newton equations of motion, discretizing them in time steps  $\Delta t$ . This choice is motivated by the necessity to deal with a large number of atoms and for long simulation times. Other descriptions, like the *ab-initio* method introduced by Car and Parrinello [9], are both more fundamental and more accurate, but not yet suitable for calculations with a number of particles of the order  $\sim 10000$ , or for simulation times of the order of  $\sim 1$  ns.

The kinetic energy of the system is obviously  $K = 1/2 \sum_i m_i v_i^2$ , while the potential energy depends on the interatomic potential chosen. The most popular interaction for MD simulations is probably the 6-12 Lennard-Jones potential (LJ), which is pairwise and easy to use from a computational point of view. It is

of the form:

$$\phi(r) = 4\varepsilon \left( \left( \frac{\sigma}{r} \right)^{12} - \left( \frac{\sigma}{r} \right)^6 \right) \quad (2.1)$$

where  $\varepsilon$  sets the energy scale, while  $\sigma$  sets the length scale. It is well known that this pair potential describes moderately well the behavior of noble gases, for which it was conceived. The  $1/r^6$  term should account for the van der Waals attraction typical of filled-shell atoms, while the other term is just a repulsive barrier, expressed in a convenient form.

For metals the  $LJ$  potential is inappropriate. For them we will use many body potentials of the **glue**, or EAM type, introduced by Daw and Baskes [10], Finnis and Sinclair [11], and by Ercolessi *et al.* [12, 13](see § 2.1).

Accurate parameterizations of the glue model have been constructed chiefly for Au [13], Al [14], and to a lesser degree Pb [15].

To describe bulk systems we have used the common technique of the periodic boundary conditions (PBC).

In the simulation of free surfaces we use the *slab* geometry, i.e. we use PBC only in the  $x - y$  directions. In the  $z$  direction the atoms on the top surface are free and in contact with the vacuum. On the bottom face the atoms in the first few layers are usually kept fixed to mimic the influence of a (solid) bulk.

The precise number of fixed layers and of mobile layers depends on the range of the potential used, on the size and orientation and on the physical problem to be studied.

Bulk thermal expansion is mimicked by expanding the in-plane size of the cell and the rigid bottom layers, as a function of the temperature, following a previously obtained thermal expansion curve.

The MD algorithm we have used is able to perform: constant energy calculations; constant temperature simulations, via velocity rescaling; and constant-stress simulations, following the Parrinello-Rahman scheme [16]. In the latter the cell is allowed to deform changing in volume and shape. This last approach, in zero-pressure condition, was used mainly in the determination of the optimal lattice spacing  $a$  of a crystal at various temperatures. We used the results obtained from these simulations to perform finite temperature calculations.

In the free surface simulations with the slab geometry, the samples are initially equilibrated at low temperature, room temperature or below, and then brought when necessary at higher temperatures, near to the melting point  $T_m$

via a protocol of further equilibrations at intermediate temperatures. This is necessary to allow the lattice, and particularly the top-most planes, to relax to equilibrium. An excessively fast heating may introduce spurious defects, or collective modes in the slab which are difficult to eliminate once started. For further details the reader is addressed to [17, 18].

## 2.1 The glue potentials

The inability of pair potentials to describe bulk metals is well known. For instance all the two-body potentials satisfy the Cauchy relation  $C_{12} = C_{44}$ , between two of the elastic constants in a cubic crystal, while in noble metals  $C_{12}/C_{44} > 1$  and often of the order of 2-3. The vacancy formation energy  $E_v^F$  and cohesive energy  $E_c$  are very similar in a pair potential, while in noble metals  $E_c$  is 3 to 4 times bigger than  $E_v^F$  [19, 13].

Problems are even more dramatic at surfaces: two-body potentials are unable to model the *contraction* of interatomic distances typical of most metal surfaces (and often giving rise to reconstruction), and usually predict *expansions*.

This and other similar considerations suggested that much better potentials for metals could be constructed by introducing a *local* many-body term to account for the electronic cohesion [10]. Noble and near-noble metals have broad  $d$  bands for which the optimal bonding energy is obtained by maximizing the coordination rather than re-hybridizing to form directional bonds, as in  $sp$ -bonded material. Hence the many-body term is reasonably taken in the form of a function of the local coordination. In the glue model [12, 13], the Hamiltonian is written as:

$$H = K + V = K + \frac{1}{2} \sum_{i \neq j=1}^N \phi(r_{ij}) + \sum_{i=1}^N U(n_i) \quad (2.2)$$

where  $\phi$  is a two-body term,  $U$  is called “glue”-term and is a function which associates an energy to a value for the coordination,  $n_i$ , of the  $i$ -th atom. To have a zero potential energy for an isolated atom one sets  $U(0) = 0$ . The effective coordination  $n_i$  is calculated via:

$$n_i = \sum_{j=1(j \neq i)}^N \rho(r_{ij}) \quad (2.3)$$

i.e. as a superposition of contributions from neighboring atoms, where  $\rho$  is a short-ranged monotonically decreasing function of the distance and takes into account only few shells of neighbors. This makes the evaluation of  $n_i$  and then of  $V$  computationally very efficient. In particular, in spite of the intrinsic many-body character of the glue term, there are no explicit  $n$ -body terms, with  $n > 2$ , in the forces acting upon the atoms:

$$\mathbf{F}_i = - \sum_{j \neq i} \{ \phi'(r_{ij}) + [U'(n_i) + U'(n_j)] \rho'(r_{ij}) \} \frac{\mathbf{r}_{ij}}{r_{ij}}. \quad (2.4)$$

The short-range nature of the interaction allows to set up fairly easily simulation algorithms which scale with  $N$ .

The functions  $\phi$ ,  $\rho$  and  $U$  are entirely determined by fitting either experimental data or calculated ab-initio trajectories.

The data include thermal properties such as thermal expansion and other properties involving low coordination number, such as the surface energy. Use is made of the fact that any transformation of  $\phi$  and  $U$  in the form:

$$\begin{aligned} \widehat{\phi}(r) &= \phi(r) + 2\lambda\rho(r) \\ \widehat{U}(n) &= U(n) - \lambda n \end{aligned} \quad (2.5)$$

leaves all forces unaltered for any real number  $\lambda$ .

From the analytical point of view, the scheme is equivalent to several other formulations developed independently. The Finnes-Sinclair potential takes as a base empirically built  $\rho$  and  $\phi$  functions in the framework of second-moment approximation to tight-binding model [11]. The Embedded Atom Method (EAM) of Daw and Baskes was inspired on density functional theory, and interprets  $n$  as the electronic density [10]. The Effective Medium Theory (EMT), was given by Jacobsen *et al.* [20] and evaluates the embedding energy from the Density Functional Theory within the Local Density Approximation [21]. These schemes differ in practice a great deal in the approach to fitting, and give rise to very different potentials for a given material. The attention given to surfaces in the development of glue potential makes their choice the most suited for our purposes.

Most of our work will focus on the surfaces of Au (and marginally Pb), where accurate parameters have been optimized [12, 15].

## 2.2 Single-step PBC

In this section we will describe a particular set of Periodic Boundary Conditions which is suitable for the simulation of a flat surface with a single step on it.

Let us consider first the case of an ideal, unreconstructed, (100) surface. In usual MD, PBC enter both the evaluation of the interactions, and the particle motion. The real system is a periodically repeated box (in a slab case, a two-dimensional box in the  $x$  and  $y$  directions) and the so called ‘minimum image algorithm’ is used to calculate the distances between atoms. In standard PBC, given the distance vector (in scaled coordinates between -1 and 1) between atoms  $i$  and  $j$  (*i.e.*  $(s_1^{(i)} - s_1^{(j)}, s_2^{(i)} - s_2^{(j)}, s_3^{(i)} - s_3^{(j)})$ ), a test is made on every component along a periodic direction, which is adjusted in the following way:

$$\begin{aligned} (s_\alpha^{(i)} - s_\alpha^{(j)}) &\longrightarrow (s_\alpha^{(i)} - s_\alpha^{(j)}) + 1, \text{ if } (s_\alpha^{(i)} - s_\alpha^{(j)}) < -\frac{1}{2} \\ (s_\alpha^{(i)} - s_\alpha^{(j)}) &\longrightarrow (s_\alpha^{(i)} - s_\alpha^{(j)}) - 1, \text{ if } (s_\alpha^{(i)} - s_\alpha^{(j)}) > +\frac{1}{2}. \end{aligned}$$

A similar recipe is applied to the motion of a particle: if any scaled coordinate along a periodic direction exceeds the boundary value  $\pm 0.5$ ,  $\mp 1$  is added and the particle goes on on the other side of the slab.

When monoatomic steps are added on a flat surface, the allowed geometry is strongly dependent on surface orientation and on step orientation. In this work, we will focus on the fcc (100) surface, with a  $[110]$  step. In a (100), surface, with  $x$  and  $y$  axes oriented along  $[011]$  and  $[0\bar{1}1]$  (the close-packed chain orientation), the bulk layers parallel to the surface have a stacking ABABABAB... where the mismatch between layers A and B is  $(\frac{d}{2}, \frac{d}{2}, \frac{d}{\sqrt{2}})$ , if  $d = \frac{a}{\sqrt{2}}$  is the nearest neighbours distance.

Consider now an unreconstructed surface: if a single monoatomic step is added, the box can be suitably rotated in such a way that the first layer on the left connects with the second layer on the right. As discussed in §3.2.1, a single step setup cannot be achieved using ordinary PBC, due to the ABABAB... stacking which prevents matching. Denoting with  $(b, b, b_z)$  the mismatch (expressed in box-scaled coordinates) between layers A and B, matching along  $y$

can be achieved by adopting the boundary conditions

$$\left. \begin{aligned} \left( s_y^{(i)} - s_y^{(j)} \right) &= \left( s_y^{(i)} - s_y^{(j)} \right) - 1 + b \\ \left( s_x^{(i)} - s_x^{(j)} \right) &= \left( s_x^{(i)} - s_x^{(j)} \right) - b \\ \left( s_z^{(i)} - s_z^{(j)} \right) &= \left( s_z^{(i)} - s_z^{(j)} \right) + b_z \end{aligned} \right\} \text{if } \left( s_y^{(i)} - s_y^{(j)} \right) > \frac{1}{2}$$

$$\left. \begin{aligned} \left( s_y^{(i)} - s_y^{(j)} \right) &= \left( s_y^{(i)} - s_y^{(j)} \right) + 1 - b \\ \left( s_x^{(i)} - s_x^{(j)} \right) &= \left( s_x^{(i)} - s_x^{(j)} \right) + b \\ \left( s_z^{(i)} - s_z^{(j)} \right) &= \left( s_z^{(i)} - s_z^{(j)} \right) - b_z \end{aligned} \right\} \text{if } \left( s_y^{(i)} - s_y^{(j)} \right) < -\frac{1}{2},$$

while usual PBC are applied along  $x$ . Moreover, when a particle crosses the box boundary along  $y$  and is folded on the opposite side, it must undergo an additional translation by a vector  $(b, -b, b_z)$ . The box boundary along  $y$  is set at  $\pm\frac{1}{2}(1-b)$ , instead of  $\pm\frac{1}{2}$  as in ordinary PBC. The ‘‘empty space’’ left is illusory, as it is ‘‘filled’’ by the additional translation. In this way, a symmetric box along  $y$  is obtained and overlapping of atoms is avoided. This is only one of the possible realizations of this kind of PBC, but it was found to be the simplest to implement within our MD programs.

### 2.3 Algorithm for extracting step profiles

We have developed an algorithm for extracting the step profile from a set of trajectories produced by a simulation run. This simple ‘step detection’ is efficient if the step profile is a univocal function of  $x$ ,  $x$  being the  $T = 0$  step direction. As usual, we sketch the main stages of the algorithm:

- the surface atoms are extracted using Carnevali algorithm, described in the following section.
- the surface is divided into slices parallel to the  $y$  axis;
- for every slice, the point of maximum height variation is found;
- an interpolation with adjacent slices is performed.

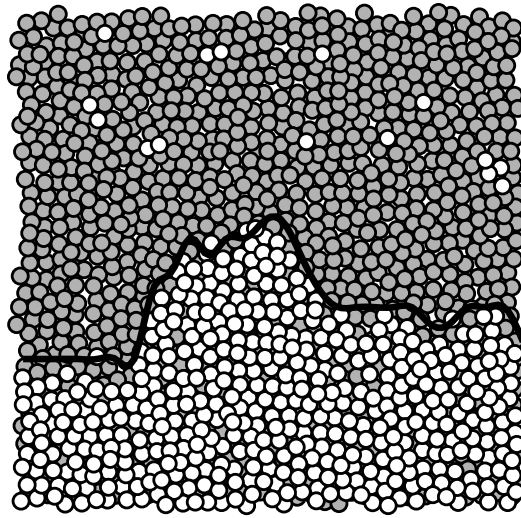


Figure 2.1: An example of step detection. Brighter atoms are higher. The color is obtained through a threshold on the height, the solid line is obtained using the algorithm described in the text.

An example of step detection is shown in Figure 2.1. This simple algorithm has been used to process several trajectory files automatically, in order to obtain significant statistical averages on step position and deviation.

## 2.4 An algorithm for detecting and classifying holes and islands

In this section we will describe an efficient algorithm which is able to describe a surface covered with holes or islands. For each hole (island) a size and a ‘center of mass’ are identified. The input file is, as usual, a trajectory file containing snapshots of the atomic positions at different times. First of all, the atoms of the surface are identified by using an algorithm that we will call ‘Carnevali algorithm’ [22]; this algorithm defines as *surface atom* a particle such as all the other particles lying in its *action cylinder* have a lower  $z$ . The *action cylinder* is a vertical cylinder of radius  $R_C$ , the choice of which will be discussed just below. After building the action cylinder for each atom (*i.e.*, a suitable bidimensional neighbour list), a loop is done on all the atoms and surface atoms are extracted.

Of course, the correct value of  $R_C$  is not universal. It depends not only on the lattice spacing, but also on the particular structure of the surface. A guess for a

correct value of  $R_C$  can be done by repeating the algorithm for different values of  $R_C$ . The surface atoms number versus  $R_C$  is a monotonically decreasing function, and the inflection point of the curve can be considered as the correct value for  $R_C$ .

Once surface atoms are extracted, different operations on the atoms can be performed: bidimensional orientational orders, structure factor, diffusion calculations and so forth. The argument of this section is the extraction of islands and holes. First, a height threshold is established above (under) which a surface atom is considered part of an island (hole); for example, the slab can be divided into small intervals along  $z$  and the threshold  $z_T$  for islands (holes) is defined just above (below) the position of the lateral density maximum.

From now on, we will treat the island case. Lists of neighbours are built for surface atoms lying above  $z_T$ . Every atom has an index  $NLIVE$  which indicates which island it belongs to; initially,  $NLIVE() \equiv 0$ . Every island has an index  $ISHAB$  counting its inhabitants. The algorithm proceeds in the following way:

1.  $NISL = 0, I = 1$ .
2. Consider atom  $I$ . If  $NLIVE(I) \neq 0$ , the atom belongs already to an island.  
 $I = I + 1$ . If  $I \leq NATOMS$  GOTO 2, ELSE STOP.
3. If  $NLIVE(I) = 0$ ,  $I$  is declared the first inhabitant of a new island:
4.  $NISL = NISL + 1$ .  
 $NLIVE(I) = NISL$ .  
 $ISHAB(NISL) = ISHAB(NISL) + 1$ .
5. Begin the loop on the neighbours of  $I$ : CALL NEIGHLOOP ( $I$ ).
6.  $I = I + 1$ . If  $I \leq NATOMS$  GOTO 2, ELSE STOP.

[NEIGHLOOP] ( $J$ ) Recursive loop on the neighbours:

- $K = \text{neighbour}(J)$
- If  $NLIVE(K) = 0$  :  
 $NLIVE(K) = NISL$   
 $ISHAB(NISL) = ISHAB(NISL) + 1$

- CALL NEIGHLOOP ( $K$ )
- Repeat on all  $K$ 's.
- RETURN.

At this point, the  $i$ -th island has a size  $ISHAB(i)$  and the atoms belonging to the island have  $NLIVE = i$ . On the surface there are  $NISL$  islands, and statistics can be made using trajectory files. Moreover, a particular island can be monitored in its time evolution.



## Chapter 3

# **The hexagonal reconstructed noble metal (100) surface: reconstruction, deconstruction, vicinals, faceting and its precursors**

### **3.1 The Au(100) surface**

The flat (100) surface of gold constitutes, along with those of platinum and iridium, a classic example of hexagonal surface reconstruction of a square surface of a noble metal.

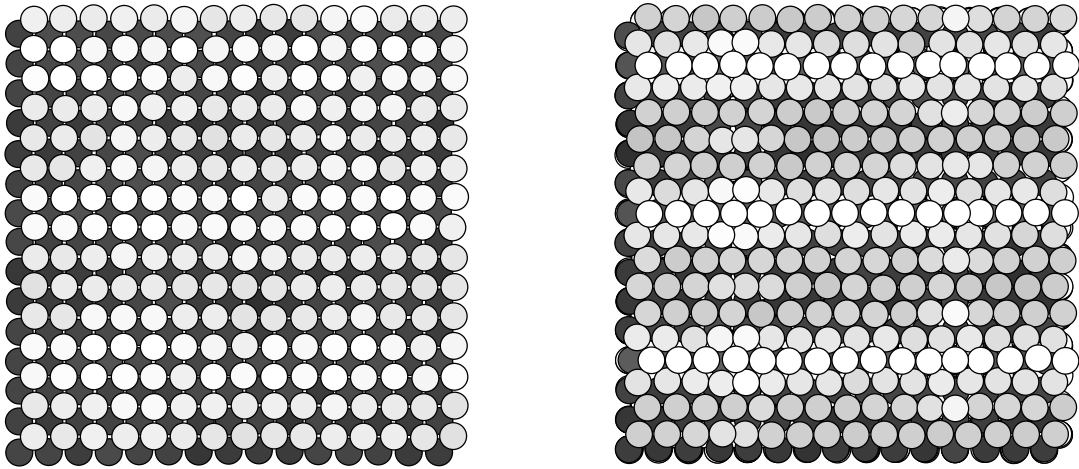


Figure 3.1: The unreconstructed (100) surface at  $T = 0$  and the reconstructed phase. Corrugation is due to the approximate  $(1 \times 5)$  superstructure. Brighter atoms are higher.

Since the early electron diffraction studies [23], the surface layer structure of Au (100) is known to be denser than a regular (100) plane, and nearly-triangular (see Figure 3.1). Incommensurate epitaxy of this dense top layer onto the underlying (100) crystal planes produces misfit dislocation crystal planes produces misfit dislocations (“solitons”) and a large unit cell, more recently estimated to be close to  $(28 \times 5)$  [24, 25, 26, 27, 28]. The fivefold periodicity is due to the stacking of six [011] rows on top of five rows in the second layer. The large periodicity in the orthogonal direction is the consequence of a small contraction along the [011] rows. The density increase with respect to a regular (100) crystal plane is about 24 percent. Theoretical investigations of this surface [12] indicated that this reconstruction is driven by the tendency of surface atoms to increase packing, which in turn may be explained in terms of the surface electronic structure [29].

X-ray reflectivity measurements as a function of temperature [27, 28] show that the hexagonal diffraction spots disappear abruptly around  $T_D \simeq 1170$  K (i.e.,  $\sim 0.875 T_m$  where  $T_m = 1336$  K is the melting point). The deconstruction transition has been characterized as a triangular-to-disordered, first-order phase transition [27, 28]. The precise nature of the disordered phase is presently not known.

We have simulated the behavior of this surface, using the glue potential and

molecular dynamics. Our system was a 16-(100) layer slab comprising altogether about 14000 particles, with the first layer initially arranged in a nearly optimal triangular structure of density 1.24 with respect to the lateral density of a bulk (100) plane. Temperature was gradually and carefully raised from zero up to 1300 K, just below bulk melting, where this model surface, like the real one, is incompletely melted [30]. From here the system was slowly cooled in small steps of 10 K, with a very long annealing time of about 0.5 ns at each temperature.

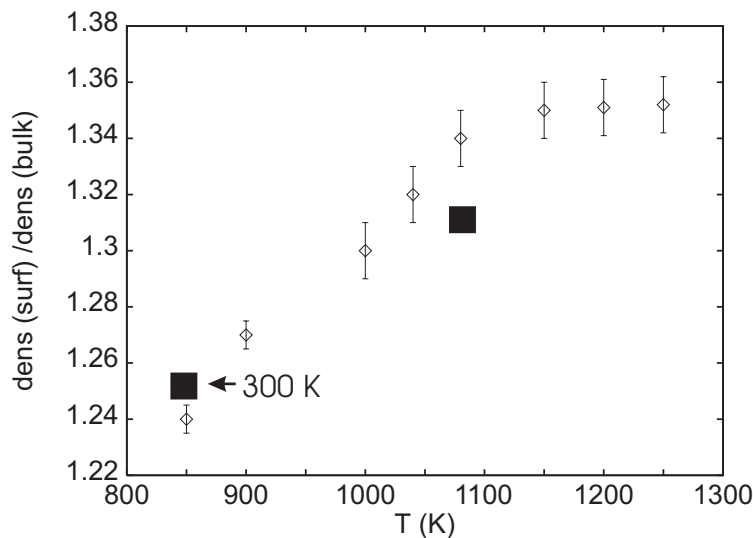


Figure 3.2: Lateral surface density of Au(100) from MD simulations as a function of temperature. Note the steady increase, and a leveling off around the glue model deconstruction temperature  $T_D = 1050$  K (experimental  $T_D = 1170$  K). Filled squares correspond to experimental points taken from [31].

Upon heating, the lateral density of the surface shows a tendency to increase with increasing temperature, as shown in Figure 3.2. At each temperature the system was annealed through a constant-temperature run (more than 2 nanoseconds). Using the Carnevali algorithm described in Chapter 2, we have extracted the average density for each temperature. The lateral density can also be independently extracted in the framework of the single step boundary conditions, by monitoring the step position. The results obtained with the two methods were found to coincide.

This unusual behaviour (the lateral density increase) is confirmed experimentally for both Au and Pt [28]. Two experimental points from [28] are drawn

on the Figure. Since our simulations are particle-conserving (canonical), this density increase leads to formation of a crater in the top layer, whose size increases with temperature. This was also found by Bilalbegović and Tosatti [30]. The temperature-driven density increase appears to be connected with the very same packing tendency which causes the reconstruction at  $T = 0$ . When the surface layer contracts laterally going from square to triangular, it does so with an additional oscillatory vertical *outward* relaxation over the second layer. The vertical expansion is easy to understand, since in fcc the interplanar spacing is 15% larger for (111) planes than for (100) planes, and the present situation [a (111) plane over a (100) plane] is intermediate. The relaxation is larger at the soliton, whence the oscillatory behavior. As temperature rises, the outward relaxation undergoes a further, anomalously large anharmonic increase. This increase is connected primarily with meandering of solitons. The anomalous expansion magnitude is in fairly good agreement with X-ray data [31, 27, 28] up to the deconstruction temperature. Above  $T_D$  our results are in contradiction with interpretation of the same experimental data: X-Rays suggest a sudden drop in surface density to the bulk value of 1, whereas no density drop is seen in our simulations.

In correspondence with the vertical expansion, the first, triangular layer becomes less coupled to the second, and the interplanar contribution to surface coordination decreases very strongly. The additional in-plane contraction therefore takes place to compensate for this excessive decrease with a corresponding in-plane increase, which is necessary to keep energy from growing excessively.

Besides the density change, temperature causes an evolution of other order parameters of the hexagonal layer, notably the orientational order. To measure the degree of orientational order, we calculate the sixfold orientational order parameter [32] at each atomic site  $i$  in the first layer:

$$O_{6i} = \frac{1}{N_i} \sum_j e^{6i\theta_{ij}} \quad (3.1)$$

where the sum is limited to the  $N_i$  in-plane first neighbours of  $i$ , and  $\theta_{ij}$  is the angle formed by the  $ij$  bond, projected on the  $xy$  plane, with the  $x$  axis.  $|O_{6i}|$  measures the degree of local triangular order at the surface, while the phase measures the local lattice orientation. We then construct a long-range orientational order parameter average  $|\langle O_6 \rangle| = |\langle \frac{1}{N} \sum_i O_{6i} \rangle|$ , where the sum

on  $i$  is extended to all the  $N$  atoms at the surface and  $\langle \dots \rangle$  indicates averaging over many configurations; and its short-range counterpart, the average modulus  $\langle |O_6| \rangle = \langle \frac{1}{N} \sum_i |O_{6i}| \rangle$ . In order to select the surface atoms we used the same algorithm invented by Carnevali and described in Chapter 2 [22].

Results for the profiles of order parameters parallel to the surface at  $T = 1040$  K are shown in Figure 3.3(b). Well inside a terrace, and away from the crater, we find a value for  $|\langle O_6 \rangle|$  of about 0.5, characterizing the finite amount of long-range order at this temperature. While  $|\langle O_6 \rangle|$  is depressed in the crater region,  $\langle |O_6| \rangle$  is not, indicating that the crater bottom is again reconstructed (as seen also by the lateral density).

The depression of  $|\langle O_6 \rangle|$  indicates incoherence of the two reconstruction motifs, that in the crater bottom, and that above the rim. The situation changes abruptly above  $T_D \sim 1050$  K.

Figure 3.4 shows, for example, a picture of the surface at 1100 K. The stripes have now lost their long-range connectivity, and the surface is orientationally disordered. This is confirmed by a drop of  $|\langle O_6 \rangle|$  to about 0.15, well below its value below  $T_D$ , and in fact compatible with zero for infinite size. It is important to note that only the long-range order parameter,  $|\langle O_6 \rangle|$ , has fallen, whereas hexagonal short-range order, as measured by  $\langle |O_6| \rangle$ , unaffected by phase disorder, remains high, as does the lateral density. Hence we can conclude, as is also clearly suggested by Figure 3.4, that a possible mechanism of deconstruction is tied to the loss of coherence of locally triangularly ordered domains, with collapse of the one-dimensional solitons and stripes which divide them.

While this picture is rather appealing, there is a disturbing point. Ignoring the crater regions, we find that the lateral surface density levels off with temperature, but does not decrease or drop across and above  $T_D = 1050$  K (Figure 3.17). This is in apparent contrast with existing fits of the specular X-ray intensity, indicating a drop of lateral density, from 1.33 below  $T_D$  to 0.98 above  $T_D$  [31]. The reason for this disagreement is presently unclear. One possibility is that in true grand canonical equilibrium, the surface structure and density might behave differently from our simulated, strictly canonical system. In particular, large craters might be a true equilibrium feature above  $T_D$ . We shall return on this point later on.

Next, we shall consider the role of steps on this hex-reconstructed surface.

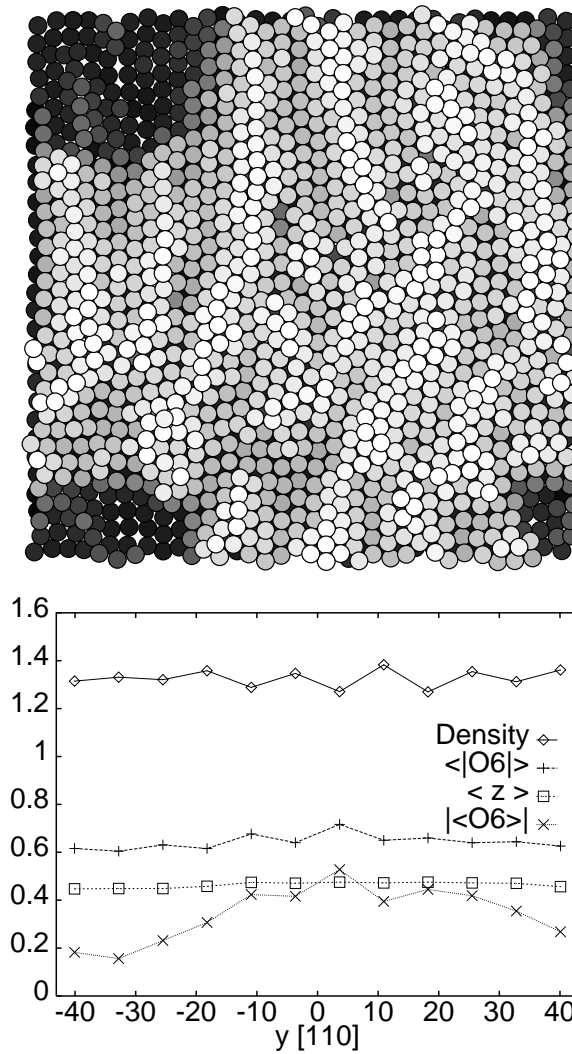


Figure 3.3: Simulation results for Au(100) at 1040 K (just below  $T_D$ ) with a top layer mean lateral density of 1.32. (a) Top view of a configuration. The grey scale represents the  $z$  coordinate of atoms; lighter zones are higher. The reconstruction is visible mainly through the striped domain-walls. The “crater” discussed in the text is visible at the four corners (a single crater, seen with periodic boundary conditions). (b) Surface density (relative to that of a bulk (100) plane), long-range and short-range order parameters, and height profile. Quantities shown as a function of the  $y$  coordinate in the surface plane, after averaging along on the  $x$  coordinate. Note the depression of long-range order and of height, but not of short-range order and of density, caused by the crater.

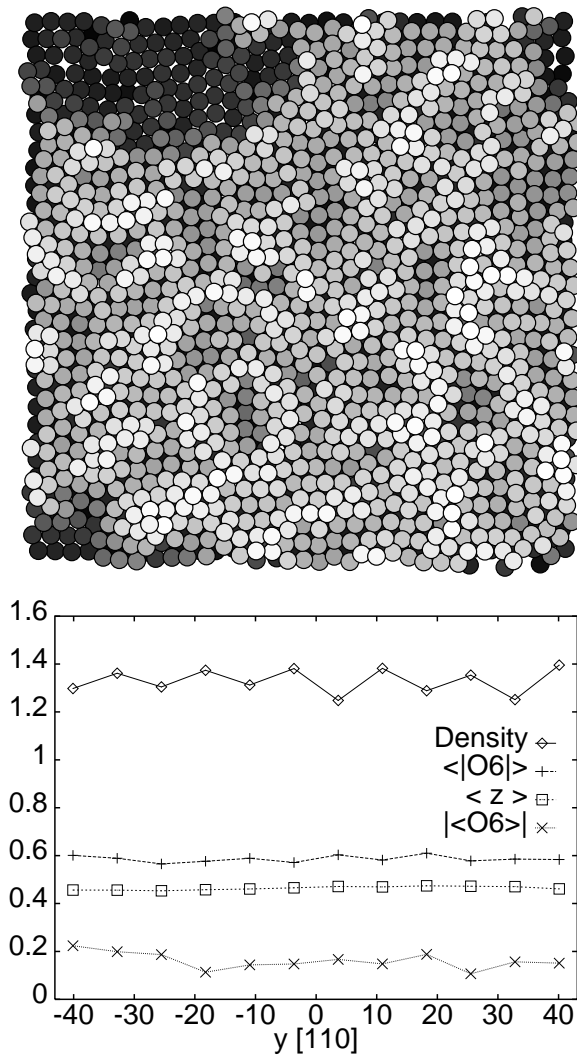


Figure 3.4: Simulation results for Au(100) at 1100 K (just above  $T_D$ ). Same atoms number, notations and conventions as in Figure 3.3. The domain wall stripe order is now spoiled. The long-range order parameter has dropped, indicating deconstruction. Short-range order and high density remain, suggesting that deconstruction is due to loss of long-range phase coherence of the triangular overlayer.

## 3.2 The single step on a Au(100) surface: non-standard PBC

It is of obvious interest to study the behaviour of an isolated step on a flat surface, and its interplay both with the reconstruction-deconstruction mechanism and with temperature-induced density changes. The simulation of an odd number of steps per cell, in particular of a single step on a (100) flat surface is impossible with the usual periodic boundary conditions (PBC), due to the ABABAB... stacking structure of a slab with the surface oriented in this way. In this section, we will adopt an alternative set of PBC (described in §2.2) which guarantee the correct matching at the boundaries; we used this method to study the temperature evolution of a  $(01\bar{1})$  step on differently sized (100) surfaces. To this end, we developed a simple algorithm (described in §2.3) to monitor the step position and its fluctuations; a microscopic insight on the interplay between step and reconstruction is eventually obtained.

### 3.2.1 Simulation of $(K11)$ vicinals of (100)

Addition of one or more steps to a slab with PBC gives rise to a vicinal surface. The vicinals of (100) we have considered are obtained by tilting around the  $[01\bar{1}]$  axis, giving rise to faces with Miller indices  $(K, 1, 1)$ , with  $K$  odd. The steps run along the  $[01\bar{1}]$  ( $x$ ) direction, and are separated by (100) terraces which are  $M = \frac{(K+1)}{2}$  atoms wide in the  $[011]$  ( $y$ ) direction. The angle of inclination of the vicinal is determined by the length of the terrace along  $y$ :  $\theta = \arctan\left(\frac{\sqrt{2}}{K}\right)$ . If we call  $z$  the coordinate along  $[100]$ ,  $y'$  that along  $[\bar{2}K K]$  and  $z'$  that along  $[K 11]$ , we observe that  $xy'z'$  form an orthogonal system, obtained by rotating the  $xyz$  system by an angle  $\theta$  along the  $x$  axis. The standard way [33] of simulating such a vicinal surface is to set up a MD box with the edges oriented along  $xy'z'$ . The length of the box along  $y'$ ,  $L'_y$ , is such as to accommodate an even number  $2N_{DT}$  of terraces, with  $L'_y = N_{DT}K d / \cos\theta$  for a  $(K, 1, 1)$ . Since triangularity has to be preserved along the steps and the bulk layers have the already described ABABAB... stacking, two steps and two terraces correspond to the minimum periodicity length in the  $y$  direction. This allows only the simulation of  $(K 1 1)$  vicinals with  $K$  odd.

This kind of MD box is constructed by starting from a (100) slab with  $2N_{DT}$

steps in a  $xyz$  oriented box, and applying a rotation operator on the particle coordinates to transform it into a  $xy'z'$ -oriented box. As a result, the area of the slab increases of a factor  $1/\cos\theta$ . The rotation creates a perfect match between the box and its image at the box boundary. For example, for a slab with 2 steps, the first layer of one box connects smoothly with the third layer of the adjacent box. To allow the simulation of a single terrace with a single step, we have modified the PBC according to the scheme described in §3.2.

### 3.3 Vicinals of Au(100) simulated with a single step

We have simulated low angle  $(K\ 1\ 1)$  vicinals of the (100) surface of gold, quasi-hexagonally reconstructed, plus a single step in the simulation cell, with the PBC described in §2.2. The largest terrace we have simulated corresponds approximately to a  $(100\ 1\ 1)$  vicinal surface. In this system, the step interacts only with its own image and the length of the terrace is fixed by construction to be  $L_y$ , the lateral dimension of the box along  $y$ . A smaller slab is shown in Figure 3.5. The corrugation arising from the hexagonal reconstruction solitons is clearly seen.

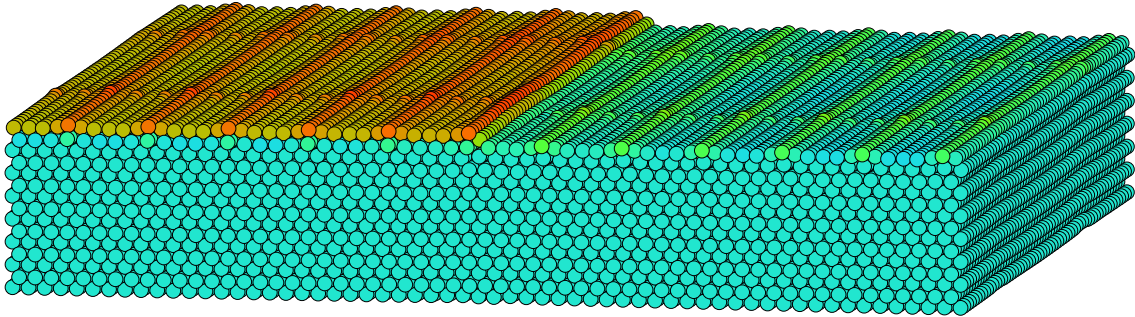


Figure 3.5: Lateral view of a slab with a single step. Top surface is reconstructed.

With this simulations, we wanted to address the following points:

- what is the optimal phase and amplitude relationship of the hexagonal reconstruction relative to the step position?
- what is the predicted detailed morphology?
- the step can act as a reservoir of atoms, if there are lateral density changes of the surface which want to take place. The drift of the average  $y$ -position

of the step will signal these density changes, and allow extraction of the exact value of the lateral density at any given temperature.

- Temperature changes induce density changes, but too sudden changes at low temperature cannot be followed by a suitable step drift; the surface is then forced to form craters in order to increase the lateral density. We can study the interplay between the step and the craters.
- When the step moves, (*i.e.*, it advances, or retracts, or meanders), regions of the second layer can become uncovered, inducing occurrence of local reconstruction/deconstruction. What is the role of the step in this mechanism?
- The mean square displacement of the step (finite because of finite size) obviously increases with temperature. That increase is connected with the entropy associated with the step. Is it possible to extract quantitative information about this entropy? Can we extract the effective step tension?
- Is the high temperature state of this surface a compact (flat) one or a non compact (disordered flat) one?

We have tried to answer some of these questions, leaving the other for future research. We simulated two different boxes, with two terrace areas: the first was composed by 625 atoms per bulk layer, the second by 2500 atoms per bulk layer. The corresponding terrace sizes were  $(72\text{\AA} \times 72\text{\AA})$  and  $(144\text{\AA} \times 144\text{\AA})$ , respectively. Both slabs were carefully heated up to the melting point and subsequently cooled in order to extract physical quantities at different temperatures.

The slab is prepared with a lateral density of 1.24 with respect to the bulk square  $(1 \times 1)$  layer. This value corresponds to the energy optimum required by the glue potential at  $T = 0$  [12]

### 3.3.1 Surface density

The slab at low temperature ( $T < 900K$ ) (a picture is shown in Figure 3.6) shows no appreciable step motion.

This is apparently due to the low mobility of the atoms in this range of temperature and perhaps also the moderate excess density required in this range of temperatures.

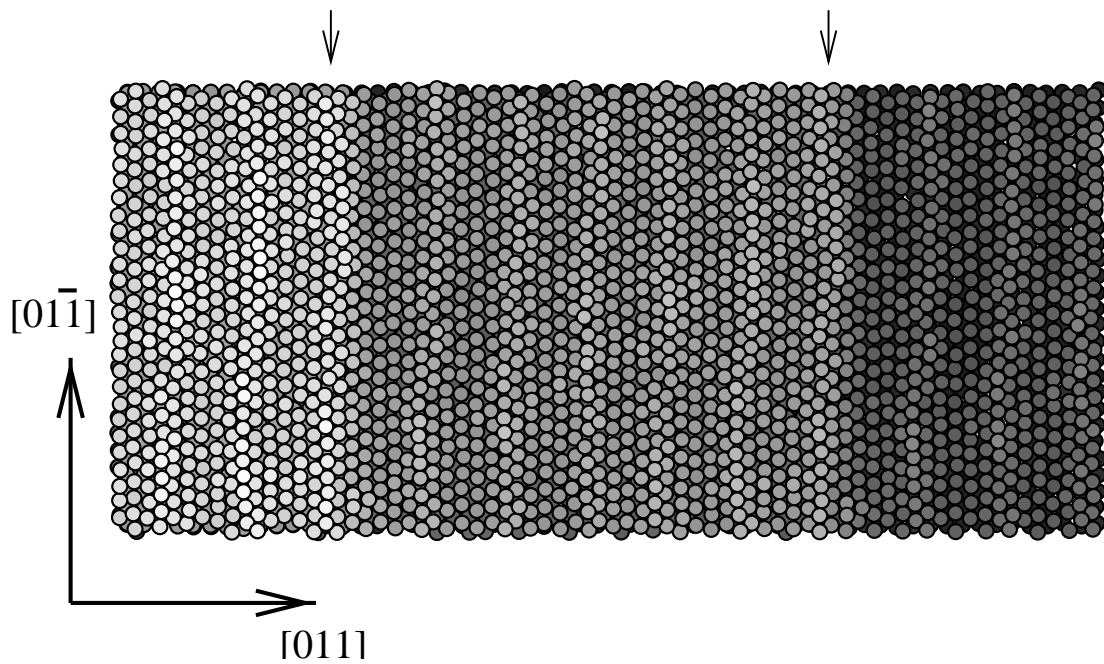


Figure 3.6: The slab with monostep periodic boundary conditions (top view); two MD boxes are shown along the staircase direction  $[011]$ . Color coding related to height: brighter is higher. No step shrinking is observed at this temperature of 600 K. The arrows indicate the step position (mid-point in lateral density of the 'second' layer). Note that solitons (lighter) are attracted to the step rim, but repelled from the lower step tread.

For  $T > 900K$ , when mobility sets in, the step shrinks, signaling an increasing of the lateral density. The mean position  $\langle y_{step} \rangle$  of the step versus temperature is plotted in Figure 3.7. The conservation of the number of particles can be used to extract the increase in lateral density, setting  $y_{step} = L_y$  at  $T = 0$ :

$$\begin{aligned} N_s^{(1)} + N_b &= \left( N_s^{(2)} + N_b \right) \frac{L_y - y_{step}}{L_y} + N_s^{(2)} \frac{y_{step}}{L_y} \\ N_s^{(2)} - N_s^{(1)} &= N_b \left( 1 - \frac{y_{step}}{L_y} \right) \\ \frac{\Delta \rho_s}{\rho_b} &= \left( 1 - \frac{\langle y_{step} \rangle}{L_y} \right). \end{aligned} \quad (3.2)$$

where  $L_y$  is the slab length orthogonal to the step,  $N_s^{(i)}$  is the number of atoms in the  $i$ -th layer,  $N_b$  is the number of atoms in a bulk layer,  $\rho_b$  is the bulk (100) lateral density, and  $\Delta \rho_s$  is the increase in lateral density at the surface.

Eq. 3.2 is applied to the data sketched in Figure 3.7 and the same results plotted in Figure 3.2 are obtained. The step position at  $T = 1300 K$  has an excess retraction due to the partial melting of the second layer.

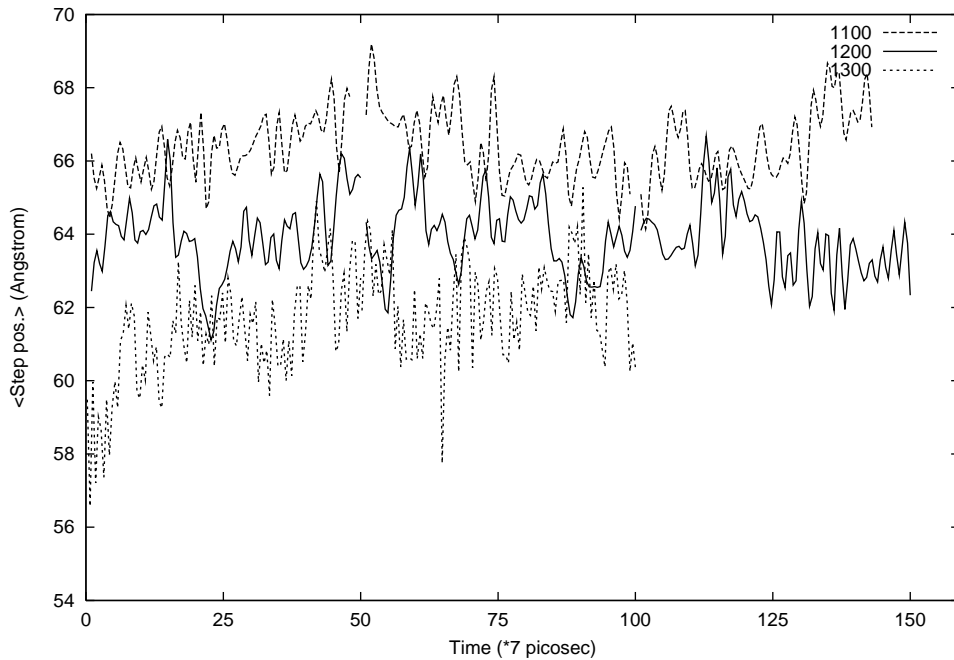


Figure 3.7: The step position as extracted by the algorithm of step detection for different temperatures. The  $T = 0 K$  step position is located at  $L_y = 72 \text{ \AA}$ .

Data collected in this way can be used to confirm data shown in Figure 3.2.

The lateral density is seen to increase monotonically with temperature. This result agrees with that obtained through different simulations in §3.1. Again we stress that experimentally X-ray specular intensity fits suggest  $\rho_s = 1.25$  at  $T = 500K$ ,  $\rho_s = 1.33$  at  $T = 1100K$  but  $\rho_s = 0.98$  (sic!) at  $T = 1250K$ . The lateral density increase is very close to the one we found. However, we cannot explain the drop at the highest temperature.

### 3.4 Interplay between reconstruction and step

In this section we investigate the relationship between the in-plane density within a layer -which strongly changes upon reconstruction- and the position of a step, which divides a layer in two regions with different atomic structure.

Let us orient a reference system so that  $z$  axis points in the  $[001]$  direction, and  $y$  axis is orthogonal to the step profile. We will call ‘first layer’, the portion of the slab lying above a certain threshold  $z_1$  (see Figure 3.8). As it is evident from the figure, the second layer is partially covered by a terrace (zone A); this part of the second layer is of course deconstructed. Conversely, the remainder of the second layer is itself a terrace and is reconstructed (zone B). The interface between zone A and zone B is marked by the step. The lateral density of the unreconstructed zone ( $0.1207\text{\AA}^{-2}$  at  $T = 0K$ ), henceforth  $\rho_A$ , and of the reconstructed zone ( $\rho_B = 1.24\rho_A$  at  $T = 0K$ ) are connected by a density profile whose structure we can obtain.

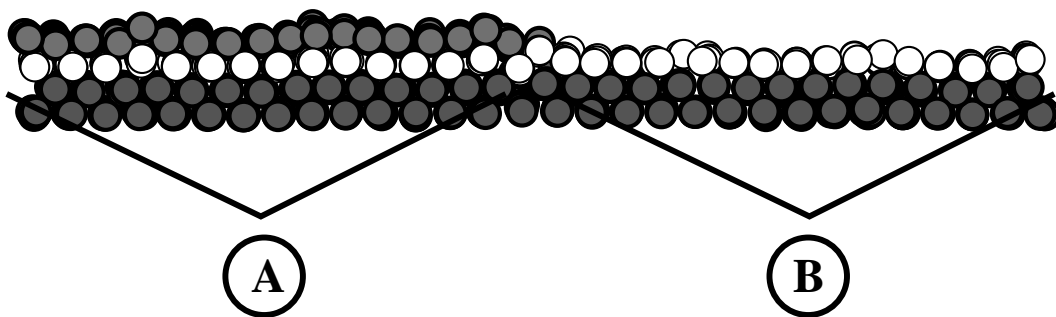


Figure 3.8: Side view of the surface with the single step. The second layer atoms are drawn in white. (A) denotes the part of the second layer which lies under the terrace and is unreconstructed, (B) denotes the uncovered reconstructed terrace.

The interface between two phases, for example solid and liquid, and its width

or temperature dependence, has been widely studied [34, 35, 36], by various methods, including density functional, and also phenomenological Ginzburg-Landau (G-L) approaches. In this framework the free energy of a system is written as a functional of the order parameter(s) involved in the phenomena under study. In our case, for example, the simplest order parameter could be the lateral density.

Calling  $n_0(y)$  and  $n_1(y)$  the lateral density of the zeroth (outermost) and first layer across the step direction, a G-L free energy functional could be considered, *e.g.*, of the form:

$$F [n_0, n_1] = \int_{-\frac{L}{2}}^{\frac{L}{2}} dy \left\{ f [n_0 (y), n_1 (y)] + J_0 \left( \frac{d n_0}{d y} \right)^2 + J_1 \left( \frac{d n_1}{d y} \right)^2 - \mu [n_0 (y) + n_1 (y)] \right\} \quad (3.3)$$

where  $f(n_0, n_1)$  is a surface free energy density possessing two separate and equivalent minima, namely  $(0, \rho_B)$  and  $(\rho_B, \rho_A)$ ,  $\mu$  is a chemical potential allowing the control of total particle number, and the gradient terms express the cost associated with the step, where  $n_0$  switches from  $\rho_B$  to zero, while  $n_1$  switches from  $\rho_A$  to  $\rho_B$ . Here  $\rho_A = 1$  is the lateral density of a bulk (100) layer and  $\rho_B \sim 1.24$  is that of the hexagonal layer.

In a theory of this kind, densities would vary roughly as hyperbolic tangents at the step, and the step width  $2\xi$  would be related to the stiffnesses  $J_0, J_1$ , as well as to the shape of  $f(n_0, n_1)$  at and between the two minima. If  $f(n_0, n_1)$  is assumed of the form  $f(n_0, n_1) \sim f(n_0 + n_1) = K \sin \left[ 2\pi \left( \frac{n_0 + n_1}{\rho_A} \right) + \phi \right]$  ( $\phi$  is a phase factor chosen in order to have two minima in  $\rho_B$  and  $\rho_B + \rho_A$ ) and  $J_0 = J_1 = J$  then  $\xi \sim \left( \frac{K}{J} \right)^{1/2}$ . We will not try to develop here the detailed form for this G-L functional. The main quantitative result we would like to extract from the simulations is the width  $\xi$  of the interface.

In order to obtain a correct estimate of the density profile, we must extend the algorithm of edge detection described in Chapter 2 to a thermally disordered situation, since the step meanders considerably, giving rise to a large  $x$ -dependence of his actual position. We divide the slab in  $x$ -slices. For each time step, the density profile was obtained as an average on the local profiles for each

$x$ -slice. If  $y_i$  is the coordinate along the  $i$ -th slice and  $y_i^{(s)}$  the position of the step, the average local density profile can be defined as:

$$\rho(y) = \frac{1}{N_{\text{slices}}} \sum_i \rho(y + y_i^{(s)}) \quad (3.4)$$

The profile was calculated both at  $T = 900K$  and at  $T = 1200K$ . The results are shown in Figure 3.9 and 3.10.

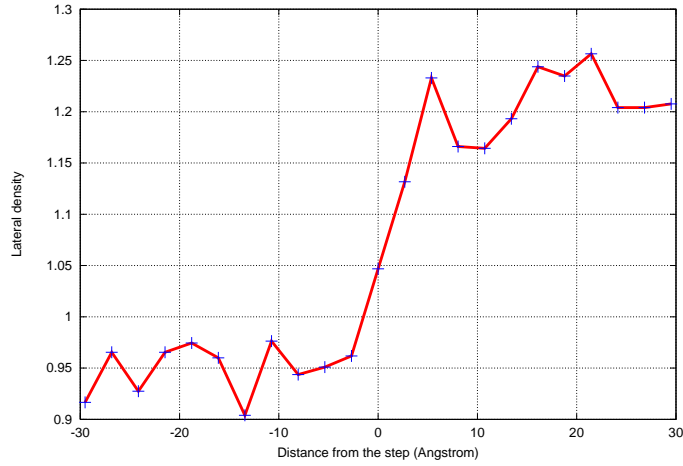


Figure 3.9: Profile of the lateral density in the “second layer”  $\langle n_1(y) \rangle$  for  $T = 900 K$ . The layer has a square structure to the left, where it is covered by a terrace, and a dense hexagonal structure to the right. The interface between the two zones is smoothed by the presence of a finite correlation length  $\xi$  of the step.

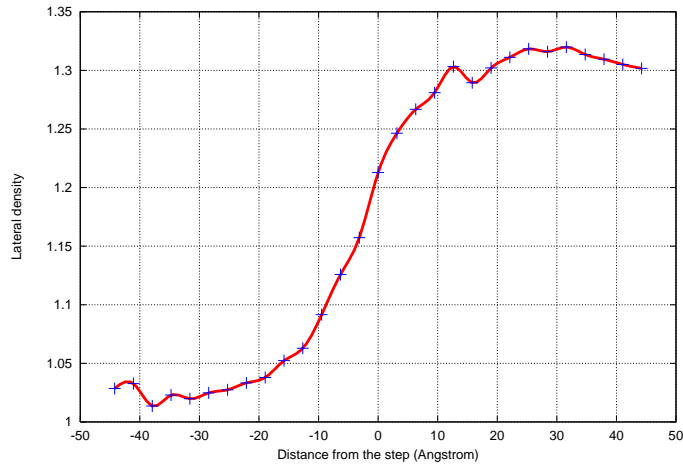


Figure 3.10: Profile of the lateral density  $\langle n_1(y) \rangle$  in the second layer (same as Figure 3.9) but for  $T = 1200 K$ . Note the smoother profile, and a larger correlation length  $\xi$ .

The resulting curve can be fitted with a hyperbolic tangent, and the correlation length around the step turns out to be of about  $5\text{\AA}$  at  $900K$ , rising to about  $10\text{\AA}$  at  $1200K$ . The reason for this increase is most likely the increasing of step meandering.

This result is important, since gives a measure of the influence of the step on the lateral coordination in its neighbourhood; this fact will be used in Chapter 6 in order to explain a critical size for reconstruction of craters or for the deconstruction of the layer under a small island adsorbed on the surface.

### 3.5 The shrinking of a terrace with retraction of a step

As we have just seen, when steps are present on the hex-reconstructed (100) surface, all exposed terraces are reconstructed, and thus laterally denser, but their continuing lattice plane which lies below the next higher terrace is unreconstructed, and has a density very close to the bulk value (see Figure 3.9). An interesting question arises when the step locally moves. Local step motion can arise either due to addition/removal of atoms (advance/retraction), or to thermal meandering, or else due to sudden heating/cooling, owing to the direct connection between temperature and lateral density.

When a step retracts, it uncovers by doing so a portion of terrace which must also become reconstructed. This must occur by incorporation into the lower terrace of atoms formerly belonging to the upper retracting terrace, whose retraction must in turn be accelerated by this loss. Conversely, when a step advances, it covers a portion of terrace which must at the same time deconstruct. This must liberate unwanted atoms, which must therefore be incorporated in the advancing upper terrace, causing it to advance even more. While this mechanism is logically obvious, its actual occurrence and its consequences seem worth studying in some detail.

In this section we present a detailed example of step retraction, to show the microscopic mechanism leading to the reconstruction of the second layer regions which remain uncovered.

To this end, we present a set of single-step simulation frames (3.11) in which atoms of the first layer involved in the process are marked with a number and atoms of the second layer are marked with letters. The starting point is an

equilibrated step at  $800K$ , suddenly brought to a higher temperature of  $950K$ .

As can be seen in Figure 3.2, the equilibrium lateral density of the upper terrace suddenly jumps upwards by  $\sim 5\%$ , whence the step begins to retract. In successive frames, spaced by  $1.4ps$  between one another, we see that first step edge atoms such as 1, 2, 3, 4, 5, 6, 7 and then progressively second-line atoms such as 11, 12, 13, 14 and 15 are abandoned by the retracting step, and get incorporated into the lower terrace. The positive feedback which we had anticipated does exist, and appears also to play a dynamical role in rendering the retracting step particularly wiggly.

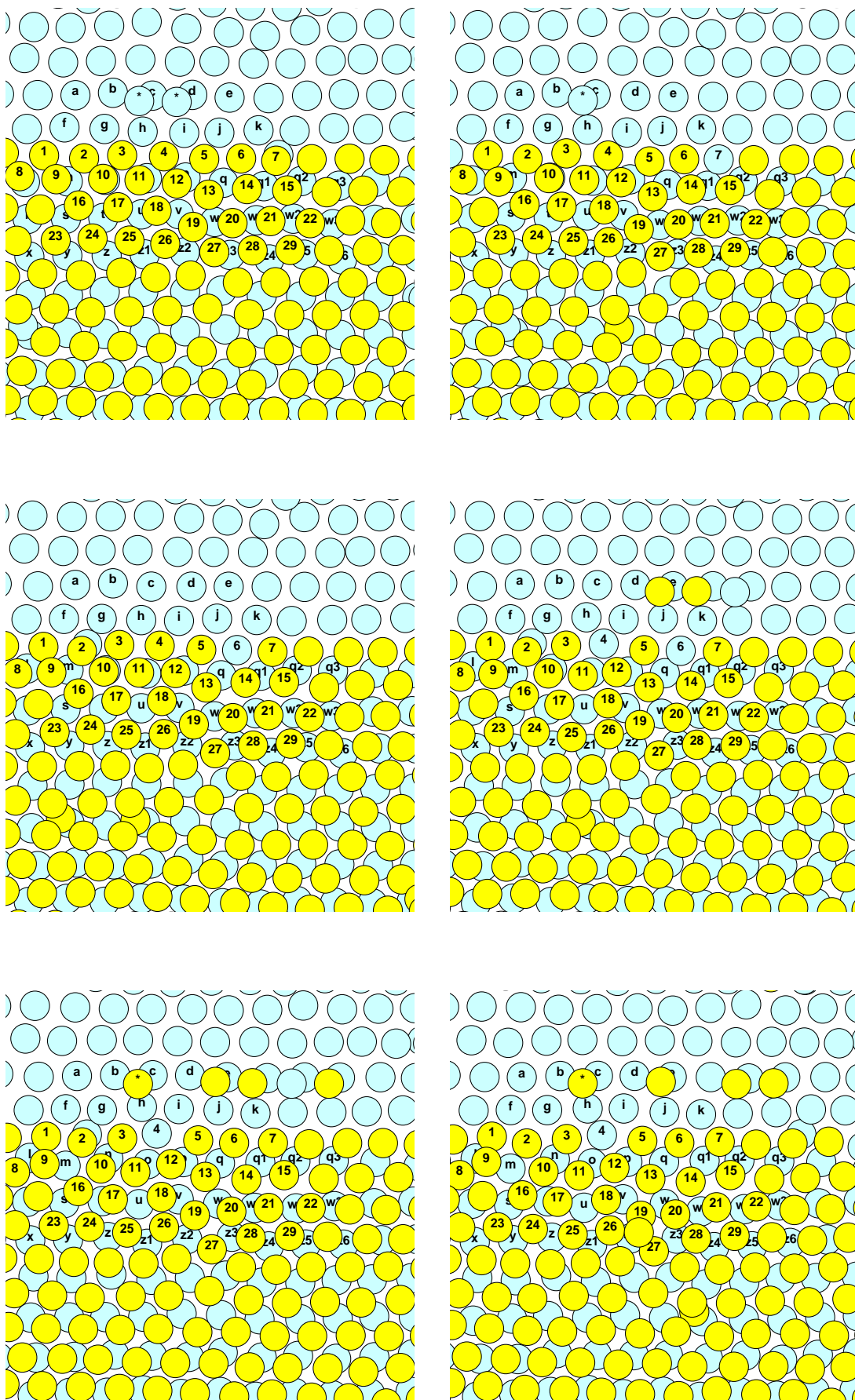


Figure 3.11: (color) Equilibrated step at 800K, suddenly brought to a higher temperature of 950K. Each frame corresponds to 1.4ps.

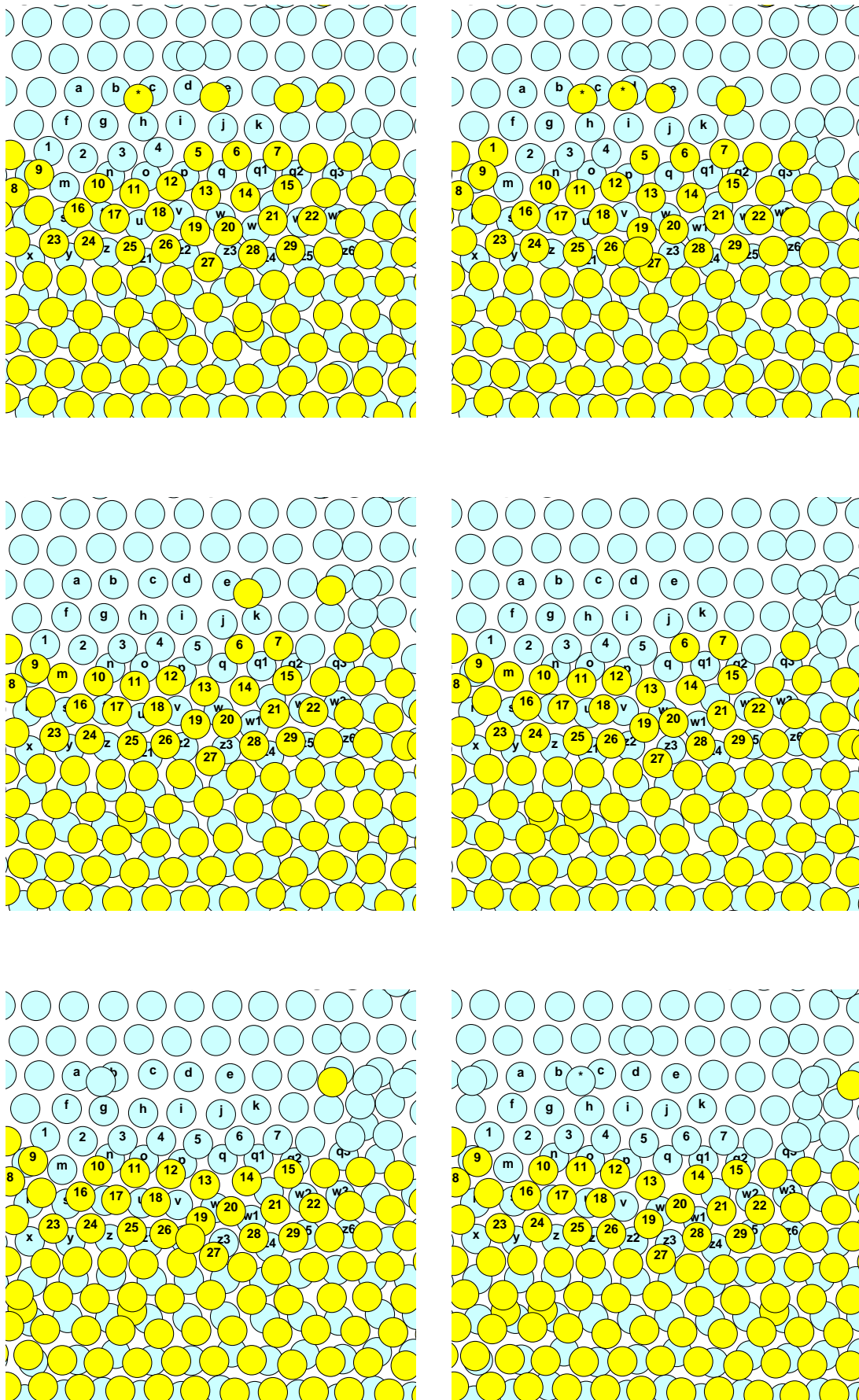


Figure 3.12: (color) Numbered atoms are initially top atoms, atoms marked by letters are initially second-layer atoms.

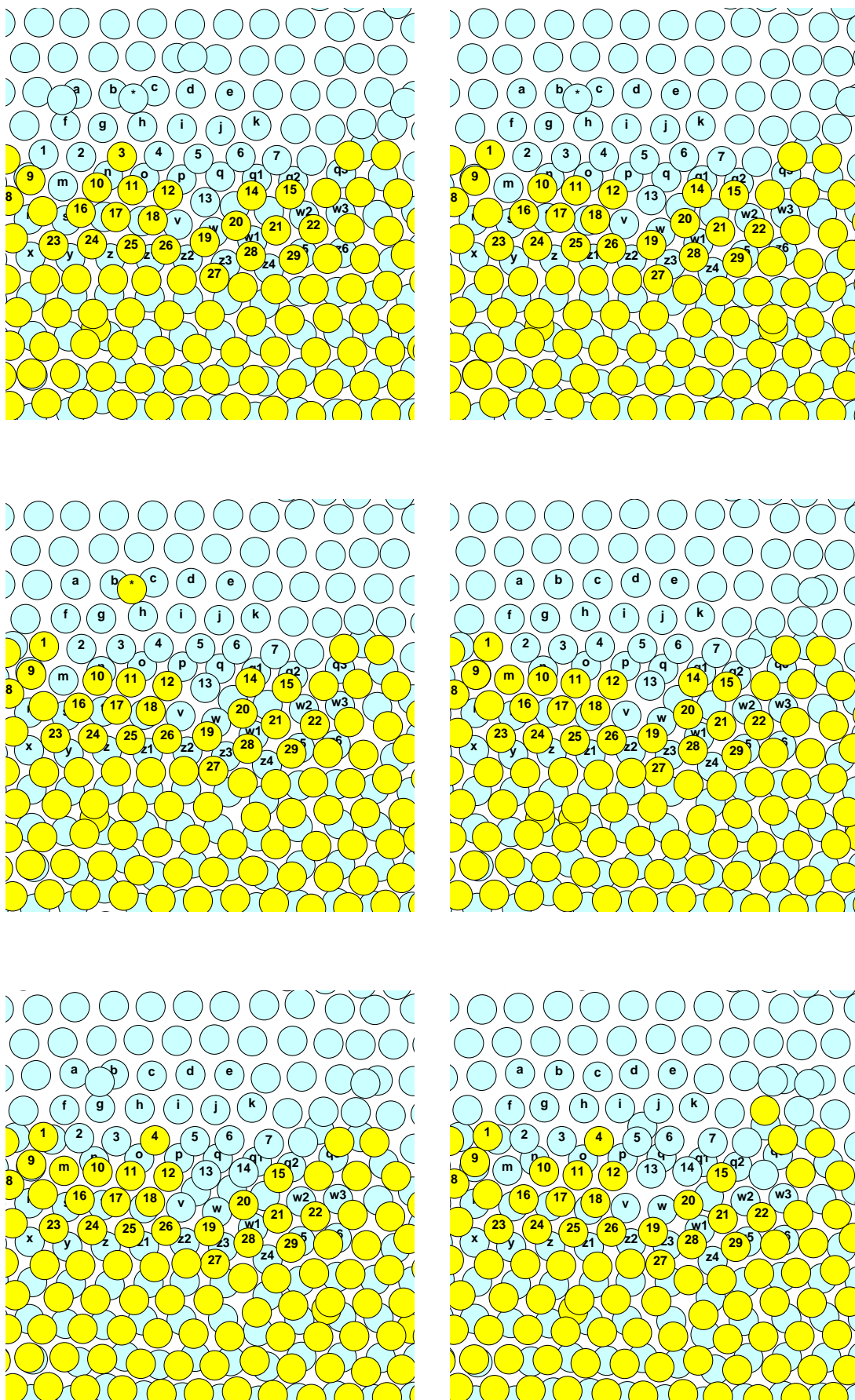


Figure 3.13: (color) Step has retracted and a whole line of atoms (1-7) passed from the step rim to the second layer.

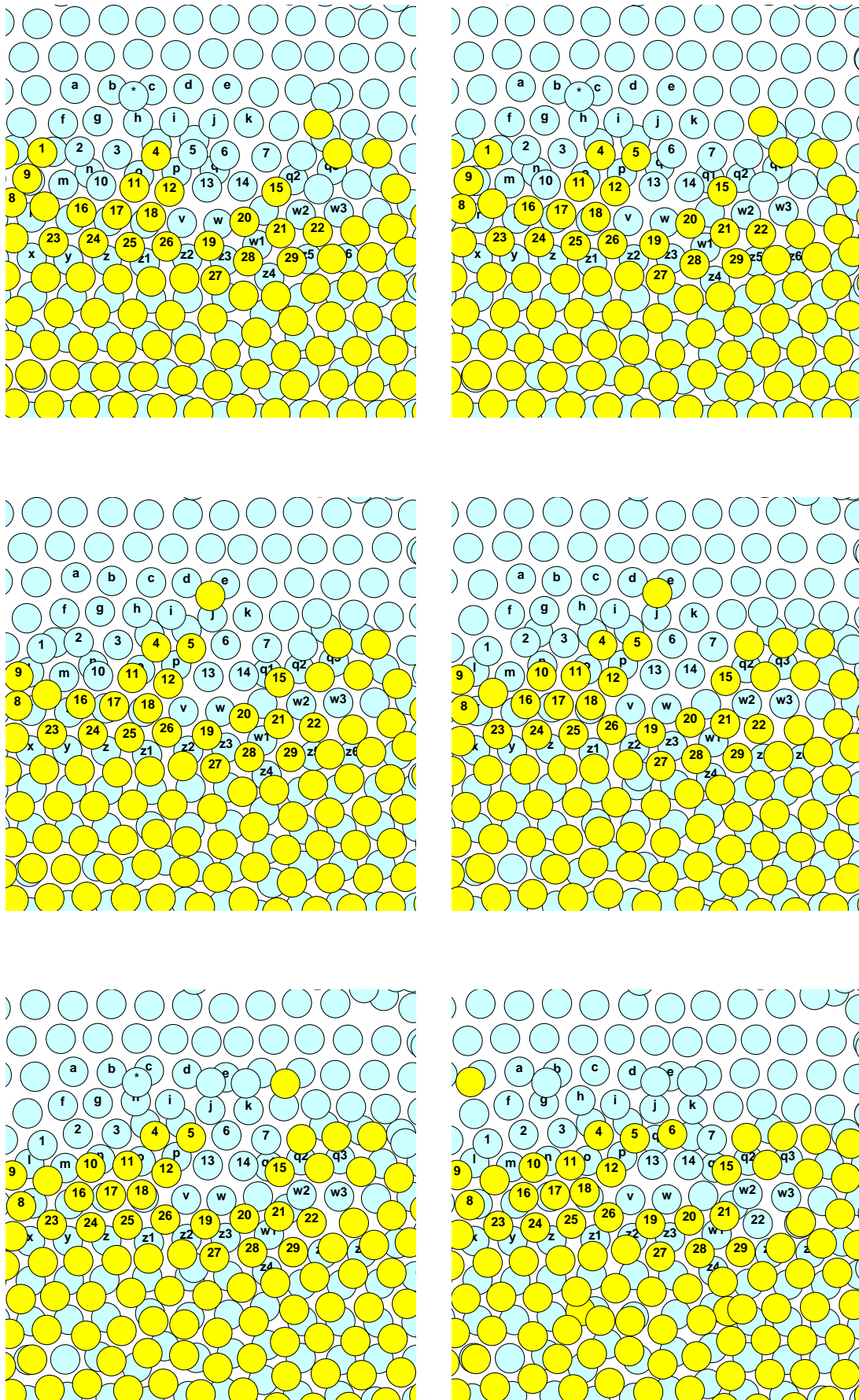


Figure 3.14: (color) Atoms 13, 14, 6 and 7 are part of the reconstruction of the uncovered zone of the second layer.

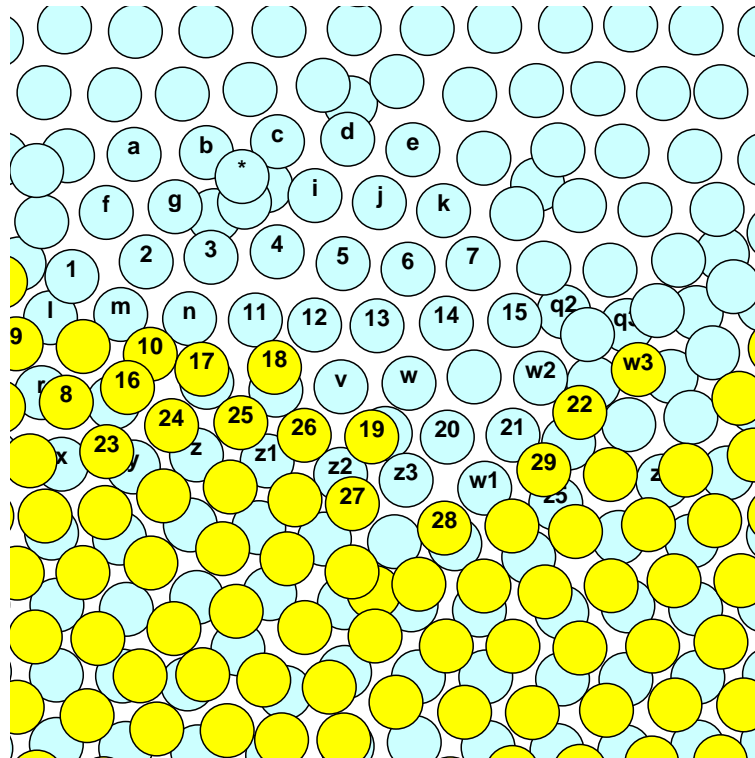


Figure 3.15: (color) The final situation, with evident shrinking of the step (70 ps of simulation have been completed). The uncovered zone has become reconstructed, and atoms 1 – 7, formerly at the step edge, as well as 11 – 15, formerly second line, have been incorporated into the lower terrace. Note also the new large wiggleness of the retracted step.

### 3.6 The $(53\ 1\ 1)$ vicinal and the step-reconstruction interaction: orientational details

In the previous sections we investigated the possible role played by a step in the reconstruction-deconstruction scenario, by means of single-step simulations. We have also carried out multi-step simulations, in particular of  $(m\ 1\ 1)$  vicinals, with  $m$  very high, *i.e.*  $m = 53$ . The choice of  $m = 53$  was intentional: it was shown that the width of a terrace is in this case *ideal* to accommodate 5 extra rows of atoms, giving rise to a structure with 5 reconstruction units on each terrace. The orientation of this surface is therefore energetically stable (magic vicinal) [33]. The sample was a 12105 particles slab, with 3 bulk rows blocked, and the surface was made up of 2 steps and 2 wide, reconstructed terraces.

Because the number of steps is now even, standard PBC are wholly appropriate. The cycle of simulation was similar to that followed in the flat surface case. The



Figure 3.16: The reconstructed (53,1,1) surface at  $T = 300K$  (side view). Note the 5 extra lines on each terrace.

results obtained from this surface can be summarized as follows:

- The step actually represents an attractive or a repulsive barrier for the reconstruction. We can see from Figure 3.17 that there is a zone of the surface where the  $O_6$  order parameter is lower, even at temperatures at which the reconstruction should be strong, and this zone is actually in the portion of lower terrace near the step. On the other hand the reconstruction is stronger close to the upper rim of the step.
- The surface shows domains with different hexagonal orientation, and this is consistent with experimental data [31].
- There is a zone where there is neither hexagonal nor square order, even at relatively low temperatures, indicating that the non-reconstructed phase at low temperature is not simple to describe.

### 3.6.1 Example of evolution at 970 K and at 1250 K

Figure 3.17 shows the results obtained after a long annealing at a temperature below  $T_D$ . We find that starting with terraces of equal width, and an initial surface density 1.24, one of the steps retreated visibly (the other appears to be pinned to the corresponding rigid bottom step, probably due to insufficient thickness). The surface density is roughly uniform, while the orientational order

parameter is greatly reduced in the lower terrace near the step. The stripes preferred orientation is orthogonal to the step, but we observed also terraces with stripes parallel to the step itself. This is probably due to the particular geometry chosen: we have cooled the slabs from a high temperature, where the surface is completely disordered. Upon cooling, the mobility decreases abruptly and the hexagonal domains can 'freeze' with different orientations. The presence of the step represents a perturbation to the orientational order parameter right under the step itself.

By heating the same system above  $T_D$ , the orientational order parameter drops (Figure 3.18), but again the density shows no decrease. The disagreement with the X-ray data fit above  $T_D$  therefore remains. No final word can be said, however: although the value of 53 for the first Miller index of the vicinal is quite high, the interaction between the steps can hardly be ignored.

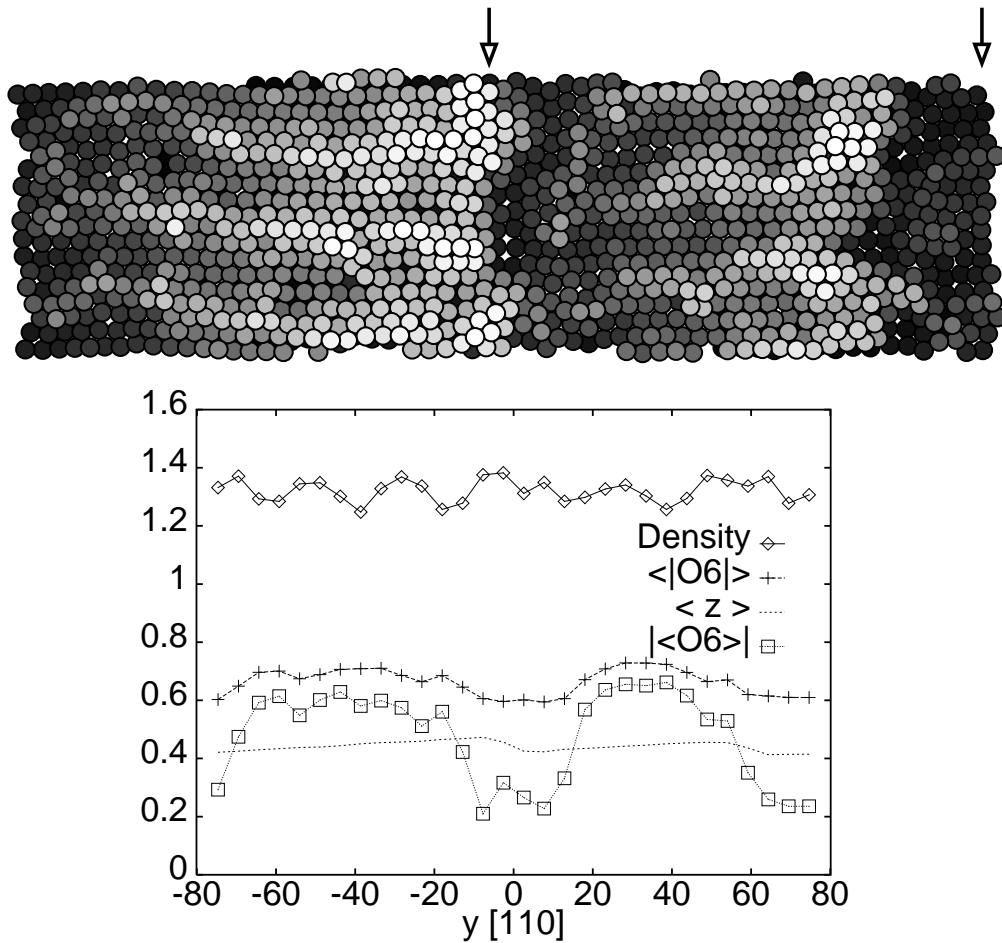


Figure 3.17: Simulation results for a (100) vicinal surface with a low density of steps, Au(53,1,1) at 970 K. Same notations and conventions as in previous figures. Arrows indicate the step positions at the bottom (rigid) surface of the slab, which also coincide with those of the step surface at  $T = 0$ . One of the two steps has retreated, thus increasing the lateral density. Note that orientational order is stronger on the rim of a step, and is depressed at the foot of a step. Note that in the slab shown stripes orient preferentially normal to the steps; upon cooling from high temperatures, we have observed both terraces with stripes parallel to the step and terraces (like the ones shown here) normal to the step. In this case, however, the slab size along  $x$  was small and exactly 15 nearest neighbours distances, which is magic ( $3 \times 5$ ) and determined the preferential  $x$ -reconstruction.

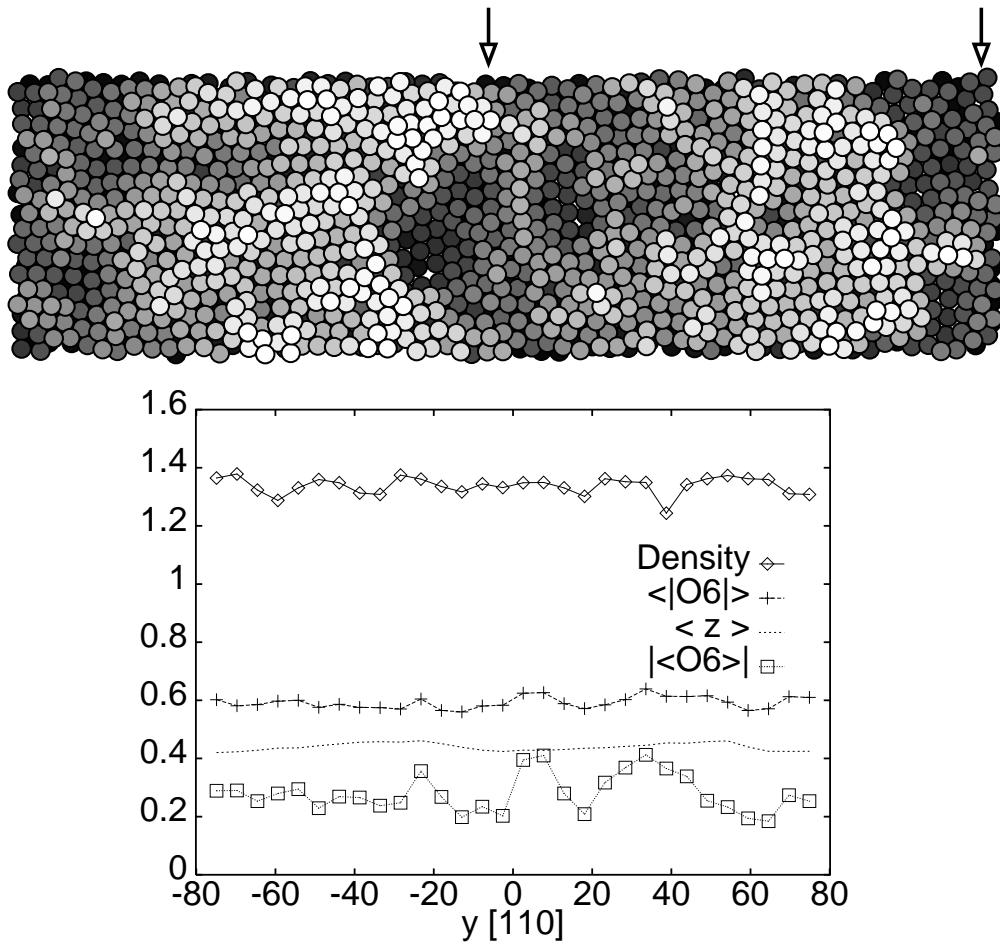


Figure 3.18: Simulation results for a surface with steps, Au(53,1,1) at  $T = 1250$  K ( $T > T_D$ ). Same notations and conventions as in previous figures. The steps are heavily meandering. There is no more long-range order, but short-range order and lateral density remain high.

Moreover, the width of the terrace is again too small for it to reproduce the physics of a flat (100) surface; it seems necessary a grand-canonical treatment of the problem, to allow the system to increase or decrease its density without changing its features introducing craters or shortening the terraces. Work in this direction is discussed in Chapter 4.

### 3.7 Higher step density: the (17 1 1) vicinal surface

In this section we will describe preliminary results concerning the behaviour of other, more stepped and thus more tilted, vicinal surfaces. The description of

our results is preceded by a short report about experimental data about faceting of the (100) vicinal surfaces.

### 3.7.1 Reconstruction-induced faceting: experimental review

In reconstruction-induced faceting [30, 37] the surface of a crystal can ‘choose’ between a reconstructed phase with low energy of the terraces and high step formation energy (favourable at low tilting angles), and another deconstructed phase with higher terrace energy but lower step formation energy, which is favoured at high step density; the lower envelope of the two phases can lead in this case to a concave form for the free energy density curve (see Figure 3.19). If the tilting angle belongs to this concave zone of the free energy profile, a simple Maxwell construction leads to faceting between a reconstructed phase at  $\theta = 0$  and a non-reconstructed phase with  $\theta = \theta_f$ .

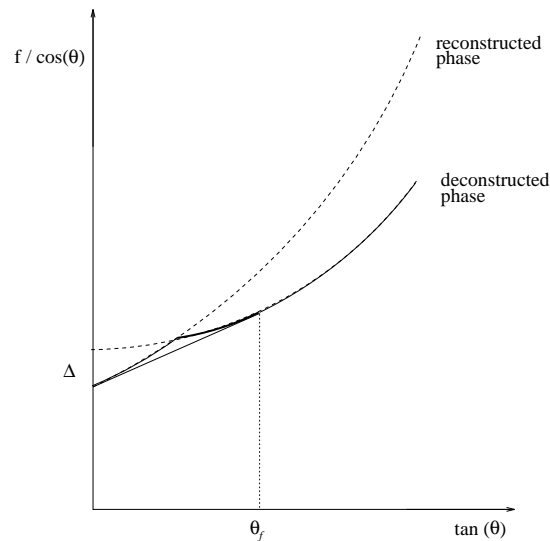


Figure 3.19: Reconstruction-induced faceting. Two free energy curves corresponding to different phases of the surface; the envelope is concave and the faceting separation occurs, with the angle  $\theta_f$  determined by the Maxwell construction.

Faceting may occur via a variety of mechanisms: for example, the adsorption of  $O_2$  induces faceting of stepped  $Ag(110)$  [38] (in this case the two phases among which the surface has to choose are the clean and the adsorbed one). It has been hypothesized that the faceting transformation of stepped  $Si(113)$  at 1220 K occurs by virtue of a direct attraction between steps [39] (in this case

the overall free energy would be concave due to this attractive interaction). Surface non-melting of certain faces induces phase separation between molten and non-molten surfaces of stepped Pb(111)[40]. The case of ‘magic vicinals’ is yet another interesting one: magic vicinals are stepped surfaces whose orientation lies near a facet (flat) orientation; they are stabilized by the near commensurability between the step separation and the reconstruction period. Such surfaces were originally predicted for Au(100)[33], and have been observed experimentally for Pt(100) [41] and for Au(100) [42, 43].

Our focus will be on the case when faceting is induced by surface reconstruction. The uniformly stepped surface is in this case replaced by coexistence among reconstructed facets and unreconstructed, stepped regions: the free energy cost of a step is larger on the reconstructed surface than on the unreconstructed surface. This kind of faceting has been observed in Si(111)[44], induced by the  $(7 \times 7)$  reconstruction; in Pt(001) [41] and in Au(100) [42], induced by the hexagonal reconstruction. In the remainder of this section we will consider the case of Au(100).

In Figure 3.20 we reproduce the experimental phase diagram for Au(100) from [42].

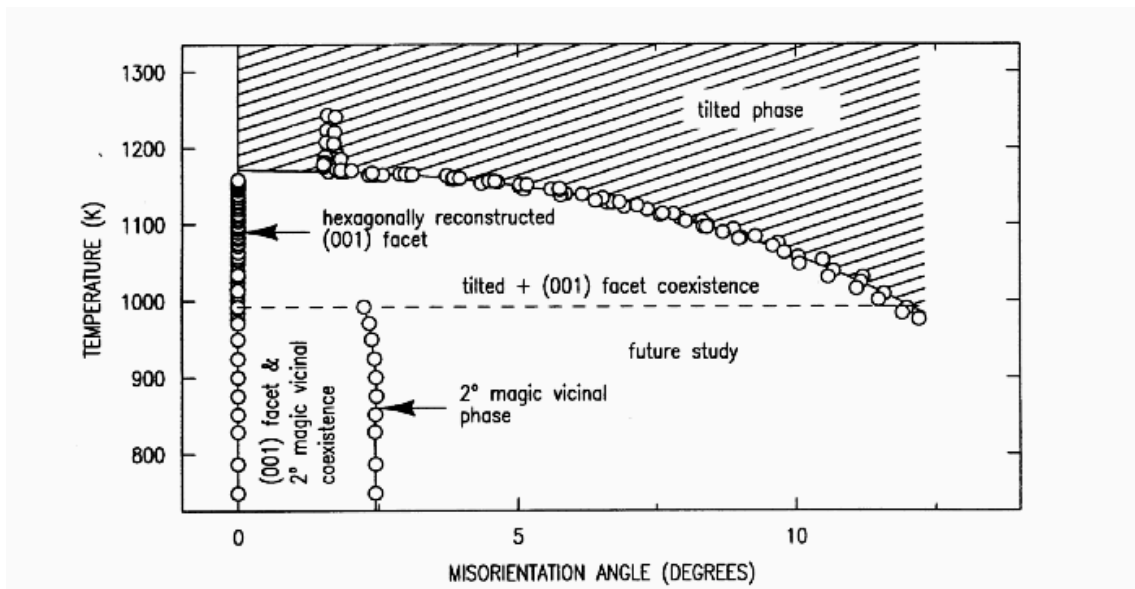


Figure 3.20: The experimental phase diagram for Au [42].

The flat surface undergoes a first order phase transition from hexagonal to

unreconstructed at 1153 K. A surface miscut towards the (110) direction by  $1.4^\circ$  is stable at high temperatures, but undergoes a faceting phase separation with a faceting angle which varies with temperature, with the power law  $\tan \theta_F = (T - T_D)^\gamma$ , where  $\gamma \simeq 0.44$  for Au(100).

To describe phenomenologically the variation of the faceting angle, one can consider the usual Taylor expansion (valid for small angles) for the free energy both for the reconstructed and for the unreconstructed phase, assuming a reconstruction energy  $\Delta$ :

$$\frac{\gamma_R}{\cos \theta} = \sigma_{0R} + \frac{\beta_R}{h} |\tan \theta| + g_R |\tan \theta|^3 \quad (3.5)$$

$$\frac{\gamma_U}{\cos \theta} = \sigma_{0R} + \Delta + \frac{\beta_U}{h} |\tan \theta| + g_U |\tan \theta|^3, \quad (3.6)$$

where  $\beta_R > \beta_U$  expresses the higher cost of a step on the reconstructed surface. We would like to point out that this is only a simple framework, since it does not explain more complicated situations, such as ‘magic vicinals’. The Maxwell construction, *i.e.* the condition for phase separation leads to the well-known  $\gamma = 1/3$  power law for the faceting angle:

$$|\tan \theta_F| = \left| \frac{\Delta}{2g_D} \right|^{\frac{1}{3}}. \quad (3.7)$$

Near the deconstruction temperature  $T_D$ ,  $\Delta$  goes to zero linearly with  $(T_D - T)$  and a reasonable, but not perfect agreement with the experimental phase diagram ( $\gamma = (0.44 \pm 0.05)$ ) is obtained.

As it is discussed in [42], the exponent of 0.44 found from experimental data is in agreement with the one obtained in an analogous case for Pt [41], *i.e.*  $(0.49 \pm 0.05)$ ; nevertheless, the untilted (100) surface of Pt is rough at high temperature, whereas Au(100) is flat. A phase diagram with an exponent of  $1/2$  is compatible with a term in  $(\tan \theta)^2$  in the free energy of the deconstructed phase, and this is exactly the case for the Pt case. Since the exponent for Au is 0.44, this would suggest a crossover in the deconstructed phase from a flat untilted surface to a rough stepped surface at high tilting. The nature of this flat untilted surface is unclear.

### 3.7.2 Simulation of vicinal surfaces

The choice, and consequently the compromise, to be made is between large slabs, with long equilibration times but a final state closer to the experimental one, and small samples with smaller equilibration times but a final state more affected by finite-size effects.

We started with large slabs with a very large surface area and observed that the times of equilibration of such samples were so high that many months of CPU time would have been necessary to obtain a non-noisy signal. In particular, a source of problem was originated by the fluctuation of the steps in the  $x$  direction (parallel to the step).

The next attempt was therefore to reduce considerably the size of the sample, especially in the  $x$  direction. In this way we could observe the first precursor signals of faceting with more clarity, and focus on the more interesting temperatures and orientations.

The same path of simulation was followed for a large number of vicinals, *i.e.* ( $M\ 1\ 1$ ) with  $M$  odd and ranging from 11 to 35. A typical sample was made up of two steps, and very thin in the  $x$  direction.

#### Step bunching

In this section, we would like to show two examples of the steps pairing mechanism originating the phenomenon of faceting. In Figure 3.21 and 3.22 the starting configuration is a  $(1\ 7\ 1\ 1)$  surface with four equally spaced steps; the figure shows a side view of the surface and few sublayers, doubled in the direction perpendicular to the step to simplify the observation.

In the first frames, only weak step pairing is observed. As the simulation ( $T = 1080\text{K}$ ) proceeds, the formerly separated steps begin to join together and at the end a ‘hill-and-valley’ structure is recognizable. This step bunching can be considered the onset of a faceting phase separation.

In Figure 3.23 and 3.24 a similar evolution path is described at  $T = 1050$ . The starting configuration is a couple of paired steps (doubled in the direction perpendicular to the step) which again tend to join together. In particular, after  $\sim 5\text{ ns}$  (nine-th frame in the figure) a clear bunching of all the steps is observed, but the small dimensions of the sample do not permit to conclude anything about the angle of faceting. It seems remarkable, however, that this hill

and valley structure has been observed on a wide range of vicinals: the set of picture presented is truly a ‘typical set of snapshots’, since the same behaviour was observed also in the other cases studied. This allows to conclude that step bunching is a general phenomenon occurring on this kind of vicinals of Au(100).

The step bunching is a precursor of faceting. Simulation and equilibration of a surface with a high number of steps is a huge task, which we could not address due to the high computational effort needed.

### Summary

The preliminary results obtained from these ‘wide spectrum’ simulations can be summarized as follows:

- Clear step bunching and, to some extent, faceting has been observed in a temperature range between 1000 and 1080K. This behaviour is consistent with the experimental results described by Watson and coworkers [42].
- The angle of faceting, which is presumed to depend on temperature according to (3.7), is very difficult to measure with sufficient precision to compare it with the experimental phase diagram.

However, step bunching was observed on all the vicinals studied; we claim that this behaviour is general in this framework and at the temperatures studied, signaling an onset of faceting of the kind described in section §3.7.1.

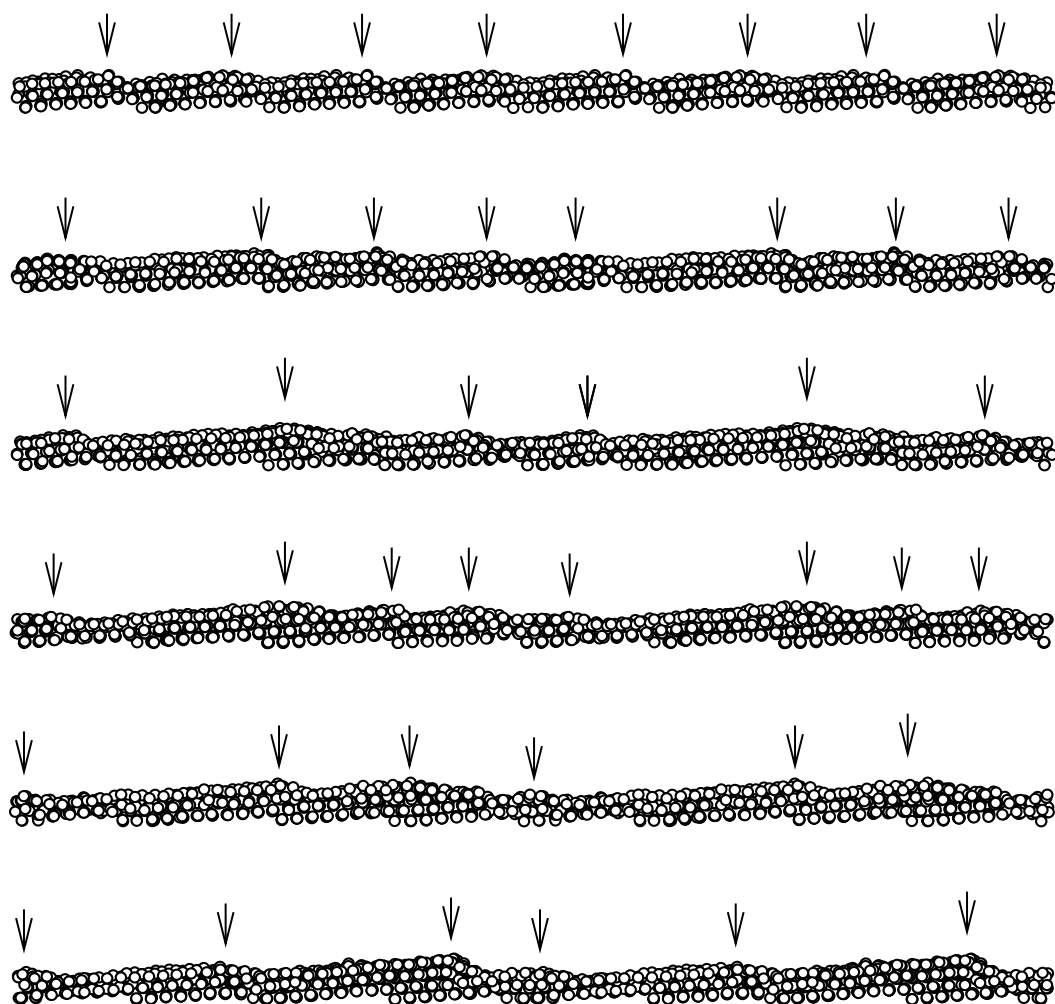


Figure 3.21: Time evolution of the surface ( $T=1080$ ) (side view). Note the attraction between the steps leading to bunching ( $\Delta t$  in these first 6 frames: .7 ns. 2 MD boxes are shown. Arrows indicate steps

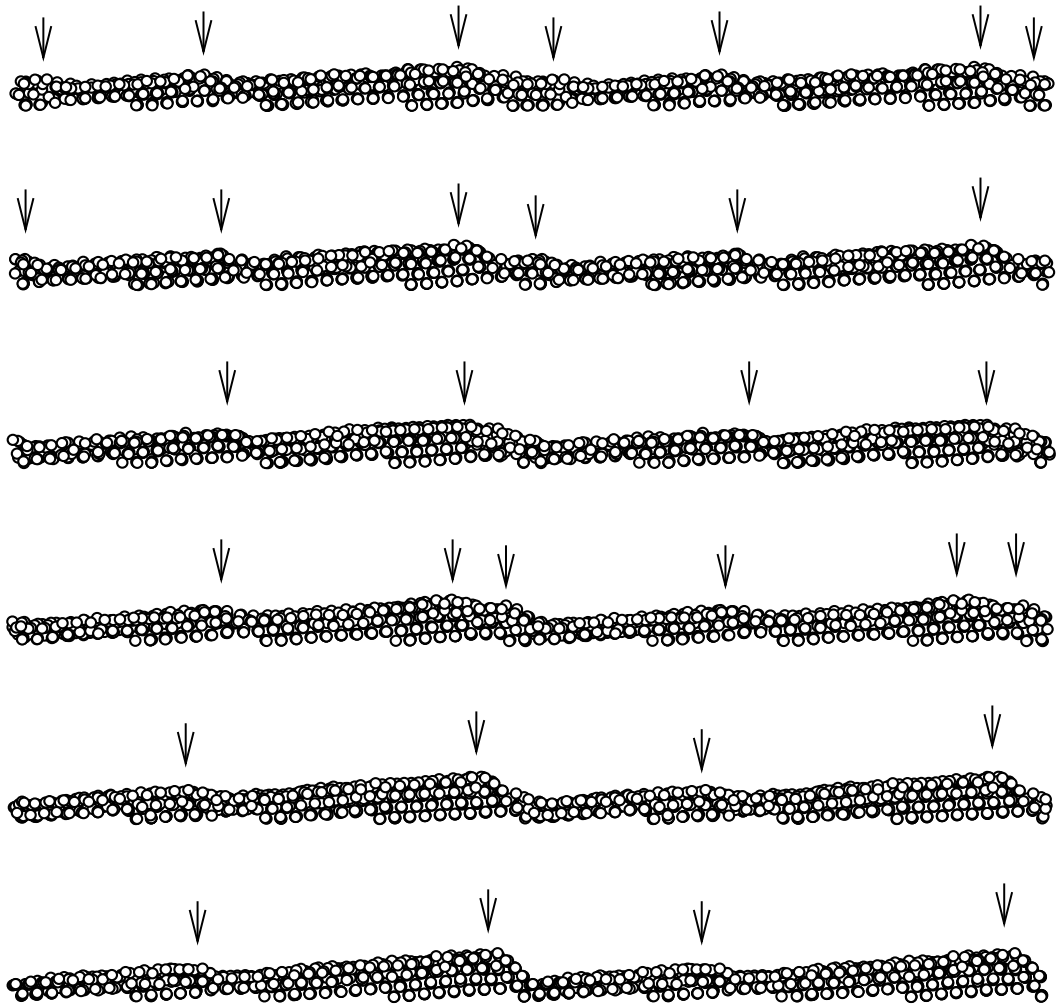


Figure 3.22: Continuation of the time evolution of the surface ( $T=1080$ ) (side view). ( $\Delta t$  in these 6 frames: .35 ns. 2 MD boxes are shown. Arrows indicate steps.

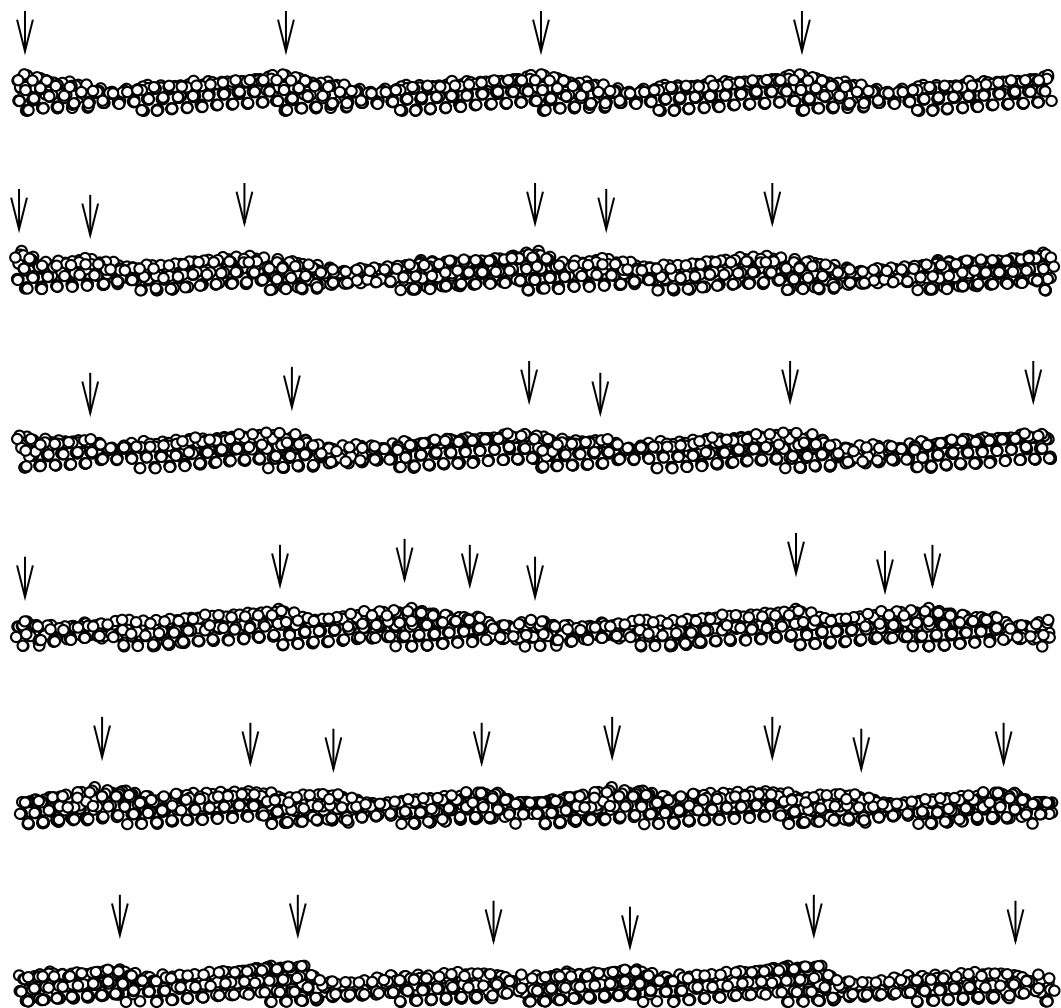


Figure 3.23: Time evolution of the surface ( $T=1050$ ) (side view). Note the attraction between the steps leading to faceting ( $\Delta t$  in the first 6 frames:  $.7 \text{ ns}$ , in the others:  $.35 \text{ ns}$ . 2 MD boxes are shown. Arrows indicate steps.

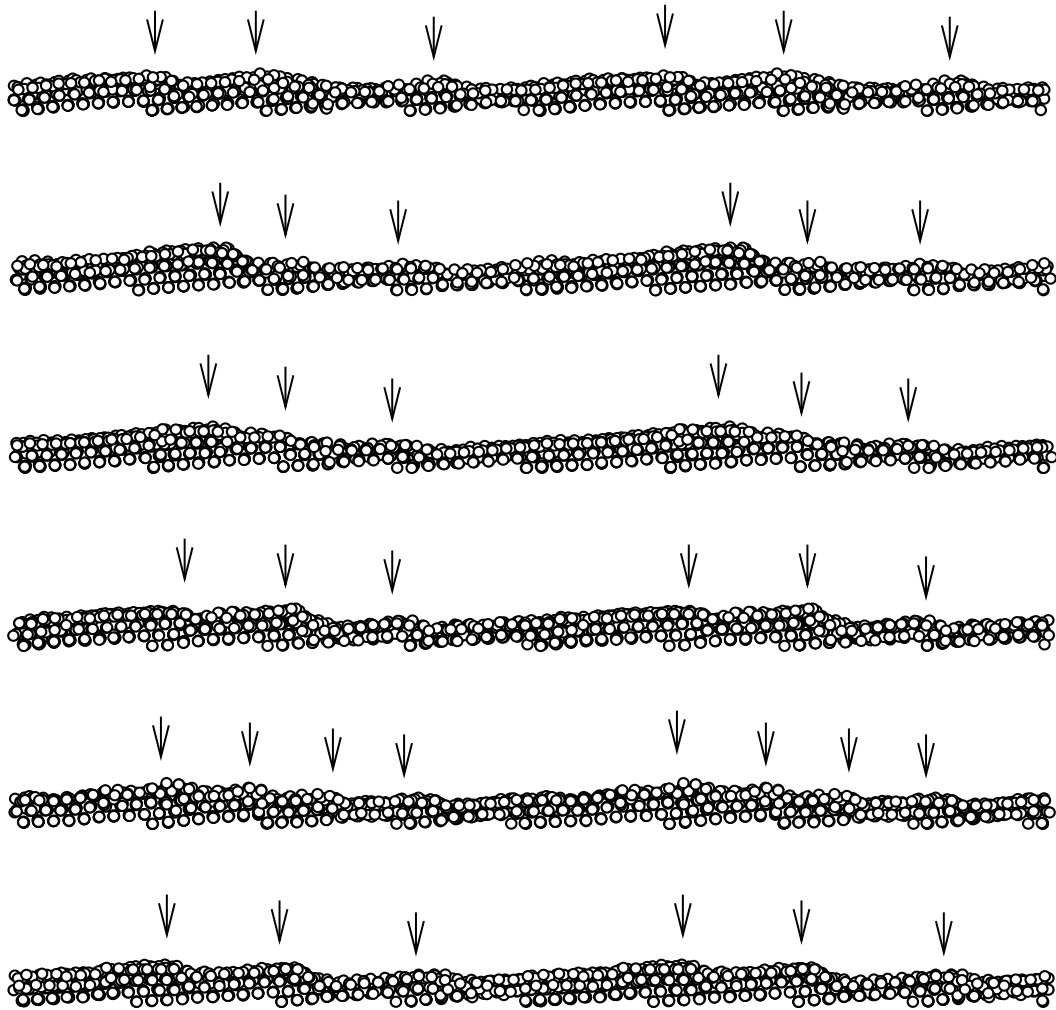


Figure 3.24: Continuation of time evolution of the surface ( $T=1050$ ) (side view). ( $\Delta t$  in these 6 frames: .35 ns. 2 MD boxes are shown. Arrows indicate steps.



# Chapter 4

## The Grand Canonical Monte Carlo method applied to surfaces

### 4.1 Introduction

We have encountered by now several examples of a standard difficulty occurring in realistic MD simulation: the number of particles is fixed at the outset and it is strictly conserved: the system is either microcanonical or canonical, but not grand-canonical. This poses a problem in all cases where a transition involving a change in the density of particles must be studied. The change of density of Au(100) with temperature described earlier, or the preroughening (PR) transition where the top layer coverage switches from nearly integer to nearly half integer, are striking examples. In these cases, nature would establish grand-canonical equilibrium through drift of particles to or from steps and defects, else through evaporation/condensation. However, these processes are generally too slow to be efficiently described by realistic MD, where the time scales must be contained within a ns or so.

Grand Canonical Monte Carlo or MD is in point of principle the obvious

way out of this problem. There are examples in the literature of both, but none specifically designed for a general surface problem. We therefore decided to build our own GCMC method, which we later applied to rare gas adsorption -involving preroughening- and to noble metal surface reconstruction involving density changes.

## 4.2 Algorithm

In this section we present a Monte Carlo algorithm which is suitable to surfaces. Concerning the statistical mechanical formulation, we follow essentially [45]. In grand canonical ensemble Monte Carlo (GCMC) the number of molecules can change, whereas the chemical potential is fixed. The simulations are carried out at constant  $V$ ,  $\mu$  and  $T$ , and the average of some property  $\mathcal{A}$  is given by:

$$\langle \mathcal{A} \rangle_{\mu V T} = \frac{\sum_{N=0}^{\infty} (N!)^{-1} z^N \int d\mathbf{r} \mathcal{A}(\mathbf{r}) e^{-\beta V(\mathbf{r})}}{\sum_{N=0}^{\infty} (N!)^{-1} z^N \int d\mathbf{r} e^{-\beta V(\mathbf{r})}}$$

$$z = \frac{e^{\beta\mu}}{\Lambda^3}; \quad \Lambda = \frac{h}{\sqrt{2\pi m k_B T}}.$$

Our implementation of GCMC is based on well known techniques [46], with modifications to improve the sampling efficiency in a system with a free surface. In particular, taking inspiration from an idea previously used for bulk liquids [47], we have restricted attempts to create or destroy particles to a region near the surface, where they are much more likely to be accepted. The application of such a method to surface physics requires some care, due to the particular geometry used: a slab with an upper free surface and some blocked layers in order to reproduce a semi-infinite bulk. It is clear that, when trying to create or destroy a particle, favorable sites can be found more easily at the surface with respect to the inner layers. It is therefore desirable to limit the creation trials to a ‘window’ surrounding the surface, as shown in Figure 4.1. The displacement moves are attempted on the whole system, and the grand canonical moves are applied only to particles with  $z$ -coordinate lying between  $z_1$  and  $z_2$ ; this simple trick significantly improves the rate of acceptance of these moves. Concerning the

move proposition strategy, it is possible to improve the algorithm by choosing a move from a set of  $M$ , according to a simple probability distribution, which is different depending on the particular interaction potential used.

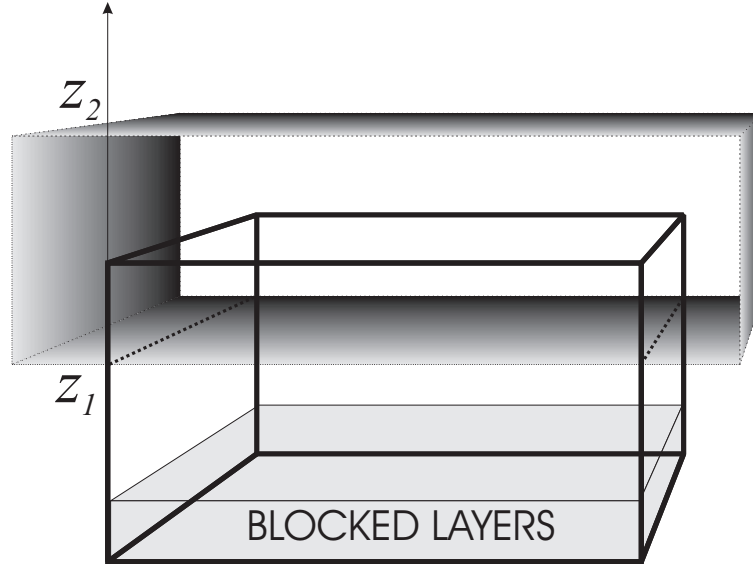


Figure 4.1: The geometry used in GCMC applied to surfaces: the lower layers of the slab are blocked, and no move is attempted within them; in the window  $z_1 < z < z_2$ , which surrounds the surface, creation and destruction moves are attempted.

### 4.3 Proposal matrix and detailed balance

In this section, we will follow Sokal [48] in the construction of a statistically correct Monte Carlo algorithm.

The idea of dynamic <sup>1</sup> Monte Carlo is to invent a stochastic process with state space  $S$  having a desired probability distribution  $\pi$  as unique equilibrium distribution. This stochastic process is always taken to be a Markov chain, that is a sequence of random variables  $X_i$  (with values in the phase space  $S$ ) such that transitions  $X_t \rightarrow X_{t+1}$  are specified by an initial distribution  $\alpha$  and a *transition probability matrix*  $P$ , defined so that  $\mathcal{P}(X_{t+1} = y \mid X_t = x) = p_{xy}$ . The *n-step transition probabilities* are defined as  $p_{xy}^{(n)} = \mathcal{P}(X_{t+n} = y \mid X_t = x)$ .

<sup>1</sup>Static methods are those that generate a sequence of statistically independent samples from a desired probability distribution, and are used in Monte Carlo numerical integration in low dimension. The term *dynamic* refers instead to a stochastic time evolution, which does not need to correspond to any real physical dynamics: the dynamics is simply a numerical algorithm, chosen on the basis of computational efficiency.

The simulation of the Markov chain  $P$  constitutes a legitimate Monte Carlo method for estimating averages with respect to  $\pi$  if the following two conditions are satisfied:

- (A) *Irreducibility*. For each pair  $x, y \in S$ , there exists an  $n \geq 0$  for which  $p_{xy}^{(n)} > 0$ .
- (B) *Stationarity of  $\pi$* . For each  $y \in S$ ,

$$\sum_x \pi_x p_{xy} = \pi_y. \quad (4.1)$$

A sufficient condition for (B) is the more popular *detailed balance condition*: for each pair  $x, y \in S$ ,  $\pi_x p_{xy} = \pi_y p_{yx}$ . The celebrated Metropolis method [49] satisfies detailed balance for a given distribution  $\pi$ .

We have to consider an arbitrary irreducible transition matrix on  $S$ , called  $P^0 = p_{xy}^{(0)}$ ; we will use this ‘proposal matrix’ to generate *proposed* moves  $x \rightarrow y$  that will then be accepted or rejected with probabilities  $a_{xy}$  and  $1 - a_{xy}$ . If a proposed move is rejected, then a “null transition”  $x \rightarrow x$  is made. Following again Sokal, the transition matrix  $P = p_{xy}$  of the full algorithm is

$$p_{xy} = p_{xy}^{(0)} a_{xy} \text{ for } x \neq y \quad (4.2)$$

$$p_{xx} = p_{xx}^{(0)} + \sum_{y \neq x} p_{xy}^{(0)} (1 - a_{xy}). \quad (4.3)$$

$P$  satisfies detailed balance for  $\pi$  if and only if

$$\frac{a_{xy}}{a_{yx}} = \frac{\pi_y p_{yx}^{(0)}}{\pi_x p_{xy}^{(0)}}, \quad (4.4)$$

for every pair  $x \neq y$ . This is obtained by setting

$$a_{xy} = F \left( \frac{\pi_y p_{xy}^{(0)}}{\pi_x p_{yx}^{(0)}} \right), \quad (4.5)$$

where  $F : [0, +\infty] \rightarrow [0, 1]$  is any function satisfying the following property:

$$\frac{F(z)}{F(1/z)} = z \quad \text{for all } z. \quad (4.6)$$

The choice suggested by Metropolis is  $F(z) = \min(z, 1)$ .

When the proposal matrix  $P^{(0)}$  is not symmetric, particular care has to be taken in order to satisfy eq.(4.5). Indeed, in the simple case in which  $P^{(0)}$  is symmetric, the condition (4.5) simplifies to

$$a_{xy} = F\left(\frac{\pi_y}{\pi_x}\right). \quad (4.7)$$

According to the previous prescription, if  $\frac{\pi_y}{\pi_x} > 1$ , the move is accepted, otherwise a random number  $r$  uniformly distributed on  $[0, 1]$  is drawn, and the proposal is accepted if  $r \leq \frac{\pi_y}{\pi_x}$ .

At this point, we will consider the Grand Canonical ensemble case. The most common method for generating the chain for a fluid was proposed by Norman and Filinov [50]; there are three different types of move:

1. an atom is displaced (either small, or large displacement);
2. an atom is destroyed;
3. an atom is created at a random position in the fluid.

In the first move, the method is identical to canonical ensemble MC, *i.e.*, a move is accepted or rejected with a probability  $\min(1, e^{-\beta\delta V_{yx}})$ , where  $\delta V_{yx}$  is the potential energy difference between initial state  $m$  and final state  $n$ .

For destruction and creation moves,  $\pi$  is proportional to

$$e^{-\beta(V(\mathbf{r}) - N\mu) - \ln N! - 3N \ln \Lambda + N \ln V}; \quad (4.8)$$

when a particle is destroyed, the ratio of the probabilities of initial and final states is ( $x$  is a state with  $N$  particles,  $y$  a state with  $N - 1$  atoms)

$$\begin{aligned} \frac{\pi_y}{\pi_x} &= e^{-\beta\delta V_{yx}} e^{-\beta\mu} \frac{N \Lambda^3}{V} = \\ e^{-\beta\delta V_{yx} + \ln\left(\frac{N}{zV}\right)} &\equiv e^{-\beta\delta D_{yx}}. \end{aligned} \quad (4.9)$$

A destruction move is accepted with probability  $\min(1, e^{-\beta\delta D_{yx}})$ . Conversely, for a creation step ( $N \rightarrow N + 1$ ), the ratio is

$$\begin{aligned} \frac{\pi_y}{\pi_x} &= e^{-\beta\delta V_{yx}} e^{\beta\mu} \frac{V}{(N + 1) \Lambda^3} = \\ e^{-\beta\delta V_{yx} + \ln\left(\frac{zV}{N+1}\right)} &\equiv e^{-\beta\delta C_{yx}}, \end{aligned} \quad (4.10)$$

and the move is accepted with the probability  $\min(1, e^{-\beta\delta C_{yx}})$ .

When the proposal matrix is not symmetric (as is the case described in the following section), the ratio  $p_{yx}^{(0)}/p_{xy}^{(0)}$  must be calculated. In the following section, we will discuss the implementation of our algorithm, and the case of a non-symmetric proposal matrix will be encountered.

## 4.4 Implementation of the GC algorithm

The implementation of the method, standard for pair potential, is slightly cumbersome, but still feasible, in the case of a many-body potential, like the glue model. In order to maintain the  $O(N)$  scaling dependence of the algorithm, the system was divided into cells. The many-body character of the potential affects the calculation of  $\delta V_{yx}$ . If a particle is removed from the system, in the pairwise case  $\delta V_{yx}$  is simply the potential energy of that particle. In the many-body potential case, all the neighbours of this atom change their coordination, and therefore their energy. The same considerations can be applied to the creation of a new particle. In our implementation, we keep therefore memory of: the coordination of the atoms, the glue term and the two body term. The glue term  $U(n)$  can also be used as a approximate, but fast and efficient criterion for preselection of the atom to destroy or of the coordinate where to create. Concerning destruction, for example, a set  $B_D$  of  $M$  atoms is chosen at random, and the Monte Carlo move is attempted from the state  $x$  with  $N$  particles to the state  $y$  without atom  $i$  ( $i \in B_D$ ) with the following probability:

$$p_{xy}^{(0)} = \frac{\exp\left(\frac{U(n_i)}{|U_0|}\right)}{\sum_{j \in B_D} \exp\left(\frac{U(n_j)}{|U_0|}\right)}. \quad (4.11)$$

Therefore, an atom with a good glue energy has a low probability to be chosen. The same scheme can be applied to creations. In order to calculate  $p_{yx}^{(0)}$ , we start in a world of  $N - 1$  particles; imagine a set  $B_C$  atoms: the first atom is  $i$ , the other  $M - 1$  are chosen at random. The proposal matrix element is therefore:

$$p_{yx}^{(0)} = \frac{\exp\left(-\frac{U(n_i)}{|U_0|}\right)}{\sum_{k \in B_C} \exp\left(-\frac{U(n_k)}{|U_0|}\right)}; \quad (4.12)$$

and the ratio to be inserted into (4.5) is simply

$$\frac{p_{yx}^{(0)}}{p_{xy}^{(0)}} = e^{\left(-2\frac{U(n_i)}{|U_0|}\right)} \frac{\sum_{j \in \mathbf{B}_D} \exp\left(\frac{U(n_j)}{|U_0|}\right)}{\sum_{k \in \mathbf{B}_C} \exp\left(-\frac{U(n_k)}{|U_0|}\right)}. \quad (4.13)$$

A suitable value for  $M$  is about 5 for a glue system, whereas the right probability for displacement is not 0.5, like in other MC simulations<sup>2</sup>, but lower ( $\simeq 0.25$ ) for the following reason. In metals, the acceptance probability for creations and destructions is very low. Due to the highly cohesive potential, it is very difficult to insert an atom in a dense or compact layer. If the rate of acceptance for creation/destruction is too high, the out of equilibrium configurations so created cannot be efficiently annealed by a suitable number of destructions and creations. This fact may show up for example with an unphysical low temperature surface initiated melting; this event, though theoretically acceptable as a particular exploration of the phase space by the Markov chain during the simulation, is undesirable because of difficulties in obtaining a perfect recrystallization from a molten state.

## 4.5 Demonstration of the method

We have tested out method with two typical cases of reconstruction, the missing row (110) and the quasi-hexagonal (100). As stated in a number of previous papers, these reconstructions involve a consistent density change at the surface. The missing row case is useful because it allows to show a rather general tuning procedure of the chemical potential.

### 4.5.1 Reconstruction of Au(110)

In the missing row reconstruction, a whole  $[1\bar{1}0]$  row every two is removed from the surface, whereas in (100) the quasi-commensurability of six  $[110]$  rows over five substrate lines produces a triangular overlayer which is stable up to  $\sim 1100 K$ .

---

<sup>2</sup>The value of 0.5 is usually chosen on the basis of computational convenience, but is not proven to be optimal. Lower acceptance ratio have in some cases shown to allow a more efficient sampling of the phase space. For a discussion about this point, see [45], p. 121.

We started from a perfect, non reconstructed (110) of Au; top view is visible in Figure 4.3(a). We carefully tuned the chemical potential  $\mu$  in order to obtain equilibrium. Starting from a small slab (40 atoms at surface and 16 layers) we were able to obtain a perfectly reconstructed surface after relatively few ( $\sim 10000$ ) MC steps. In Figure 4.2 the behaviour of  $N$  is shown, whereas in Figure 4.3(b) the final state is shown; as it can be seen from the figure, whole rows are removed and the  $(1 \times 2)$  pattern is obtained. The chemical potential is tuned by bisection of an interval bounded by high values (where indefinite growth is observed) and low values (where indefinite desorption happens) of  $\mu$ . The asymptotic limit extracted from this procedure is the correct value of the chemical potential.

At the correct chemical potential of  $-3.92\text{eV}$  (temperature is about  $500\text{K}$  for all simulations) the number of particles no longer varies for several hundred of thousand steps, as it can be seen from Figure 4.2.

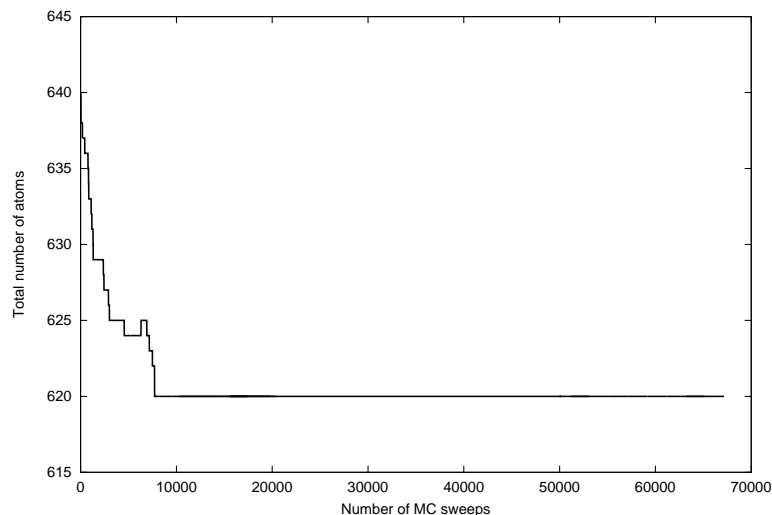


Figure 4.2: The number of atoms in the (110) surface we considered. The number equilibrates to the  $(2 \times 1)$  missing row value.

We have repeated the simulation with a larger slab (160 atoms at the surface), the reconstruction is obtained, but only locally and so called ‘white-black’ defects appear: in a certain zone atoms from odd rows are removed; in other zones atoms from even rows are destructed; this leads to defects. Once the  $2 \times 1$  structure was obtained locally the simulation times needed to correct the naturally arisen defect were too large.

Once the problem is identified, a better result can be obtained by ‘suggesting’ the correct structure to the simulation: we have removed a single atom from the ‘even’ rows of the surface, and the number of defects became significantly lower.

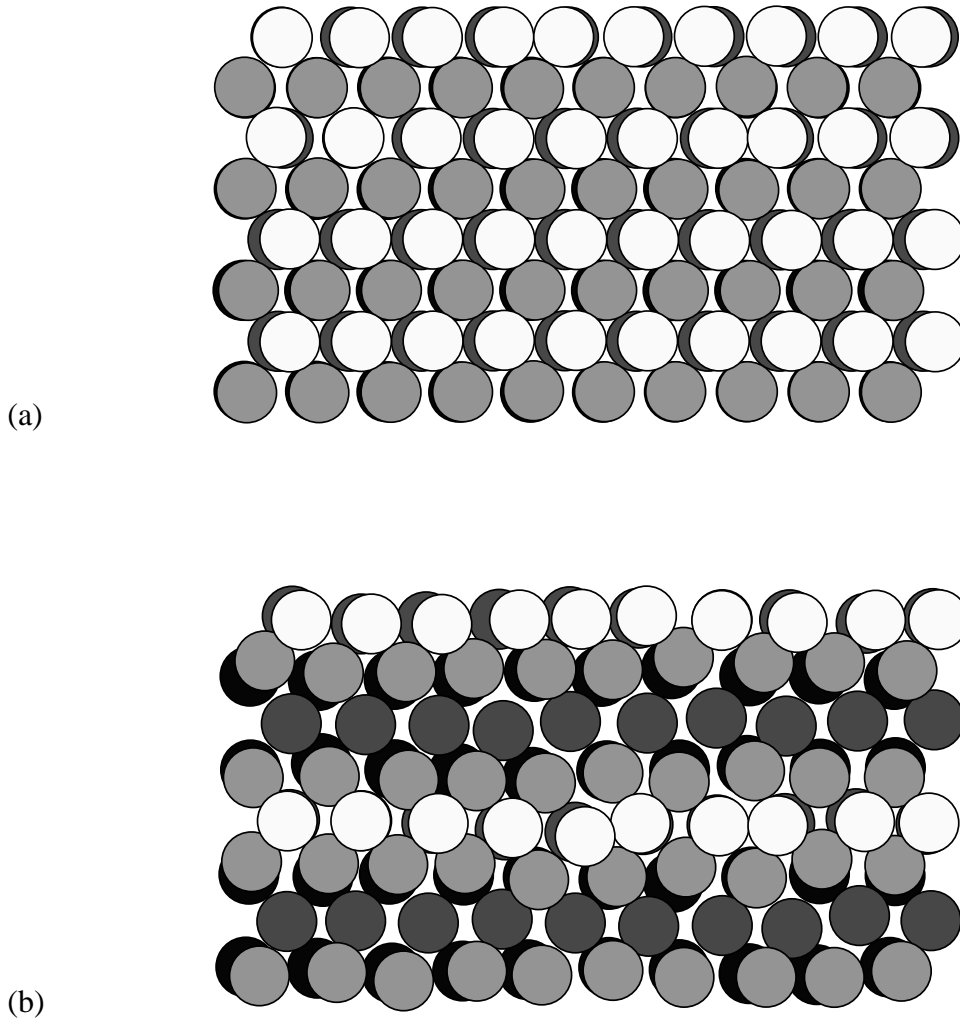


Figure 4.3: (a) The initial configuration of a (110) surface of gold (top view). (b) After the MC simulation, the equilibrium state is the  $(2 \times 1)$  reconstructed state.

## 4.5.2 Hexagonal reconstruction of Au(100)

Concerning Au(100), experimental details of the reconstruction have been recalled in previous chapters of this thesis. In this framework, we have used our GCMC to simulate two different systems at low temperature: a non-reconstructed surface (1) and a reconstructed quasi-hexagonal surface (2) (see for detail Chap-

ter 3, and we found the following results:

1. upon adsorption of atoms on the square top layer, the adatoms are included and the equilibrium state of the surface is, correctly, the  $(5 \times 1)$  reconstructed quasi-hexagonal state;
2. upon adsorption of atoms on the reconstructed layer, another reconstructed layer forms, and the former first layer, now covered, deconstructs immediately into a nearly regular, square  $(100)$  layer.

The surface density  $\rho_{(s)}$  for system (a) continuously changes from the bulk value to the hexagonal value. The chemical potential is  $\mu = -3.92\text{eV}$  and  $\rho_{(s)} >$  levels up at a nearly correct value of 1.30. All simulations are performed at  $T = 800\text{ K}$ . Figure 4.4 shows the initial unreconstructed state, an intermediate state with hexagonal zones which begin to form, and the equilibrium final state, triangularly ordered.

For system (b) the evolution of the number of atoms of the ad-layer and the population of the first two adsorbed layers are shown in Figure 4.5. The density of the first layer decreases nearly to the bulk value when the ad-layer has completed its growth, and completes its square ordering when another adlayer has adsorbed on it.

This results show that the GCMC simulation method is efficient also on the microscopic scale: structural phase transitions involving strong density changes and rearrangement of atoms are correctly driven by the grand canonical Markovian chain we used in order to sample this particular statistical ensemble. Not only the correct density is achieved, but also an almost perfect short-range order is obtained both in the reconstructed top layer and in the square bulk layers. This facts is remarkable, if one keeps into account the fact that an off-lattice model was used and no constraints on the lattice structure were given. We must give, of course, credit to the glue potential we have used [13], but we are confident that the interplay between efficient phenomenological potentials and particle-non-conserving algorithms such as the one just described will lead to interesting predictions in the field of structural transitions at surfaces.

Summarizing, these two simple tests indicate the feasibility of a surface GCMC simulation, applied in particular to metals modeled by classical many-body (glue) forces.

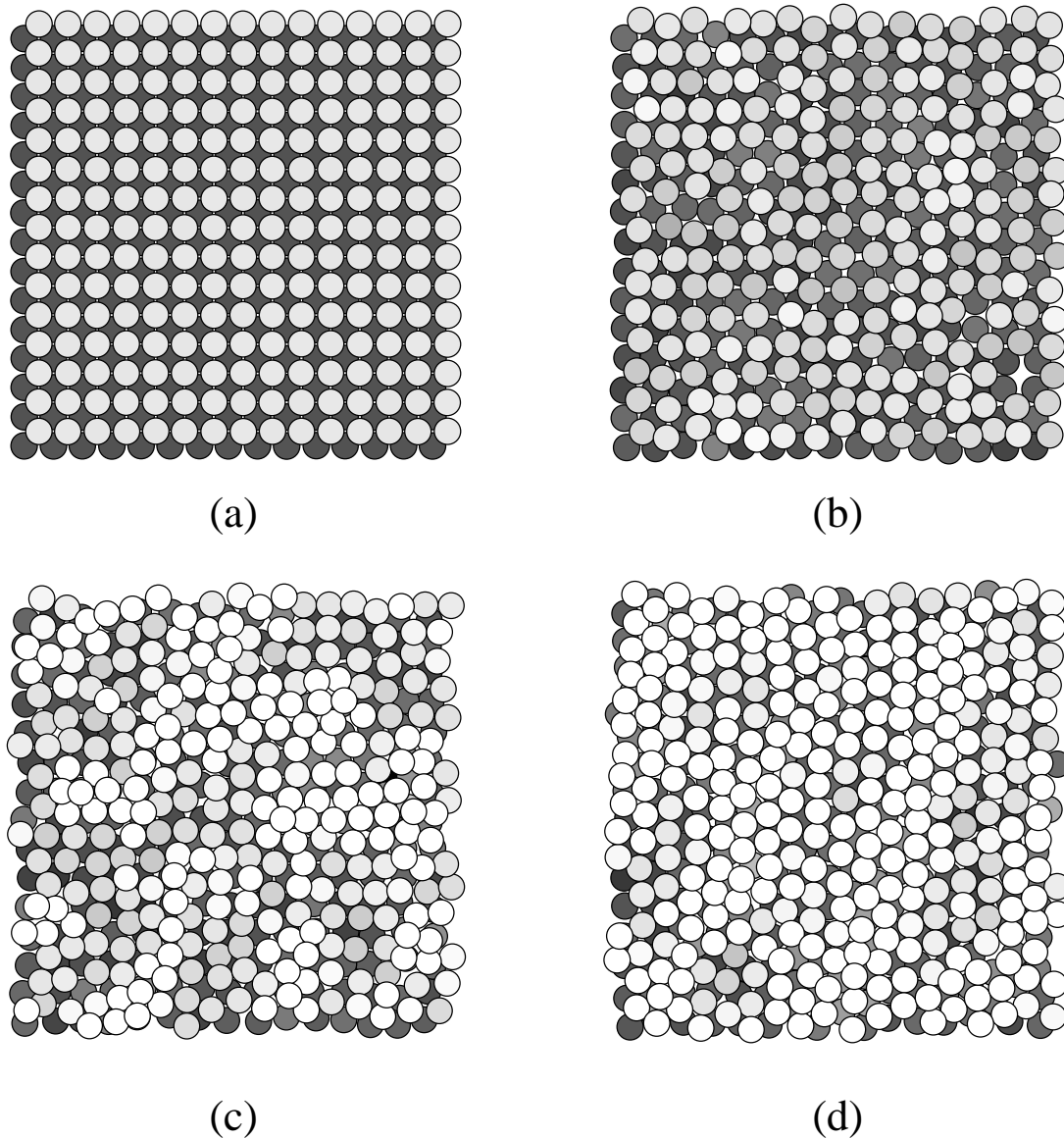


Figure 4.4: (a) The initial state of Au(100): the top layer is perfectly squared and unreconstructed; (b) first creations accepted start modifying the structure; (c) the correct lateral density is achieved; (d) quasi-hexagonal order (equilibrium state) is obtained at surface after the Monte Carlo simulation. Color of atoms reflects their height, atoms in (d) are brighter due to vertical expansion (about 20%) connected to the reconstruction of the first layer.

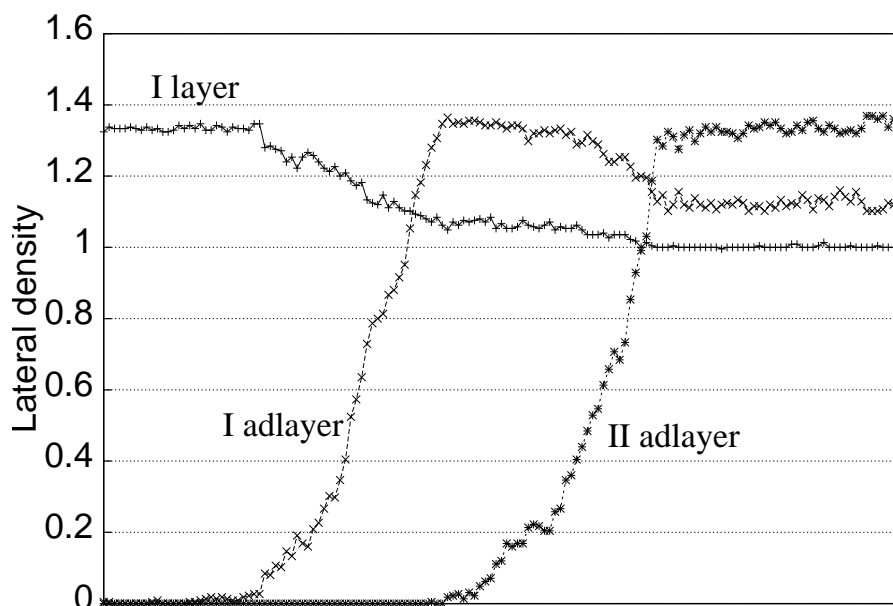


Figure 4.5: Evolution of the first layer and of two adlayers, with a slight disequilibrium towards growth(system (b)). Layer densities are normalized to bulk (100) lateral density. The I layer decreases its density and it becomes squared with defects, and eventually perfectly squared when two complete layers are adsorbed on it. The deconstruction of the underlying layer increases the growth rate of an adlayer.

### 4.5.3 High temperature GCMC simulation for metals. Equilibration problems

In this subsection we account for the state of our work concerning high temperature simulation of the (100). Our goal is to study the surface structure *above* the deconstruction temperature (see Chapter 3). To do this, we have carefully heated a large slab composed by 24 layers, three of which blocked as usual, with 900 particles per bulk layer, up to  $T = 1300\text{ K}$  ( $0.96 T_m$ ). We tuned the chemical potential, obtaining an equilibrium value of  $\mu = -4.40\text{ eV}$ , which accounts also for the entropic contribution in the Gibbs free energy. The equilibrium state we found was a disordered molten top layer with full occupancy, apparently confirming that no preroughening occurs at least in this range of temperatures.

We conclude this section with a remark concerning equilibration problems we encountered in our simulations: the point concerns the acceptance ratio for creation/destruction compared with the acceptance ratio for displacements.

If few creations/destructions are accepted with respect to displacements, the displacive moves tend to disorder the slab starting from the surface. This happens in particular if the maximum allowed displacement is too small; in this case too many displacement

moves are accepted, but the system is lead towards a zone of the phase space from which is possible (by definition of Markovian chain) but unlikely with respect to simulation time, to reach equilibrium. Therefore, since the acceptance ratio for creation/destruction is very low ( $<, 10^{-4}$ ), we should take a displacements acceptance ratio of about 0.20 instead of the traditional 0.5.



# Chapter 5

## The Ar(111) surface. Preroughening and surface melting

### 5.1 LJ systems and Grand Canonical simulations

In this chapter we report on groundwork, plus some initial successes, in implementing a grand canonical Monte Carlo (GCMC) surface simulation based on a continuous classical Hamiltonian, in particular the Lennard-Jones fcc (111) surface, chosen as a model for rare gas surface.

Rare gas solid surfaces and films have provided an important testing ground for several surface phase transitions for over two decades. Surface melting [51], roughening [52], and recently preroughening [53] have been characterized at the free solid-vapor interface. Layering transitions of thin rare gas films on smooth substrates have given rise to a wide literature [54]. The discovery of reentrant layering [55] has led to a debate over a possible explanation in terms of preroughening, as suggested by R-SOS models [56, 57], versus a melting solidification interplay as argued from simulations with a continuous potential, though canonical [58].

In Figure 5.1 we show the ellipsometric coverage isotherms for argon on graphite, from [55]. At low temperatures, the layering transitions are observed between complete layers. The layering behavior disappears at  $T = 68.8 \text{ K}$ , while it reenters at higher temperatures, with layering taking place between *half covered* layers.

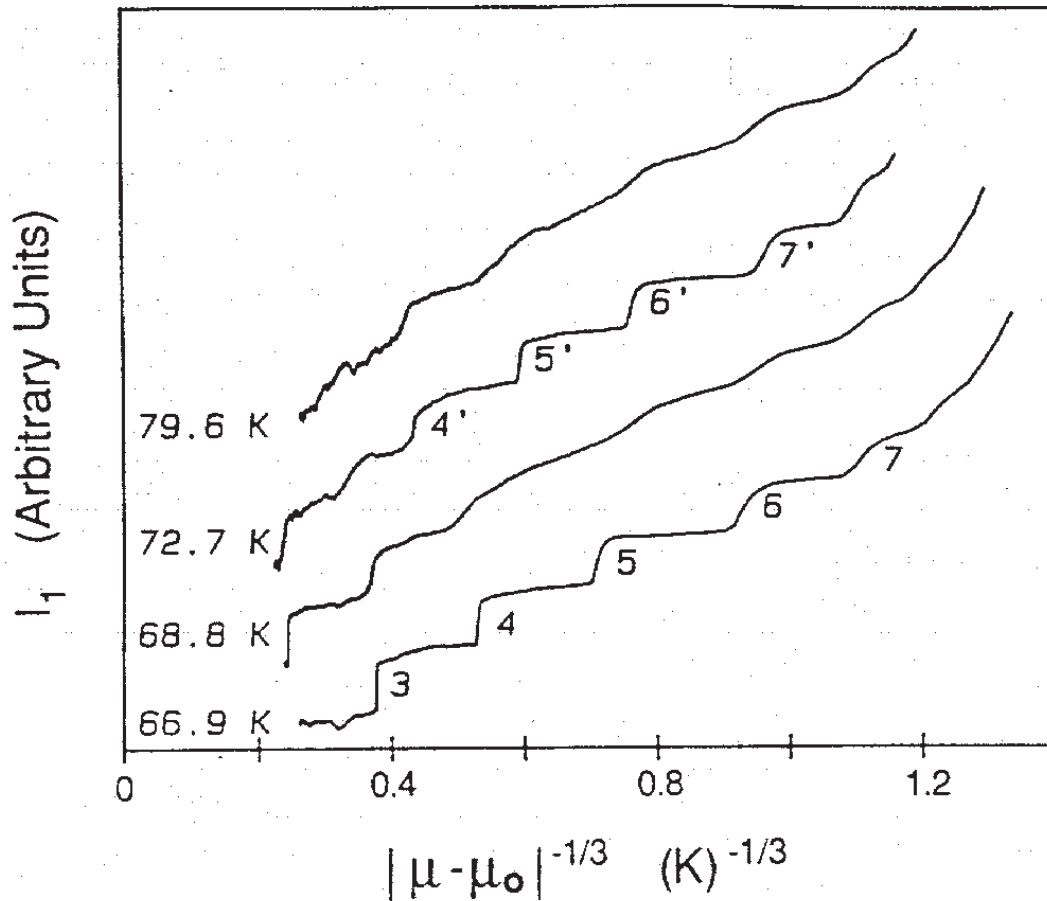


Figure 5.1: Ellipsometric coverage isotherms at four temperatures as a function of reduced vapor pressure. The reentrant layering between fractionally covered layers is evident. From [55].

In real life, the true rare gas solid surface begins to develop diffusion phenomena, which are totally absent in lattice RSOS models, above roughly  $(1/2) T_m$ . However, the lattice models allow a much more thorough statistical mechanical understanding and classification of possible surface phases. In particular, they imply the possible existence of a preroughening (PR) transition, leading to a so

called disordered flat (DOF) phase. At  $T_{\text{PR}}$ , among other things, the surface occupancy exhibits a transition from close to a full monolayer ( $T < T_{\text{PR}}$ ) to close to a half monolayer ( $T > T_{\text{PR}}$ ). This kind of transition cannot be easily simulated with a fixed particle number. In fact it has been shown elsewhere [59, 60] that a fixed particle number will lead, at and above  $T_{\text{PR}}$ , to a kind of phase separation into two neighboring DOF phases. In other words, that surface will not even remain macroscopically homogeneous. Classical off-lattice GCMC [46] has so far been successfully applied to simulate different systems such as capillary condensation in nanopores [61]. However difficulties appear when one tries to simulate a denser system [47] and the classical GCMC technique requires modifications. We have described before these modifications for a surface case.

We recall the three different types of Monte Carlo moves we have considered:

(a) small thermal displacements of individual atoms, with magnitudes  $\delta r$  adjusted with  $T$  in order to obtain an optimal acceptance rate of 50%, and random direction;

(b) large lateral displacements of surface atoms;

(c) destruction of an existing particle, or creation of a new particle. Since deep in the bulk the acceptance rates will generally be exceedingly small, we restrict attempts to within a region of thickness  $d = na$ , where  $a$  is the spacing between two consecutive bulk lattice layers, and  $n$  is typically 6 (in the LJ case). This region is centered on the outer layer of the system simulated.

Moves of type (b) were thought at first to be important for establishing surface diffusivity. It was later seen, however, that this is not really so for the LJ surface. Therefore, they were eventually omitted. Clearly, only moves of type (c) are grand canonical. Thermal moves (a) must be by far the most frequent, for equilibration. We find that a large number of such moves is necessary, in the temperature range investigated, between a grand canonical move (c) and the next. We have taken the probability of attempting a move (c) to be  $\alpha_c = \alpha_d = \alpha$  (respectively for creation and destruction), and that of attempting a move (a) to be  $\alpha_m = 1 - \alpha$ , with  $\alpha$  very small, its actual value depending on the ratio between the number of atoms in the outer layers and the total number of atoms, but roughly of the order of  $0.5 \times 10^{-3}$ .

The acceptance probability of creation and destruction,  $p_c$  and  $p_d$  have then

been finally normalized in the form [46]:

$$p_c = \min \left[ 1, \frac{V}{(N+1)\Lambda^3} \exp \left( \frac{\mu - \delta U}{k_B T} \right) \right] \quad (5.1)$$

$$p_d = \min \left[ 1, \frac{N\Lambda^3}{V} \exp \left( \frac{-\mu - \delta U}{k_B T} \right) \right] \quad (5.2)$$

where  $N$  is the number of atoms present in the creation/destruction region,  $V$  its volume,  $\Lambda = [h^2/(2\pi m k_B T)]^{1/2}$  is the thermal de Broglie wavelength, and  $\delta U = U_a - U_b$  is the difference between the total energy  $U_a$  after the trial move (creation or destruction) and the total energy  $U_b$  before it. In order to satisfy detailed balance  $N$  must be readjusted at each step of the simulation.

We simulated in this way the free fcc(111) solid-vapor interface of a rare gas, particularly Ar. The interatomic forces were described by a (12,6) Lennard-Jones potential truncated at  $2.5\sigma$ . Our system consisted of a 15-layer slab, with periodic boundary conditions along the  $x$  and  $y$  direction in the interface plane. Three bottom atomic layers were kept frozen, while 12 layers of 480 atoms each were free to evolve. The lateral box size was rigid, but readjusted at each temperature according to the thermal expansion coefficient of this potential, obtained from separate bulk simulations. We considered a grid of temperatures above  $0.46\epsilon$ , as there is very little action below (the bulk melting temperature is  $T_B \simeq 0.7\epsilon$ ). For each temperature we first found the equilibrium value of the effective chemical potential  $\mu_o(T)$ . This was done by trial and error, starting from an arbitrary value, and changing it until the particle number remained as stationary as possible. With  $\mu_o(T)$  so determined we made long equilibration runs looking for stabilization of both the total energy and the number of particles in the system. Generally half a million of Monte-Carlo (MC) steps (in the usual sense, i.e., one step attempting to move each particle on average once) were sufficient to reach reasonable equilibrium. Here we encountered our main problem, which is that this procedure is increasingly less convergent, and the resulting surface less stable, as  $T$  increases. In practice, we found it impossible to stabilize the surface against exceedingly large fluctuations above  $T = 0.56\epsilon$  ( $\simeq 0.80 T_m$ ). This constitutes an important drawback, because the interesting phase transitions of the surface are believed to lie just above this temperature, i.e., preroughening at  $0.83 T_m$  and roughening at  $0.95 T_m$  [60]. On the other hand, a further reduction in the relative creation/destruction rate  $\alpha$ ,

necessary to obtain grand-canonical equilibrium at these higher temperatures, would quickly become too costly, as would the alternative possibility of creating/destroying atoms directly in the vapor phase. Below  $0.80 T_m$ , where our equilibration worked, typically 30 to 50 uncorrelated configurations were subsequently generated from another half a million MC step is run, and finally analyzed.

## 5.2 Results

The typical  $(xy)$ -averaged density profile of the simulated grand canonical Ar-(111) surface (really solid-vapor interface, but the vapor density is tiny) is shown in Figure 5.2. Layers are clearly visible, and the outermost ones are labeled 2

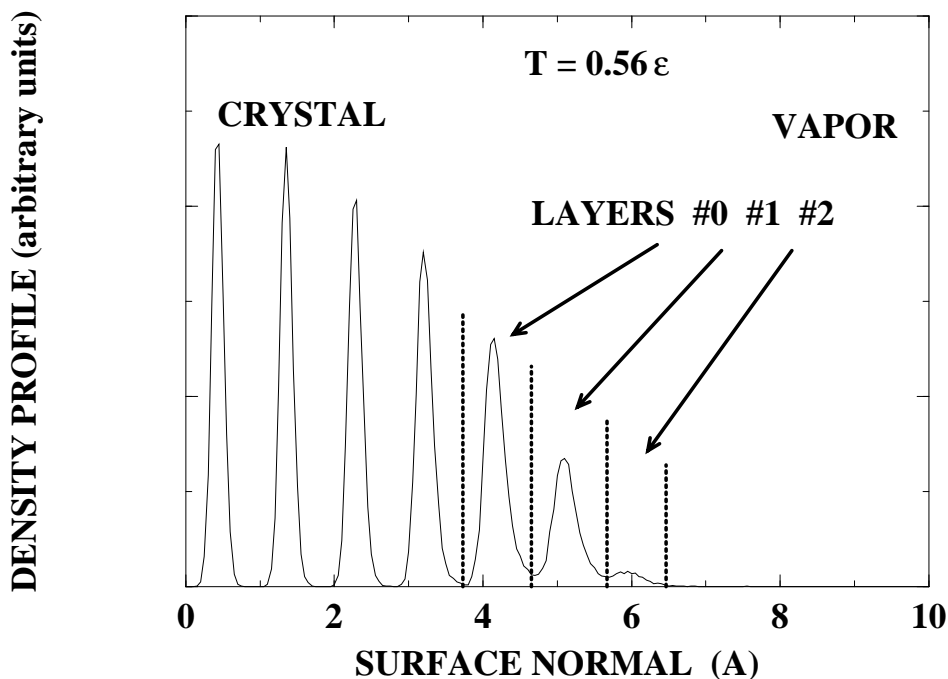


Figure 5.2:  $(xy)$ -averaged density profile of the simulated Ar fcc(111) surface in grand canonical equilibrium at  $T = 0.56\epsilon$ , or  $T = 0.8 T_m$ , plotted along the surface normal. The sub-monolayer coverage in layer 1 is the main new result, in comparison with previous canonical simulations.

(“adatom layer”), 1 (“surface layer”), and 0 (“subsurface layer”). We conventionally associate an atom with a given layer  $n$ , if it falls within the bin  $n$ , as indicated. Taking the ratio of the number of atoms in layer  $n$ ,  $N_n$  to the number  $N_B$  of atoms in a bulk layer, we obtain a conventional layer occupancy  $o_n = N_n/N_B$ . Occupancies of the three outermost layers are shown in Figure 5.3 as a function of  $T$ . At low temperatures, the layers 0 and 1 were almost

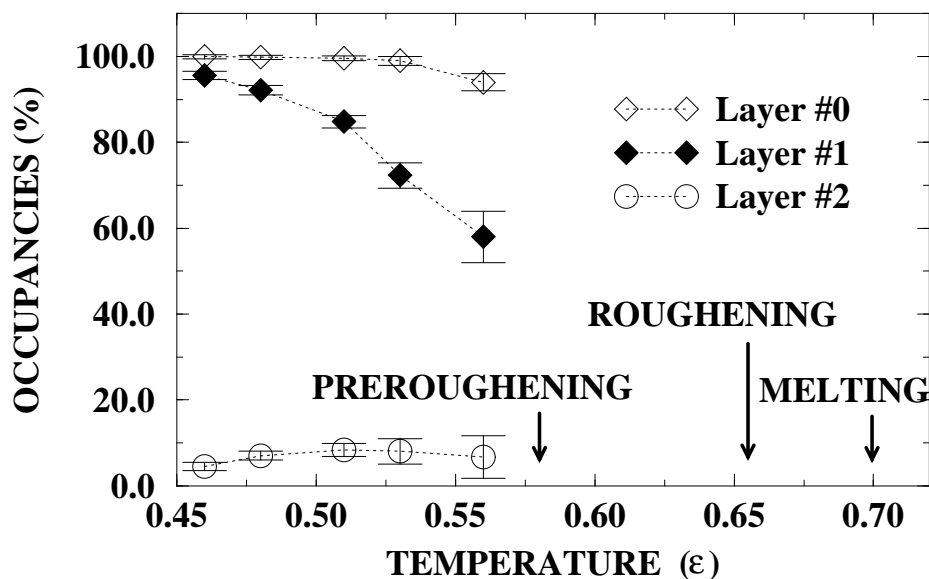


Figure 5.3: Occupancies of the three outermost layers (fraction of particles contained in the bins indicated in Fig.5.2) as a function of temperature. Note the gradually decreasing occupancy of layer 1, extrapolating to the preroughening value of  $1/2$  close to  $T = 0.58\epsilon$ .

full, with only a few percent of vacancies, with corresponding few adatoms in layer 2. As  $T$  increased, layer 1 lost atoms very rapidly, reaching an occupancy  $o_1 \simeq 55\%$  at  $T = 0.56\epsilon$ .

It is important at this point to compare the properties of this grand canonical Lennard-Jones (111) surface with those of exactly the same surface, simulated under identical physical conditions except for the canonical, particle-conserving

constraint. The results obtained in our earlier, very extensive MD simulations [60] were quite different. By starting with an integer number of layers, and at the very same  $T = 0.56\epsilon$ , for example, we had obtained canonically  $o_2 \simeq 100\%$ ,  $o_1 \simeq 90\%$ ,  $o_0 \simeq 10\%$ , against the present grand canonical values  $o_2 \simeq 94\%$ ,  $o_1 \simeq 55\%$ ,  $o_0 \simeq 8\%$ . Grand canonically, the “total surface population” ( $o_2 + o_1 + o_0 - 1$ ) appears to change continuously with temperature, going from nearly 100% at  $0.65 T_m$  down to 57% at  $0.8 T_m$ . This kind of gradual change was not predicted by the less realistic solid-on-solid models [59, 62].

Extrapolating, these data strongly suggests that at  $T \simeq 0.58\epsilon$  the surface spontaneously tends to half occupancy, with about 8% adatoms and 6% sub-surface vacancies. This temperature is in excellent agreement with the experimentally observed temperature for the onset of reentrant layering,  $T = 69 \text{ K} \simeq 0.83 T_m$  [55]. The coincidence with the preroughening temperature obtained from canonical simulations is perfect. The half occupancy also agrees with theoretical predictions and with solid-on-solid simulations of the disordered flat (DOF) state, realized at and above preroughening [62, 53]. Therefore, the present grand canonical realistic simulation data strongly confirm the occurrence of preroughening and of a DOF phase on the free surface of Ar(111) at  $T_{\text{PR}} = 0.83 T_m$ .

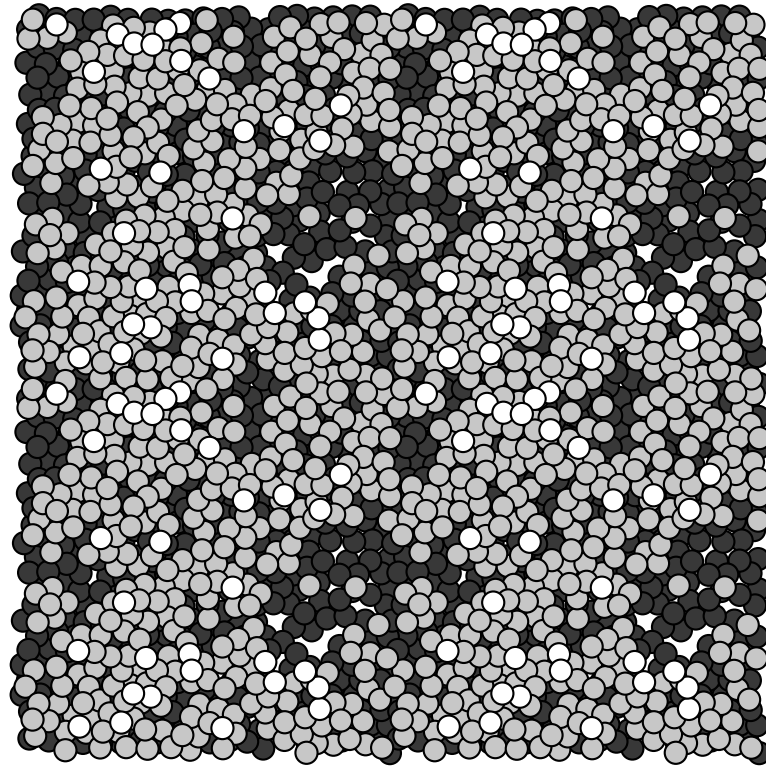


Figure 5.4: Top view (snapshot) of the three outer layers of simulated grand canonical Ar(111) at  $0.8 T_m$ . This surface is nearly “disordered flat” (DOF). Atoms in layers 0, 1 and 2, identified through their  $z$ -coordinate as in Figure 5.2, are respectively black, grey and white. For convenience, four adjacent cells are shown. The nearly half occupancy of the surface layer (layer 1) is realized through large islands and large craters.

Figure 5.4 presents a top snapshot of the grand canonical surface at  $T = 0.56\epsilon$ , the closest we can get to  $T_{\text{PR}}$ . This is, we believe, the first available illustration of what a rare gas surface really looks like at preroughening. The main features to be noted are the large islands and craters in the first (gray) layer. We did not try yet to examine the height-height correlations of this surface, which would have been very interesting, particularly to check whether they are large as expected by our predicted divergence at  $T_{\text{PR}}$ [59]. In order to do that properly, we would need finite-size scaling, which is computationally too demanding.

In conclusion, we have obtained preliminary results on the microscopic na-

ture of a rare gas solid-vapor interface, as obtained by means of a novel grand canonical Monte Carlo simulation. In spite of difficulties encountered with stabilizing the surface at higher temperatures, we have succeeded in describing what appears to be a well equilibrated surface in an interesting temperature range. We have obtained a clear indication that preroughening is indeed taking place under conditions very close to those where reentrant layering was observed on Ar(111), and where DOF phase separation was found by canonical MD [60].

### 5.3 Growth on a substrate

In the previous section we described the simulation of a rare gas free surface in the grand canonical ensemble and found indications that PR does exist in the fully continuous case as well. However a full description of the transition to the DOF phase had not been possible due to the difficulty of stabilization of the free solid-vapor interface (i.e to find the equilibrium value of the chemical potential) at least for higher temperatures.

In this section we present results of a grand-canonical Monte Carlo (GCMC) simulation for adsorption of a rare gas thin film on a flat attractive substrate. In this case, the presence of the substrate allows a much easier stabilization of the system. We have obtained realistic adsorption isotherms, which we compare directly with the experimental ones. Monitoring microscopical quantities such as the layer occupancies and the pair correlation functions, we confirm that the reentrant layering transition is indeed associated with PR.

In the case of adsorption simulation the encountered difficulties in the grand canonical simulations can be due to a larger number of particle destructions or creations which do not give the system the "Monte Carlo time" necessary to equilibrate through small displacements. This is especially true for a high number of adsorbed layer where the majority of atoms situated in the deepest layers have a small probability to be destroyed. In order to leave to the system the possibility to equilibrate after each creation or destruction we have increased the probability of attempted moves,  $\alpha^m$ , compared to the probability of attempted creations and destructions, respectively  $\alpha^c$  and  $\alpha^d$ . In standard GCMC simulations the fastest convergence to the Markov chain was found by Norman and

Filipov [50] for  $\alpha^m = \alpha^c = \alpha^d = 1/3$ , whereas in our simulations we have taken the general form  $\alpha^c = \alpha^d = \alpha$  and  $\alpha^m = 1 - \alpha$  where  $\alpha$  has a small value depending on the ratio of the total number of atoms versus the number of atoms in the outer layers. It is important to note that the problem just described is specific of the system studied: we currently encountered the opposite problem (rare creation/destruction events) in the simulation of reconstruction on noble metals, as pointed out in the previous chapter. The creation and destruction were also only attempted in a fixed region of our simulation box centered on the out-most adsorbed layer and approximately four layers wide. The probability of creation and destruction acceptance have been finally written in order to verify the detailed balance condition associated with the above described modifications.

We have simulated adsorption of atoms described by the (12,6) Lennard-Jones potential truncated at  $2.5\sigma$ . The substrate was taken to be flat, unstructured, occupying the  $z < 0$  region and with periodic boundary conditions taken along the  $x$  and  $y$  directions. Interactions between the substrate and atoms were also supposed of the Lennard-Jones form, giving rise to a laterally invariant potential (3,9). The attractive part of the substrate potential was enhanced with respect to the usual Ar/Graphite potentials, in order to avoid stabilization problems encountered in a previous simulation of a free solid-vapor interface, described in the preceding section [5].

The size of the simulation box was of  $23 \times 23 \times 20 \text{ \AA}$  in the  $x$ ,  $y$  and  $z$  direction respectively, so that a full layer was composed of approximately  $N_l = 500$  atoms at a temperature of  $0.61\epsilon$ . In this letter we will focus on two isotherms obtained below and above the PR temperature,  $T_{PR}$ . From both R-SOS models [59], experimental results [55] and canonical simulation [60] it was found to be  $T_{PR} \simeq 0.56\epsilon$ , hence we present adsorption isotherms obtained at  $0.53\epsilon$  and  $0.61\epsilon$ . For each temperature the procedure adopted was to increase the chemical potential  $\mu$  (i.e. to increase the pressure of the fictitious perfect gas in contact with our system) of the system by intervals of  $\simeq 0.02\epsilon$  and to wait for stabilization of both the total energy and the number of particles in the system. Generally half a million of Monte-Carlo (MC) steps (as usually defined respectively to the number of particles in the system) were sufficient to reach equilibrium. Then 30 to 50 uncorrelated configurations were generated from another half a million MC steps run and subsequently analyzed.

The first quantity analyzed is the same as that accessible to experiments : the adsorption isotherm where the number of particles in the system (expressed in number of equivalent full layers) is recorded as a function of  $(\mu_0 - \mu)^{-1/3}$ ,  $\mu_0$  being the equilibrium value of the chemical potential for the bulk. In Figure 5.5 we plot the two simulated isotherms for the two temperatures of  $0.53\epsilon$  and  $0.61\epsilon$ . At the lower temperature we observed marked layering transitions between consecutive integer values of layers. For all layers we observed two stages of growth; first, adatoms in the upper layer gradually reach an occupancy of  $\simeq 15 - 20\%$ , while in the same time vacancies in the second layer are filled; in a second time, one can observe an abrupt jump to a state where the first layer is almost completely full ( $\simeq 15 - 20\%$  of vacancies and negligible presence of adatoms).

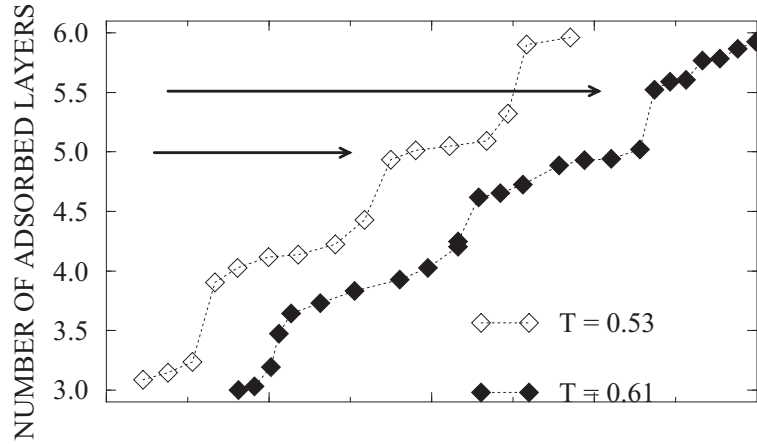


Figure 5.5: The two isotherms for the two temperatures of  $0.53\epsilon$  and  $0.61\epsilon$ . At  $0.53\epsilon$  layering transition between consecutive integer values of layers are observed. At  $0.61\epsilon$  a vertical shift in layering and abrupt jumps towards half integer occupancies appear.

We have verified that isotherms between these two temperatures become broader and broader and finally lose the layering behavior. At these intermediate temperatures the system is very difficult to equilibrate; for this reason we cannot show here clean plots of the adsorption isotherms.

The re-entrance of the layering is effectively observed at a temperature known to be higher than  $T_{PR}$ . Even if layering is still present, there are essentially two important qualitative differences with the low temperature isotherm : the isotherm is shifted in the vertical direction and is much broader. The system seems to switch abruptly to a half-integer layer number, progress continuously

its absorption and finally jump to the next half integer layer value. We plot in Figure 5.6 the  $0.61\epsilon$  isotherm up to eight adsorbed layers, which was the maximum value obtained before encountering stabilization problems. In the inset the amplitude of the continuous adsorption progression  $dn(i)$  for each layer  $i$  is plotted.

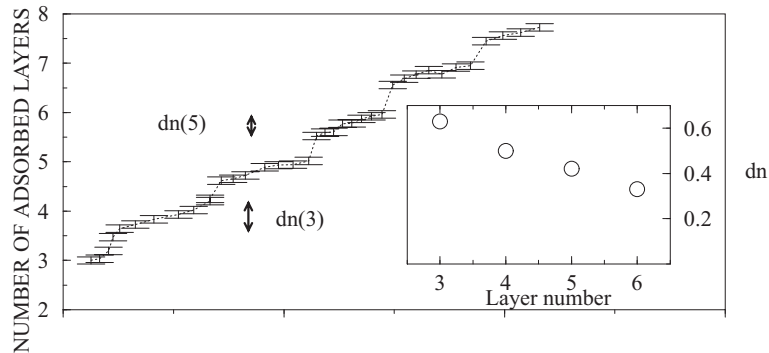


Figure 5.6: The  $0.61\epsilon$  isotherm up to eight adsorbed layers. In the inset the amplitude of the continuous adsorption progression  $dn(i)$  for each layer  $i$  is plotted.

As the solid-vapor interface is far away from the substrate, the value of  $dn$  decreases. This clearly shows that the continuous progression is directly related to the substrate-adatoms interactions. Such a behavior is not clearly seen in experiments since this interaction for the real Ar/Graphite system is weaker. In spite of it we see that, in the limit of large numbers of adsorbed layers, our isotherm is qualitatively in good agreement with the experimental ones. In Figure 5.7 we plot the occupancies of the different layers versus the chemical potential of the system and for the temperature of  $0.61\epsilon$ . The jumps to the half occupied layers is also observable here. We can remark that the occupancy of the first layer just after the discontinuous adsorption tends clearly to 50 % for a large number of adsorbed layers. The occupancies of the adatoms layer is less dependent on the adsorbed layer number and is roughly of 10 %, while the second layer has an occupancy of about 80 %. This characterization of a realistic DOF phase is now much more detailed from results obtained from lattice models [57].

One major source of difference is certainly due to the onset of surface first-layer melting above  $T_{PR}$ , a phenomenon described earlier in Canonical MD [58], but not previously related to PR. We have studied in detail the positional order of different layers above and under this temperature. For  $T < T_{PR}$  all the

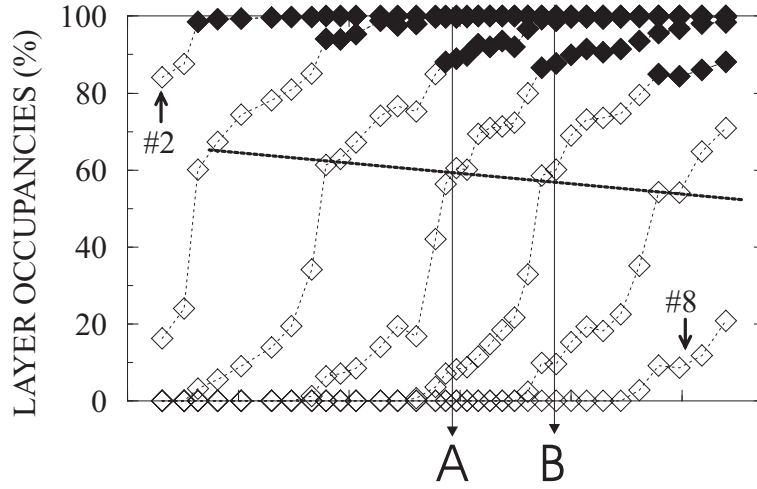


Figure 5.7: The occupancies of the different layers versus the chemical potential of the system and for the temperature of  $0.61\epsilon$

layers present a crystalline order (except the upper adatoms layer). The situation is richer for  $T > T_{PR}$ .

In Figure 5.7 filled diamonds mark ordered layers, whereas empty diamonds mark fluid-like layers. We start the description from a state (indicated with **A** in the Figure) where the upper layer has few adatoms, the second layer (with disordered structure) has an occupancy of approximately 50% and the third layer is close to perfect full solid layer. We observed a continuous adsorption on both the first and the second layer. When the upper layer of adatoms reaches an occupancy of  $\simeq 20\%$  a sudden jump occurs to reach the 50% occupancy. At the same time, the second layer solidifies. This is visible through the jump of approximately 10% in the occupancy which roughly corresponds to the density difference between solid and liquid. At this point the system is in a state (indicated with **B** in the Figure) identical to our starting state, except that the upper layer is now the second, the second the third, and so on.

The existence of this double regime (i.e. abrupt jump to half integer values and continuous growth) observed for the first adsorbed layers can be understood in terms of a substrate influenced PR transition. We write the grand potential,  $\Omega$ , of the system using a phenomenological theory often used, for example, in the case of surface melting. This potential is essentially composed of two parts:

$$\Omega = \Omega_C(N, \mu, T, \gamma \dots) + \Omega_{SI}(N, T)$$

$\Omega_C$  is the classical part of the grand potential, it is dependent on number of par-

ticles, temperature, chemical potential and on the different interfacial tensions in the system. There are in this potential two opposite effective driving force applied on the solid vapor interface. Since  $\mu > \mu_0$  the adsorption of the solid phase on the substrate is energetically unfavorable, the solid-vapor interface is attracted by the substrate. On the other hand, since the substrate is perfectly wet by the solid phase, the spreading coefficient,  $S = \gamma_{sv} - \gamma_{sc} - \gamma_{cv}$  where the subscripts  $s$ ,  $c$  and  $v$  denote respectively the substrate, the crystal and the vapor, is positive. This gives rise to an effective repulsion between the substrate-crystal and the crystal-vapor interfaces. At a fixed temperature and chemical potential  $\Omega_C$  has a local minimum at a certain value of the number of particles  $N_0$ , when  $\mu$  is increased and approaches  $\mu_0$ ,  $N_0$  diverges to infinity. In order to simplify, we assume a parabolic form :  $\Omega_C = \alpha(N - N_0)^2$ .  $\alpha$  is a parameter related to the influence of the substrate, larger values correspond to a low number of adsorbed layers (i.e. a small value of the equilibrium value  $N_0$ ) When the value of  $\alpha$  tends to zero, the minimum is still present but less marked. We approach the asymptotic problem to equilibrate a free crystal-vapor interface.  $\Omega_{SI}$  is the part of the grand potential related to the step interactions at the crystal-vapor interface. For temperatures above  $T_{PR}$  the theory predicts a half occupied first layer,  $\Omega_{SI}$  will then have local minima at half integer values of  $N/N_l$ .

We qualitatively propose the form :  $\Omega_{SI} = \cos(\frac{2\pi}{N_l}N)$ . We represent in Figure 5.8(a) a sketch of the evolution of the grand potential for a large  $\alpha$  and different values of  $N_0$  taken between two successive half occupied layers. With this simple description we can qualitatively explain two features of this system observed in our simulations. The continuous adsorption is justified by the horizontal shift of the local minimum; the abrupt condensation is justified by the disappearance of this minimum followed by the jump to the next local minimum.

In Figure 5.8(b) we can see that a smaller value of  $\alpha$  reduces the amplitude of the continuous progression. Also note that in this case there is no disappearance of the local minima but the system jumps from the meta-stable to the stable state. This simple model shows that the reentrant layering transition is associated with PR.

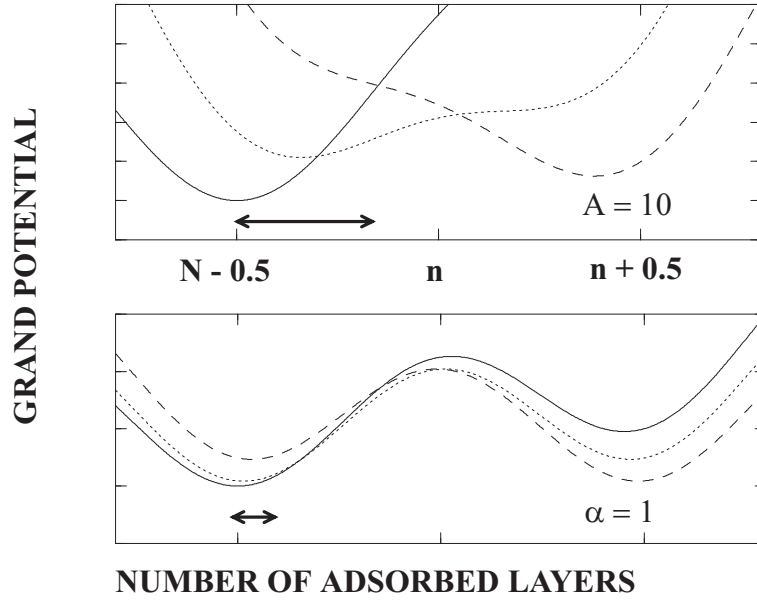


Figure 5.8: (a): a sketch of the evolution of the grand potential for a large  $\alpha$  and different values of  $N_0$  taken between two successive half occupied layers. The continuous adsorption followed by the abrupt condensation as observed in our simulation is justified respectively by the horizontal shift of the local minimum and by its disappearance followed by the jump to the next local minimum; (b): a smaller value of  $\alpha$  reduces the amplitude of the continuous progression.

To test the alternative explanation in terms of a melting solidification interplay but no PR, as proposed by Phillips *et al.* [58] we plot in Figure 5.9 the pair correlation functions of the third and fourth layers for two coverages of  $4.92N_l$  and  $5.52N_l$  respectively just before and after the discontinuous adsorption. The third layer is a two dimensional crystal which is not modified by the increase of the coverage. On the other hand, we can see that the fourth layer apparently undergoes a solidification. This is confirmed by the increasing of its occupancy which is roughly equal to density difference between the solid and the liquid. The solidification process is present and effectively associated with the layering transition. Nevertheless, this cannot explain why the fifth layer should reach an occupancy of 56 %, as it indeed does, once grand canonical freedom is allowed.

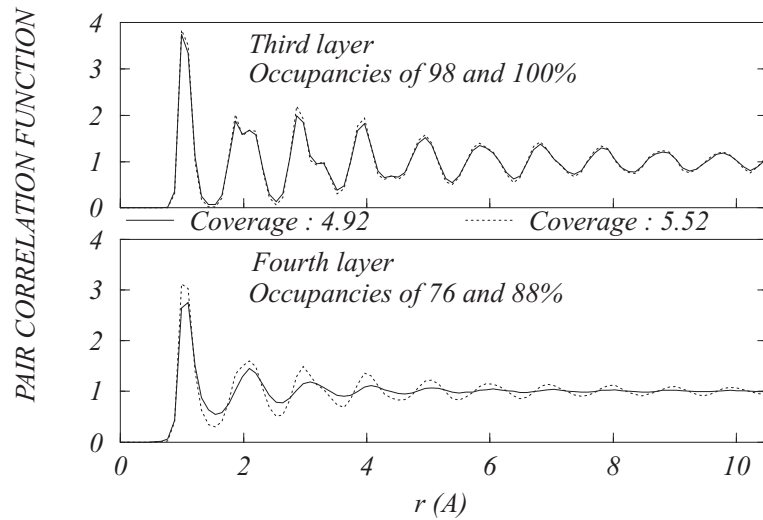


Figure 5.9: The pair correlation functions of the third and fourth layers for two coverages of  $4.92N_l$  and  $5.52N_l$  respectively just before and after the discontinuous adsorption, always at  $T > T_{PR}$ .

To summarize, we can explain the experimental evidence of the reentrant layering occurring in the adsorption of rare gas on a solid substrate. Layer by layer occupancies, pair correlation functions and direct insight on the surface density and mobility, that are not directly accessible from experiments, confirm the interpretation of the reentrant layering transition in terms of preroughening. Furthermore, we show that there is a coincidence of the onset of surface first-layer melting with the PR transition. These two surface phenomena, apparently very different, appear here to be in intimate connection. However, the role of surface melting in determining the existence of a PR transition below the roughening temperature is still unclear. Further connections between surface melting and preroughening are therefore under present study.

# Chapter 6

## Adsorption-induced deconstruction

### 6.1 Experimental framework

The early motivation for this line of research was provided by surface heteroadsorption work in D.A. King's group in Cambridge. When adsorbing molecules such as  $CO$ ,  $D_2$  and  $O_2$  onto a fully hex-reconstructed Pt(100) surface, formation of regular islands was observed, but the island growth rate was seen to be initially very low. Specifically King *et al.* found that the molecular island growth rate increases roughly like the fourth power of molecular coverage  $\theta$ :

$$R \simeq K\theta^4. \quad (6.1)$$

The explanation offered for this phenomenon is that while the hex-reconstructed surface is unreactive, and will not give rise to dense molecular islands, the opposite is true for the *deconstructed*, square (100) surface. The latter must nucleate, and this requires no less than 4 ad-molecules.

The highly non linear growth rate is shown in Figure 6.1, taken from [2] (referring to adsorption of CO on Pt(100)) and in Figure 6.2, taken from [63]

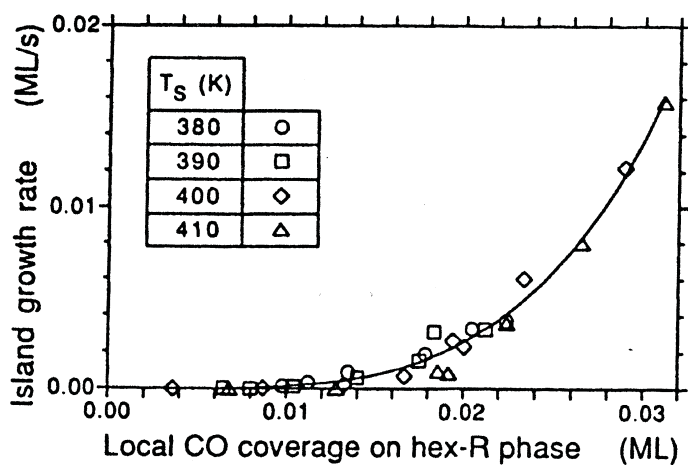


Figure 6.1: The (1x1)-CO island growth rate as a function of local CO coverage  $\theta$  on the hex-R phase at different temperatures. The line depicts a rate proportional to  $\theta^4$ . From [2].

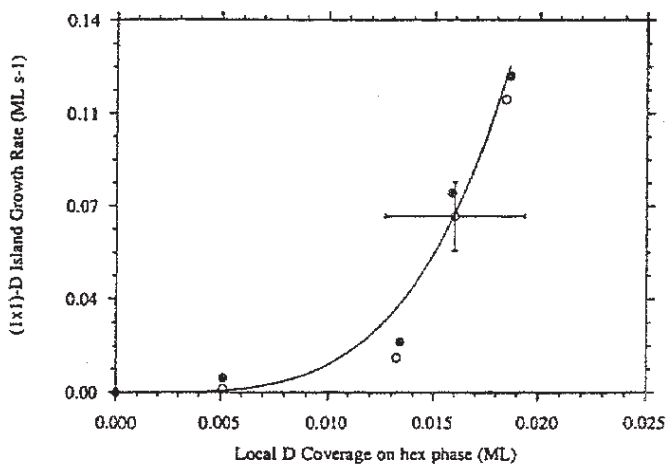


Figure 6.2: The (1x1)-D island growth rate as a function of the local D coverage on the hexagonally reconstructed phase at surface temperatures between 160 and 230 K, for total D coverages of 0.04 ML (solid circles) and 0.06 ML (open circles). The line represents an island growth rate proportional to  $\theta_D^{hex}$  raised to the power 4.0 (6.1). Figure from [63].

(referring to adsorption of H on Pt(100)). A pictorial explanation of the phenomenon is also reproduced in Figure 6.3, taken from [64].

We further observe that, since the CO coverage is  $1/2$ , King's exponent of about 4 implies that about 8 Pt atoms must switch from hex to square for the adsorption process to continue. Hence King's law is most likely telling us a property of the clean surface, not very dependent on the adsorbed species.

The next observation is that very much the same deconstruction must take place with homoepitaxy. Hence we expect that upon deposition of Pt on Pt(100), or on Au(100), particularly at high temperatures when equilibrium can be established, there should be a minimum critical island size, of order 8 or so atoms, related to deconstruction of the substrate. We have set up simulations to address this possibility, and understand its microscopic details.

In our work, we have focused the attention on the triangular-square deconstruction transition which takes place at the (100) surface of a noble metal, such as platinum and gold. This reconstruction is now deeply studied, but the mechanisms of its microscopic creation or removal, especially at high temperatures, are not clear. The deconstruction transition, which is observed experimentally at  $T = 1173K$ , is still not completely understood. In the earlier part of this thesis, we have shown that the orientational hexagonal order, typical of a low temperature triangular phase, can disappear through mutual disordering of locally reconstructed domains. However, there is also another framework where the deconstruction can be observed. Since the reconstruction is a way for the surface to increase coordination, as soon as an initially covered part of the second layer remains exposed at the interface, reconstruction in this zone should appear. This was indeed seen to be the case in Chapter 3. In the same way, if an island grows on the surface, the top of the island should be reconstructed and the surface under the island should revert to a square lattice. This last prediction is confirmed by experiments made on Pt (100) [65], through homoepitaxial deposition. As seen in Figure 6.4, which is a series of STM topographs (the highest resolution is  $90 \times 90 \text{ \AA}^2$ ) the islands are reconstructed and the surface under the island is squared: this conclusion can be drawn by observing the rows over the island in (c) which reveal the typical (1x5) pattern of the hexagonal-on-square reconstruction.

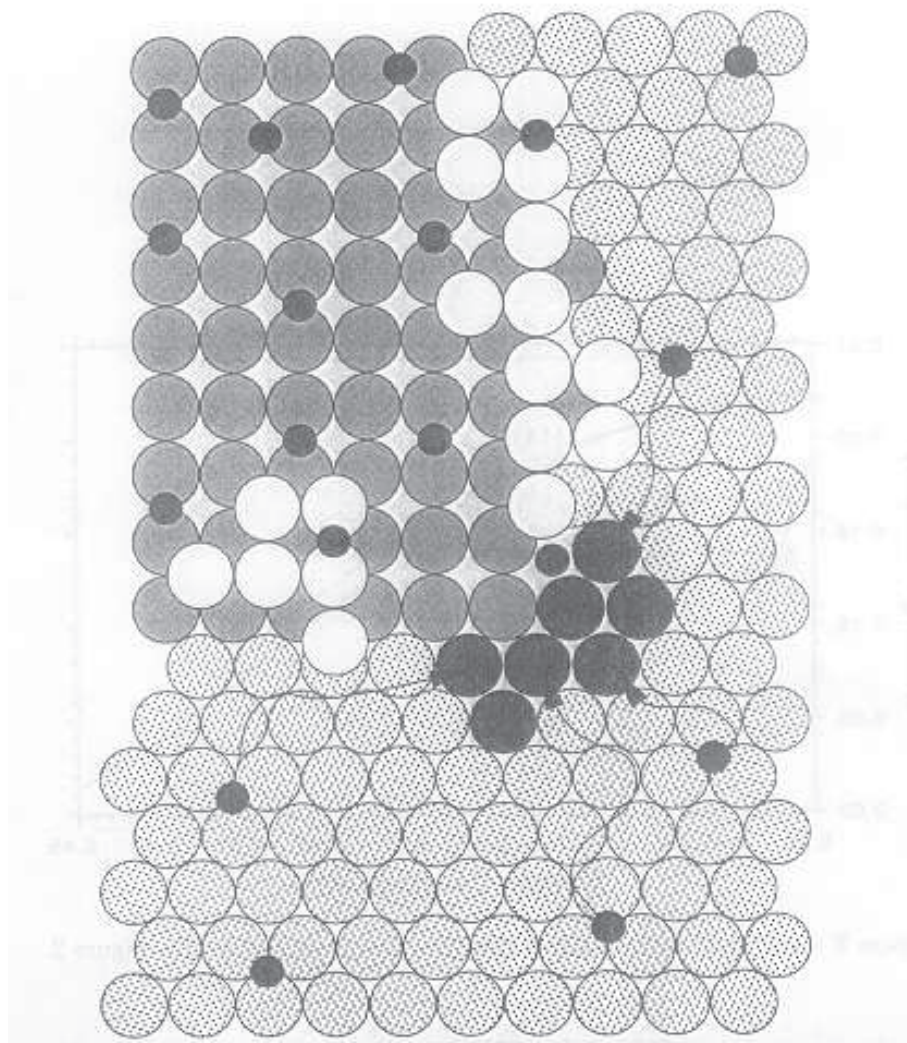


Figure 6.3: A schematic illustration of the  $(1 \times 5) \rightarrow (1 \times 1)$  phase transformation. Dotted circles represent surface iridium atoms in the  $(1 \times 5)$  phase; grey circles represent Ir atoms in growing  $(1 \times 1)$  island; small black circles represent chemisorbed oxygen atoms, in the relative size corresponding to their covalent radius; white circles represent Ir atoms forced up as a result of the completed phase transformation; large black circles represent the next 7 Ir atoms to be converted to  $(1 \times 1)$  when 4 oxygen atoms from the reconstructed phase locally fluctuate towards the domain boundary. From [64].

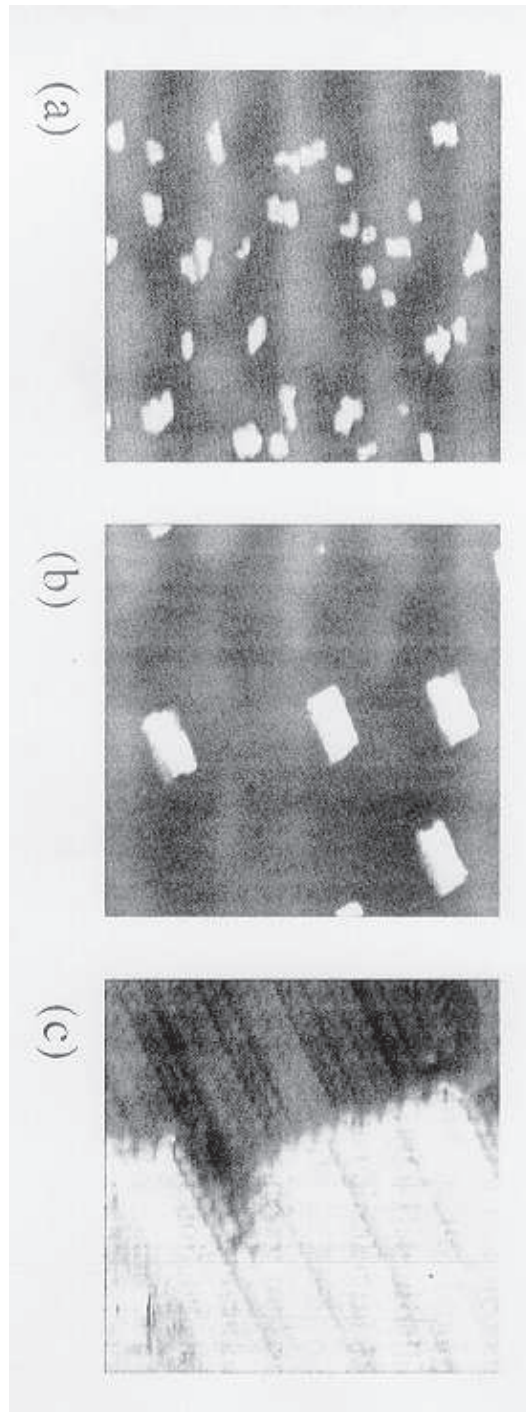


Figure 6.4: STM topographs showing monoatomically high Pt islands, from [65]. (a) Irregular but compact islands obtained at low temperature ( $T = 318\text{ K}$ ). The islands are reconstructed. ( $930 \times 960\text{ \AA}^2$ ). (b) Rectangular islands obtained by deposition at  $T = 389\text{ K}$ . The islands are oriented with their long edge parallel to the direction of the reconstruction channels. The reconstruction of the islands is revealed in (c), where the edge of an island is depicted with atomic resolution ( $90 \times 90\text{ \AA}^2$ ).

## 6.2 MD simulations

We have set up simple simulations in order to clarify the microscopic mechanisms underlying the transformation from reconstructed to deconstructed upon adsorption (and vice versa upon desorption). For the simulation, we exploit the fact that formation of islands and craters is possible not only upon homoepitaxial deposition, but also when strong density fluctuations take place at the surface: indeed, canonical ensemble MD reveals in this case an unexpected advantage: while strong density changes are requested by the surface, neither extra atoms insertion nor destruction is available, due to the particle number conservation. The only source/sink of extra particles are steps, requiring formation of islands, or formation of holes. Atoms in excess cannot desorb (metals vapor pressure is very low at any temperature lower than  $T_m$ ) and must attach to steps, or else form islands on the surface.

We have simulated an Au(100) surface, with 12 layers, whose top layer was hexagonally reconstructed, and 625 atoms per bulk layer. The surface lateral density at  $T = 0$  (which will be referred in the following to the bulk one), was chosen between 1.2 (perfect hexagonal overlayer) and 1.29. As described in Chapter 3, this surface *increases* its lateral density when the temperature increases [27, 4]. We have therefore used temperature as a ‘driving force’ for obtaining density changes at the surface. First, we have investigated the formation of ‘holes’ by increasing temperature from  $T = 0 K$  to  $T = 950 K$ . At this temperature, surface atom mobility is sufficiently high. The main results found in this study are the following:

- The formation of craters is an example of homogeneous nucleation with a critical size  $N_H$  of about 8 – 10 atoms. Figure 6.5 shows this behaviour; the size (in atoms) of a crater is plotted versus the simulation time. At a size of about 8, a jump occurs and the growth continues in a linear way, up to a saturation value.
- The craters with  $N < N_H$  present sometimes the onset of a reconstruction, but are mainly unreconstructed with the boundary of the hole avoiding the mutual sliding of the rows in the crater bottom.
- The mechanism for further growth of the craters with  $N > N_H$  is the

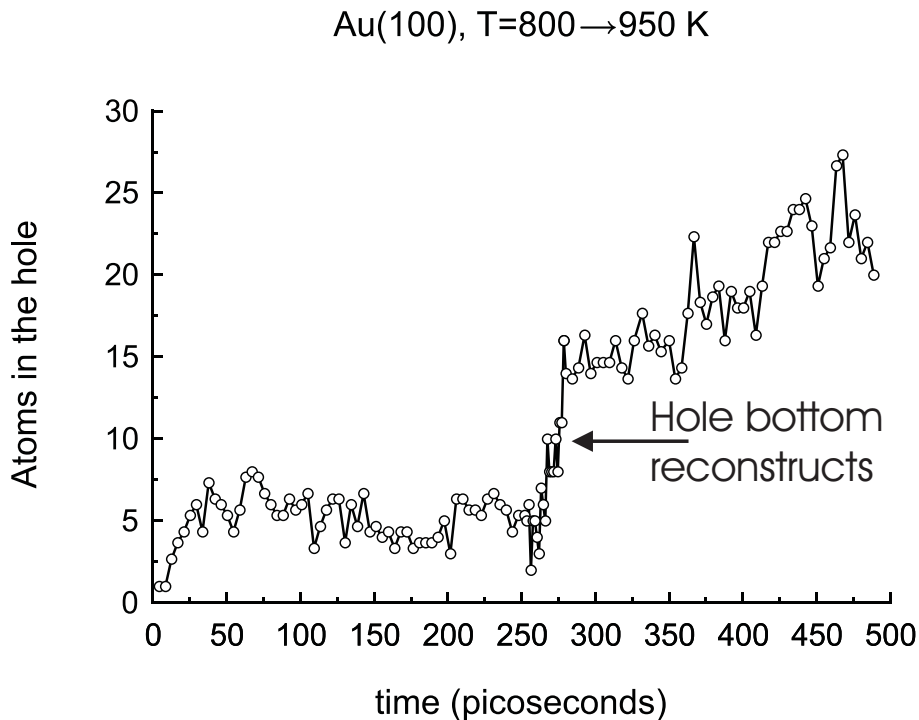


Figure 6.5: The time evolution of a crater size. Please note the jump at a critical value for the size.

following: atoms in the hole, initially arranged in a square lattice, are undercoordinated; the boundary of the crater (a ‘closed step’) provides extra atoms, increasing the dimension of the hole. This process does not appear to be unstable (*i.e.*, the growth saturates to a maximum value).

### 6.2.1 Microscopic details of crater formation

A set of snapshots of the simulation at  $T = 950$  K is shown in Figure 6.6. In these images the tendency of the surface to increase its density appears almost immediately through the formation of small holes; these craters appear unreconstructed, and the square packing appears to be forced by the boundaries of the hole. Moreover, these small holes close again and other craters appear after some picoseconds. As soon as a particular crater exceeds the size (*i.e.* number of atoms) of about 10, it becomes stable and its growth proceeds until the correct lateral density for that temperature is reached.

The mechanism of the reconstruction in the bottom of the crater is well The mechanism of the reconstruction in the bottom of the crater is well described

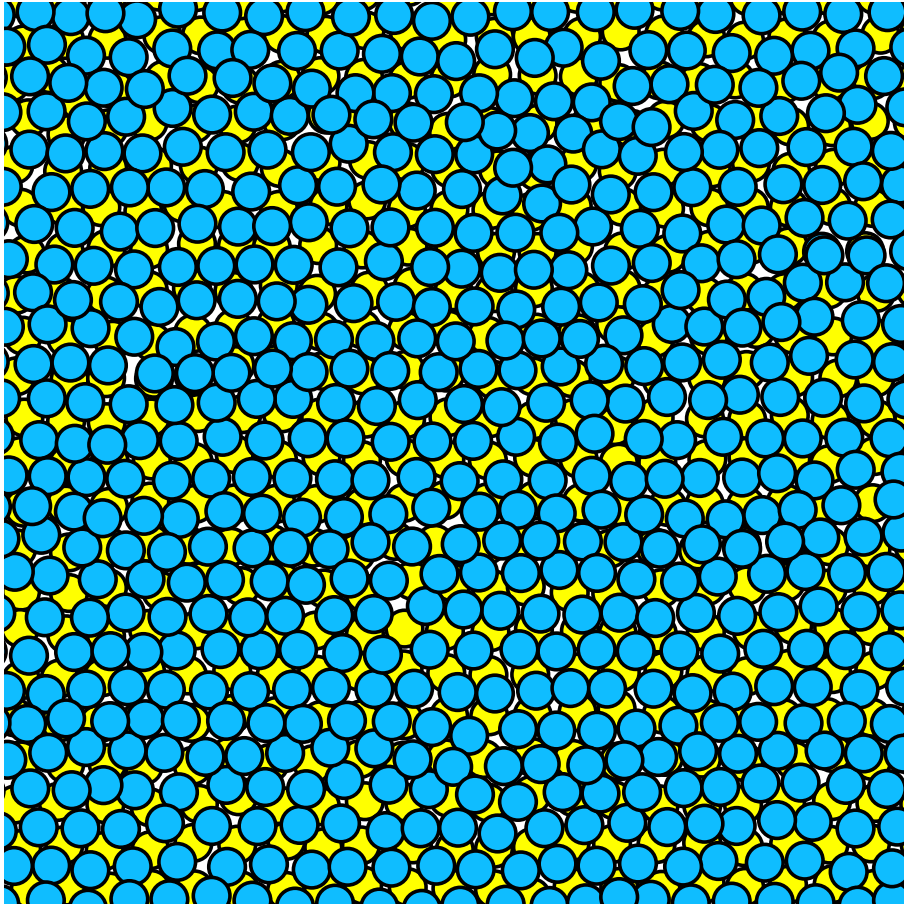


Figure 6.6: Snapshots of the simulation. The temperature has just been raised, step-like, from  $T = 800\text{ K}$  to  $T = 950\text{ K}$ . This is a detail of the initially perfectly uniform layer ( $t = 0$ ).

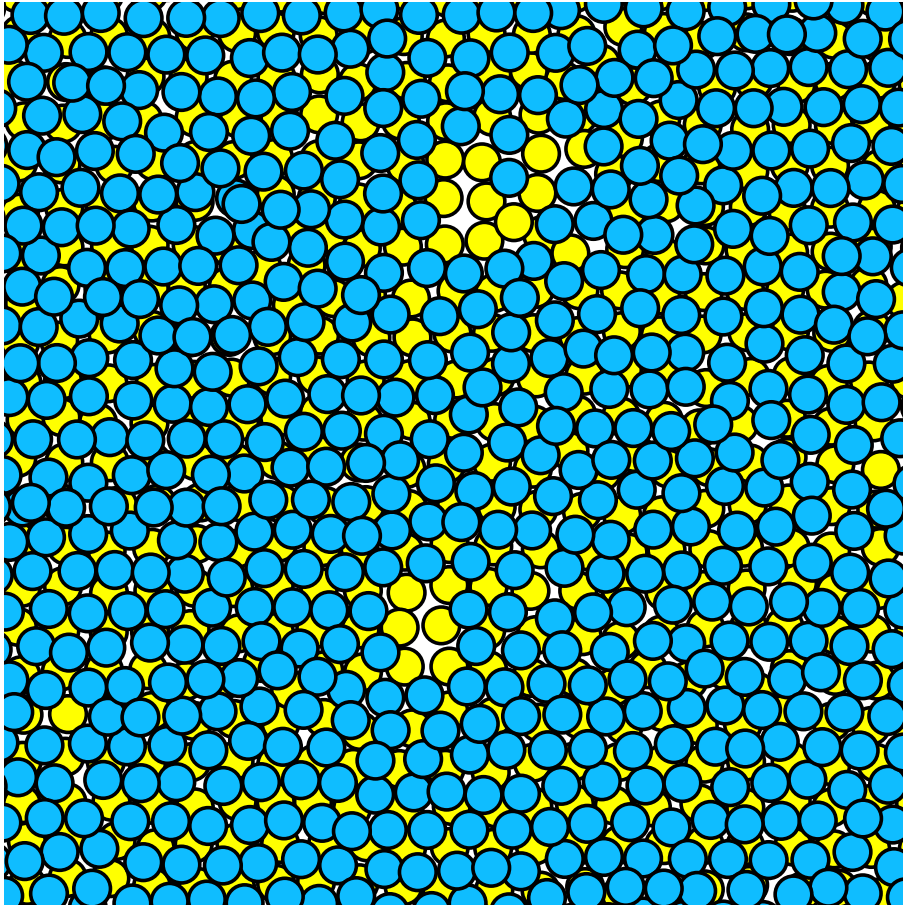


Figure 6.7: At  $t = 210ps$ , two small, unreconstructed craters remain uncovered (brighter atoms are lower).

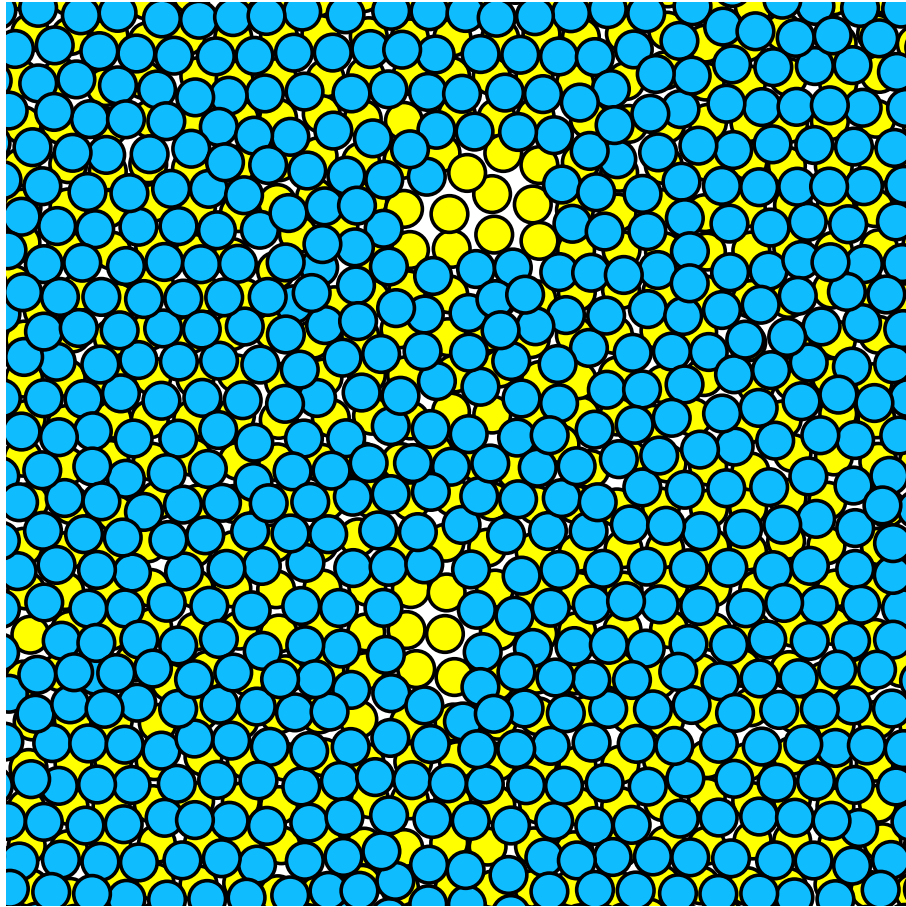


Figure 6.8: At  $t = 228.2 \text{ ps}$ , no significant variation in the size of the craters is observed ( $T = 950 \text{ K}$ ).

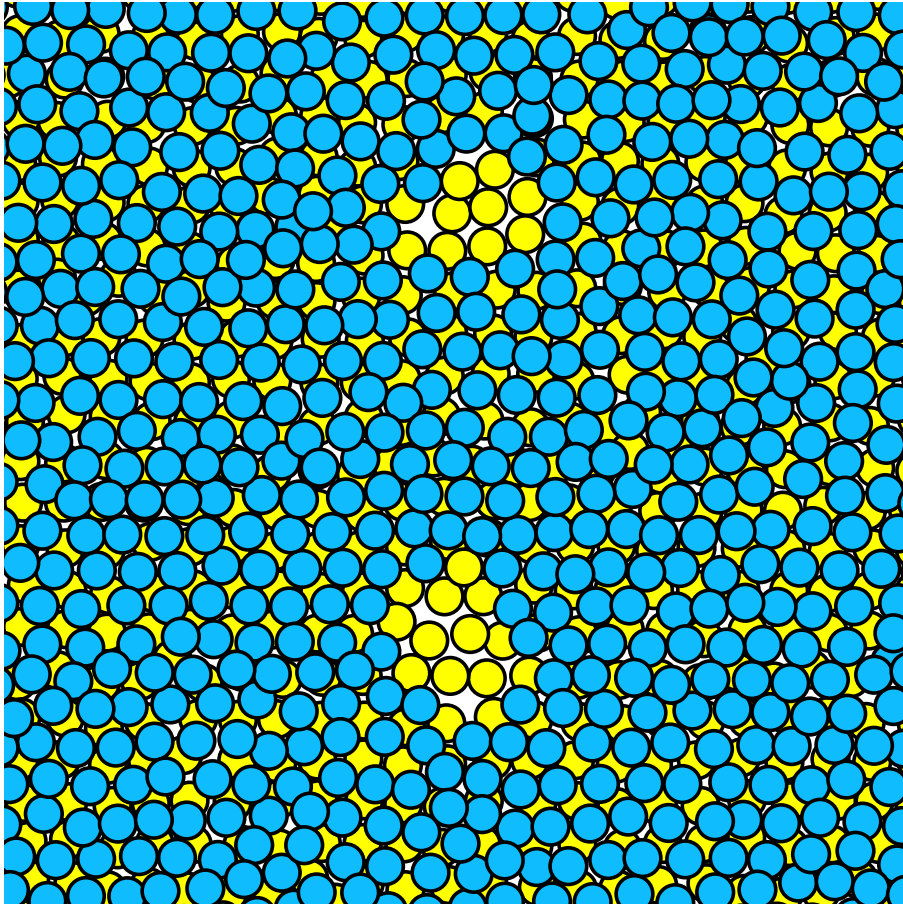


Figure 6.9: At  $t = 277ps$ , two small nuclei of reconstruction appear in both craters. The size of the nuclei is smaller than the critical size for homogeneous growth of reconstructed clusters, and the reconstruction is hindered by the boundary.

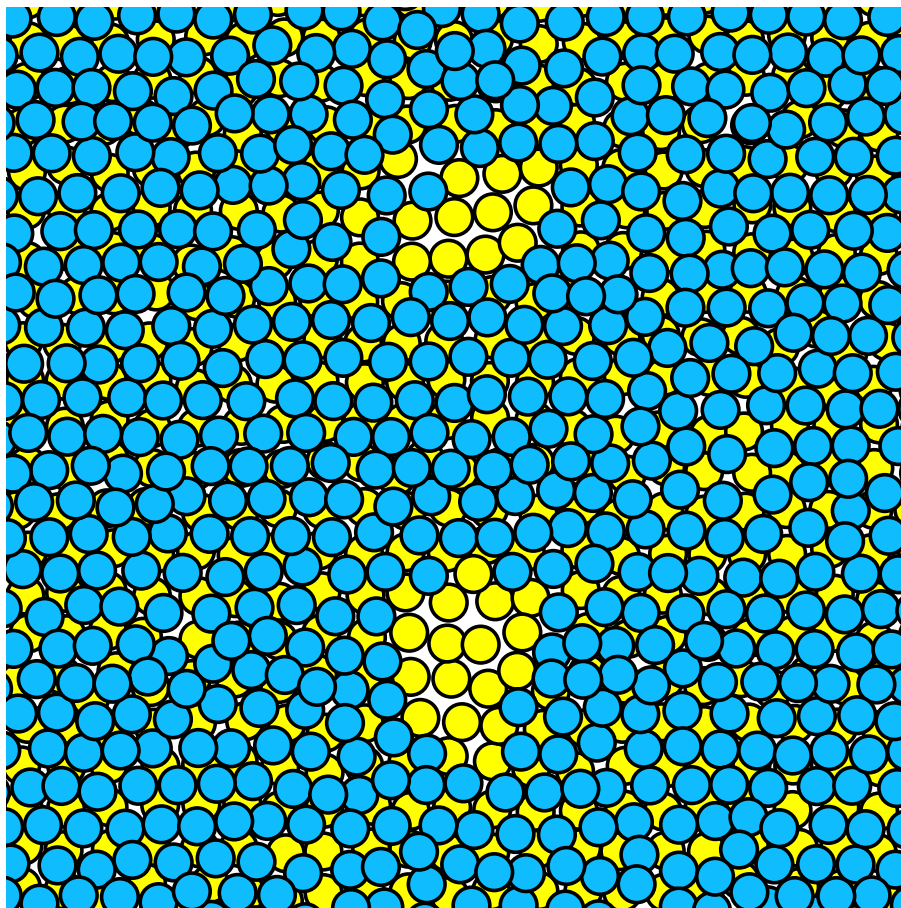


Figure 6.10: At  $t = 344ps$ , in the lower crater of the figure atoms from the top layer have provided the extra lateral density with respect to the  $(1 \times 1)$  layer. Rows on the bottom of the crater begin to slide in order to achieve a triangular, close packed arrangement.

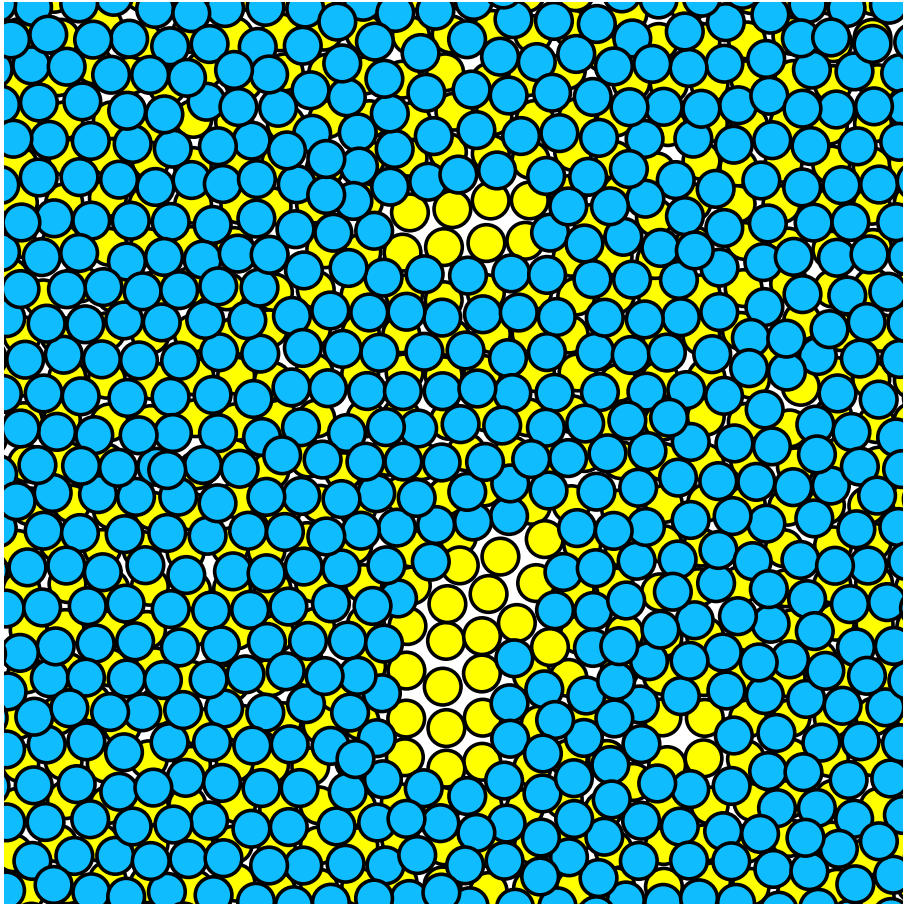


Figure 6.11: At  $t = 412ps$ , whereas the top crater is almost covered, the biggest crater needs more and more atoms in order to reconstruct. The descent of these atoms from the top layer causes an enlargement of the crater and the growth becomes dramatic.

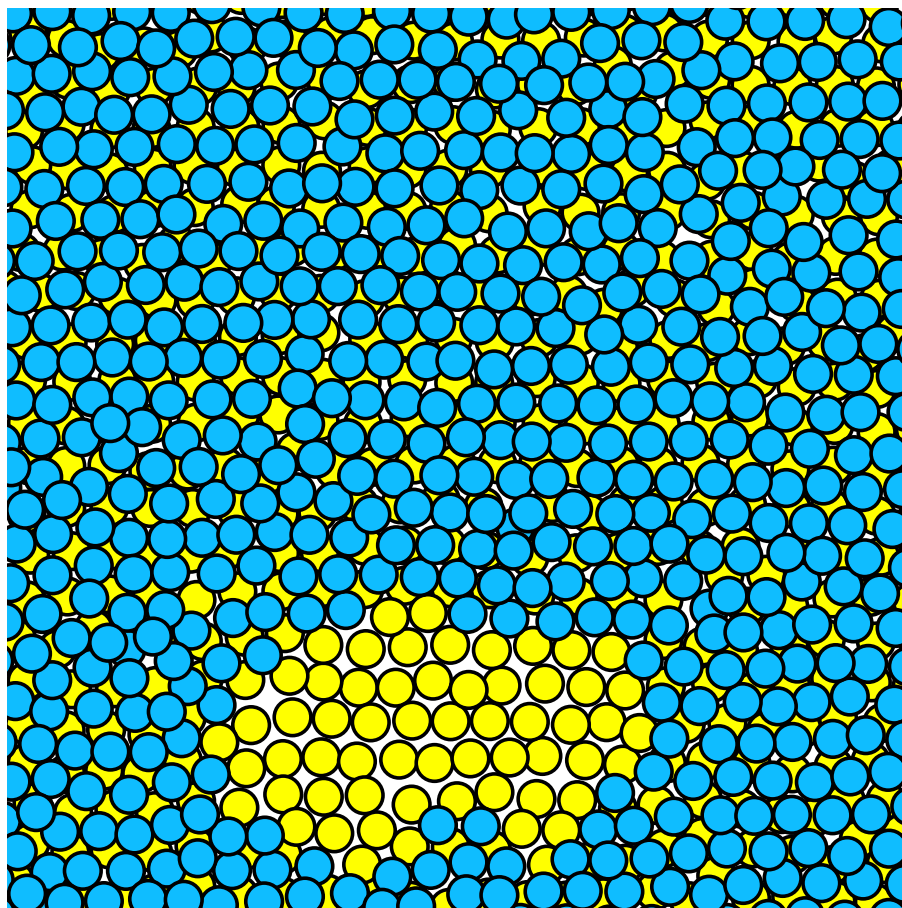


Figure 6.12: At  $t = 1330ps$ , the crater is very large and completely reconstructed. The direction of the close packed rows is the same as in the top layer (experiments on Pt islands adsorbed on Pt(100) [65] confirm this prediction).

by the following mechanism: rows of atoms slide one with respect to the other while particles from the boundary are included in them, and a triangular pattern is obtained.

### 6.2.2 Homogeneous island nucleation

At a temperature of  $T = 1200K$ , we have prepared the surface with an excess lateral density (defined as  $\rho_{ex} = (\rho - \rho_{eq})/\rho_{bulk}$ ) ranging from 0.1 to 0.3. In this case, the driving force for the formation of islands is simply this disequilibrium (we cannot play the reverse trick to crater formation, for in this case we should suddenly quench the temperature: but this causes surface mobility to drop, and waiting times get too long).

Starting from excess densities larger than 10%, equilibration for about 1 nanosecond brought the system to an excess density of about 0.02, whereas the density of the second layer increased up to a value of about 1.12. We found that an excess densities smaller than 0.06 are not sufficient for nucleation of islands. For larger excess densities, islands form but they are initially very small ( $\leq 8$  atoms) and do not grow.

In Figure 6.13 we observe the time evolution of maximum island size observed with an excess density (at equilibrium) of 0.02. The maximum size of an island is about 8 atoms, but no growth is observable. They are under the critical size, and the reason is that the substrate has not yet locally deconstructed. For a sufficiently large excess, and after a suitable waiting time, a stable island eventually grows: this growth is shown in Figure 6.14. We note a takeoff in the number of atoms in this island, and the two contrasting behaviour can be seen together in Figure 6.15.

### 6.2.3 Details of deconstruction under an island

In this section we want to show how the growth of an island is connected with the deconstruction under the island itself. The mechanism is the following. As long as the island is small, (*i.e.* less than  $\sim 12 - 15$  atoms) there is no possibility of deconstruction under it. The border of the island has the same role of the single step described in Chapter 3; there is therefore a correlation length for the influence of the step on the reconstruction under the island. No deconstruction

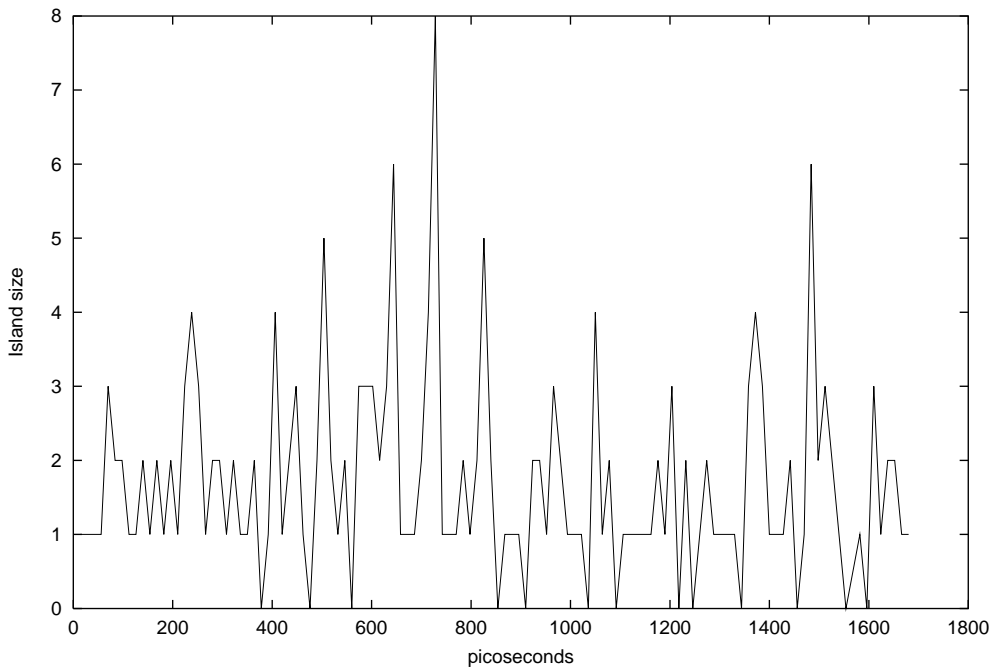


Figure 6.13: The maximum island size for an excess density of about 0.02.

occurs until the diameter of the island is greater than this correlation length.

When the size of the nucleated island allows under it the onset of deconstruction, growth can continue, supplied by the excess atoms ejected by the lower layer. These atoms correspond to the density difference between hexagonal and square order under the island. The deconstruction is almost completed when the island has a size of about 25 – 30 atoms.

A pictorial sketch of this situation is shown in Figure 6.16.

### 6.3 Connection with the step correlation length $\xi$

There appears therefore to be a connection between the critical nucleus for formation of holes and islands and the width of the perturbation of the underlying density caused by a step on a surface. We can infer from the two situations we have examined (the crater formation and the island growth) that reconstruction and deconstruction play a crucial role in determining the onset craters and islands growth. In the same spirit of the heterogeneous adsorption experiment, a critical size for a concerted, collective phenomenon such as deconstruction-

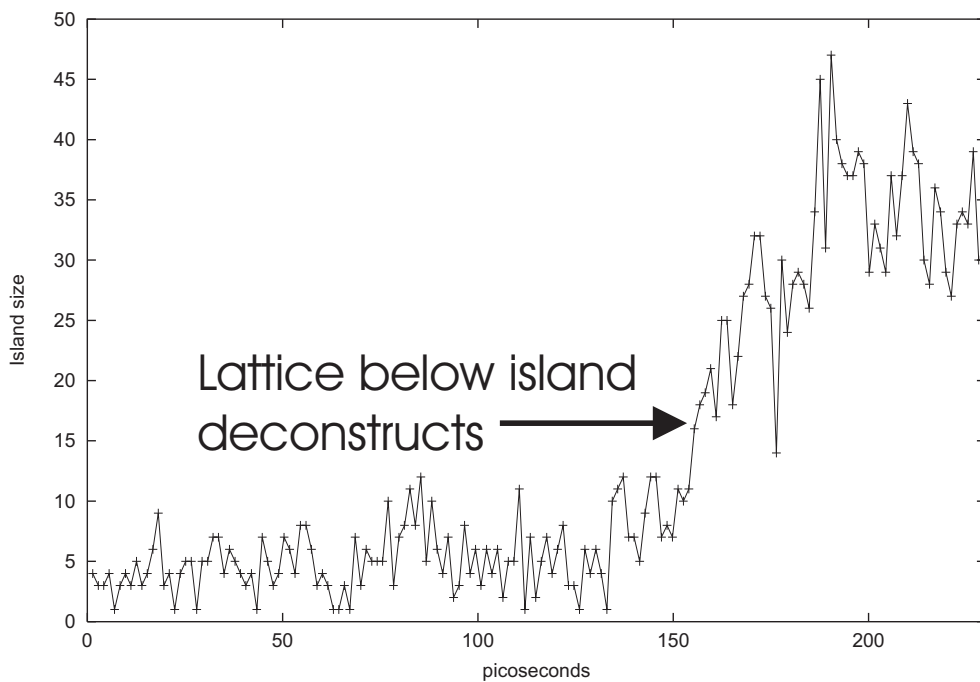


Figure 6.14: The maximum island size for an excess density of about 0.06. There is a jump in the island size and a growth up to a saturation value of about 38 atoms, corresponding to the initial excess density. The arrow indicates the onset of deconstruction of the substrate under the island. This deconstruction is completed at a size of about 20.

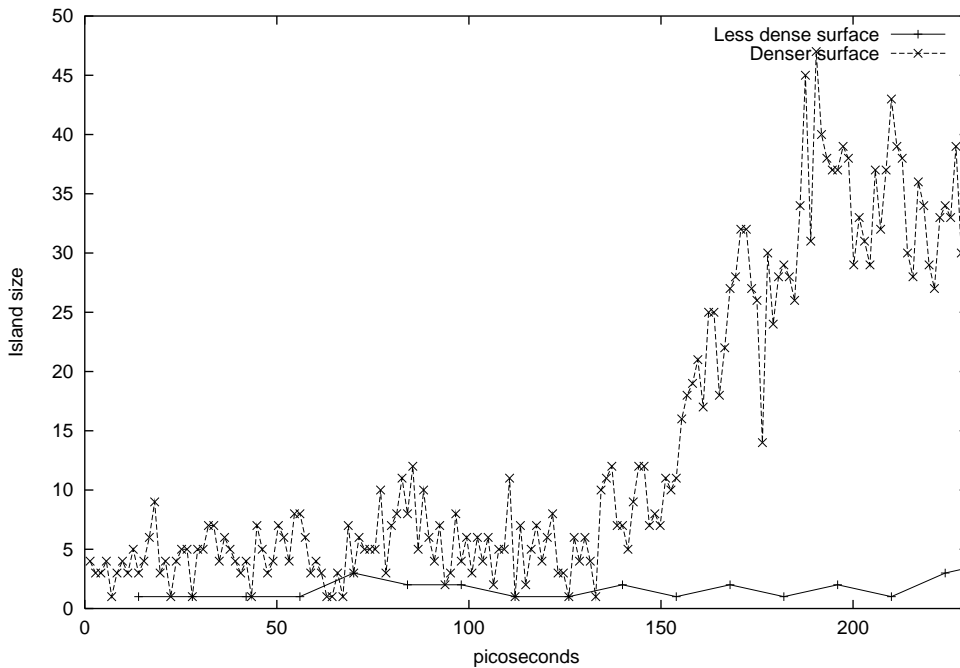
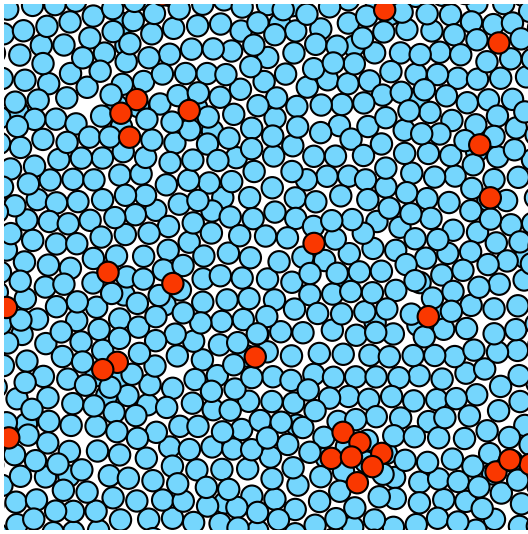


Figure 6.15: The two situations compared on the same  $y$ -scale

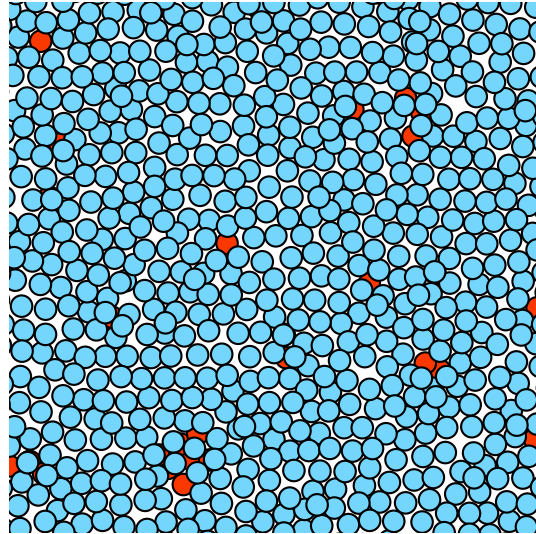
reconstruction has been found; moreover, the ‘range of influence’ of the defect boundary is in rough agreement with the correlation length obtained in Chapter 3. In fact, if the step correlation length is  $\xi$ , then the minimal area for an island or a crater to exist, compatibly with deconstruction of the island substrate or with reconstruction of the crater bottom, is  $\pi\xi^2$ . The corresponding number of atoms involved is

$$N_c = \pi\xi^2\rho_A \quad (6.2)$$

For  $\xi = 5\text{\AA}$ ,  $\rho_A = 0.12$ . This yields  $N_c = 9.4$  atoms, which is exactly in the observed range of 8 – 10. While a more detailed analysis of the concerted local reconstruction/deconstruction process, and of the reasons which make the crossing of this particular transition state a peculiarly slow process is still to be carried out, we may still tentatively conclude that King’s type of exponents can be explained by a step correlation length via (6.2). More simulations would be needed in order to verify temperature dependence of this critical size. In our opinion, only the kinetics of the process is affected by temperature: the number of atoms participating to the deconstruction (reconstruction) transition will remain the same, and so will the critical size for growth.

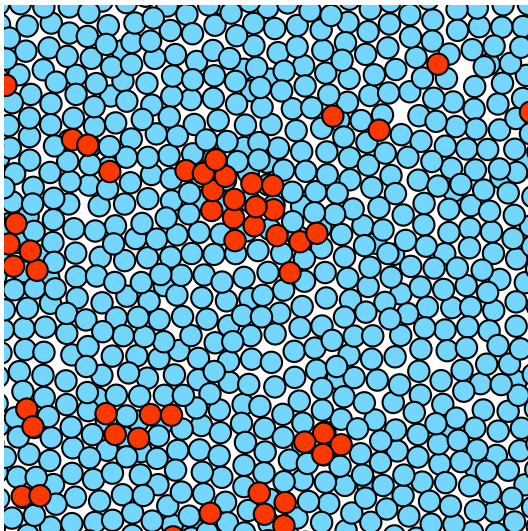


TOP VIEW

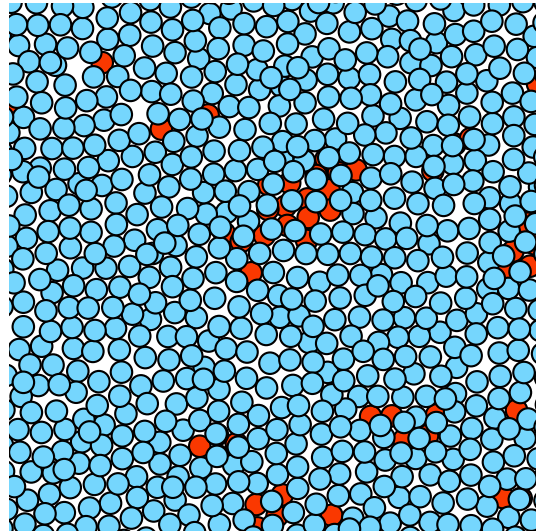


BOTTOM VIEW

Figure 6.16: (color) Some snapshots of island growth. For each figure, the surface seen from the top and from the bottom is presented. At  $t = 0$ , only few adatoms are present on the surface.



TOP VIEW



BOTTOM VIEW

Figure 6.17: (color) At  $t = 147ps$ , there is nucleation of small red islands.

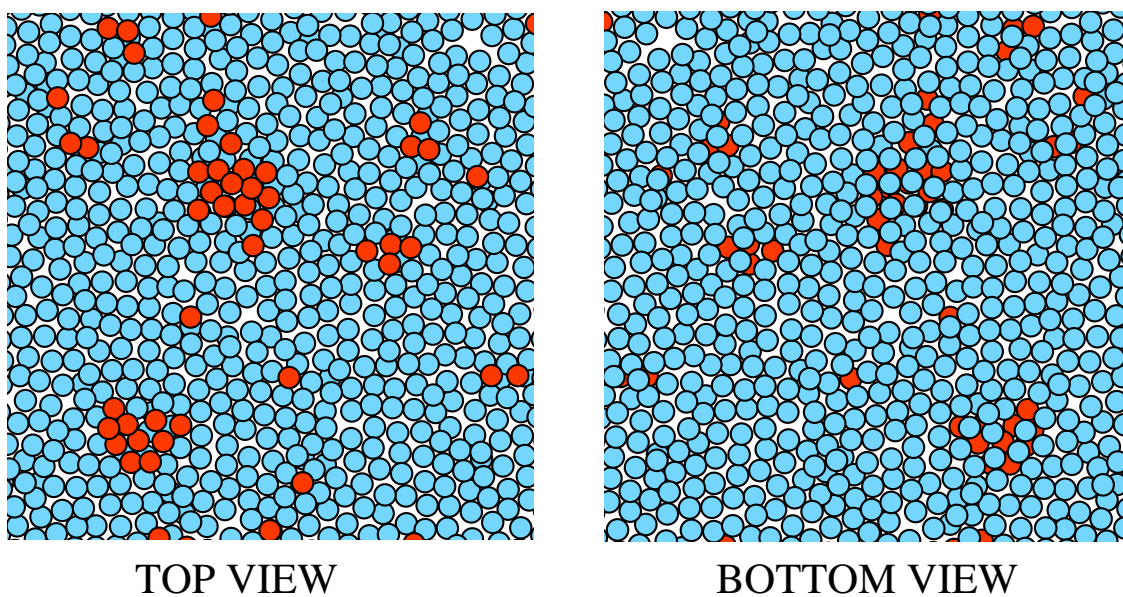


Figure 6.18: (color) At  $t = 150ps$ , blue atoms under the small islands try to assume a squared arrangement, but the boundary of the island hinders this tendency.

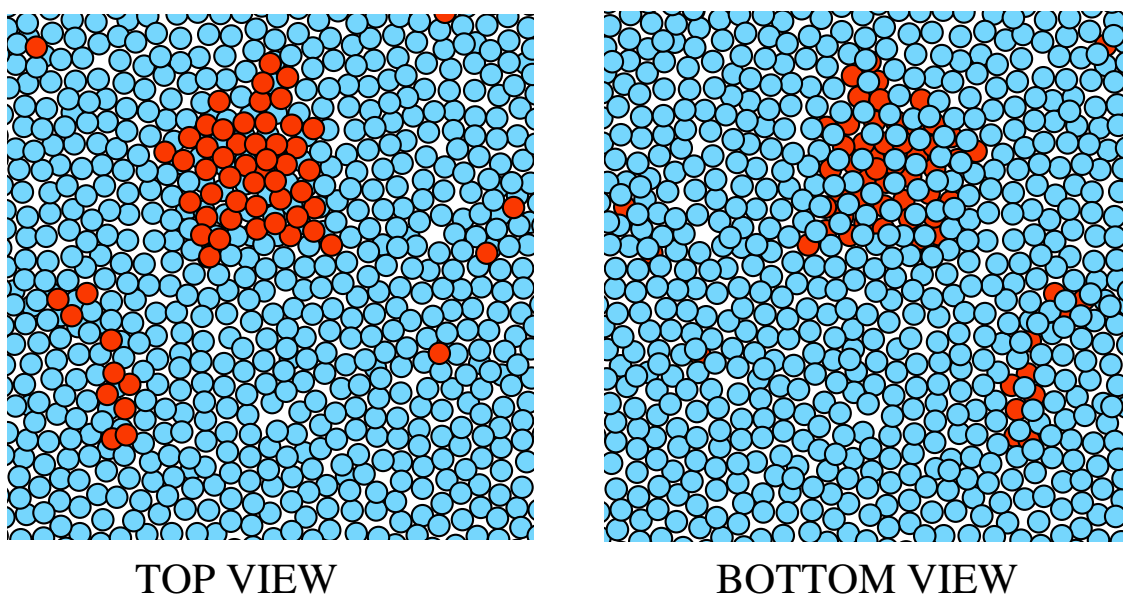
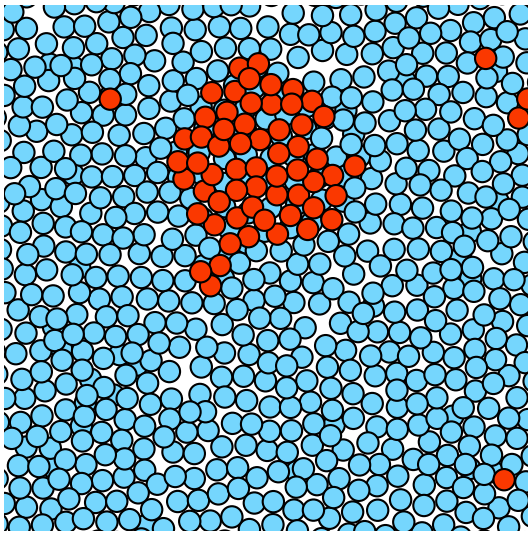
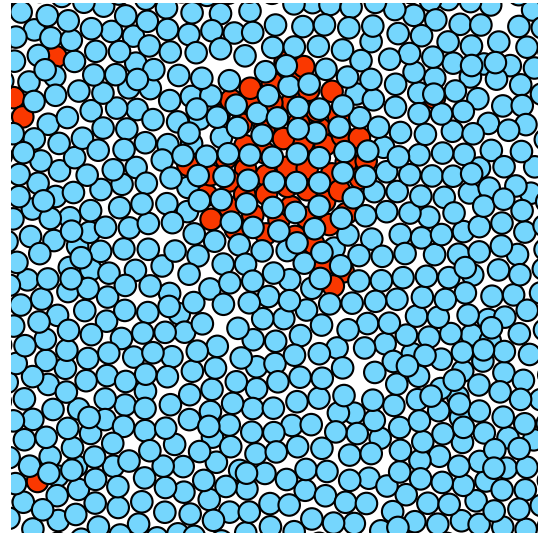


Figure 6.19: (color) At  $t = 175ps$ , only one island continues its growth, and under it deconstruction occurs.

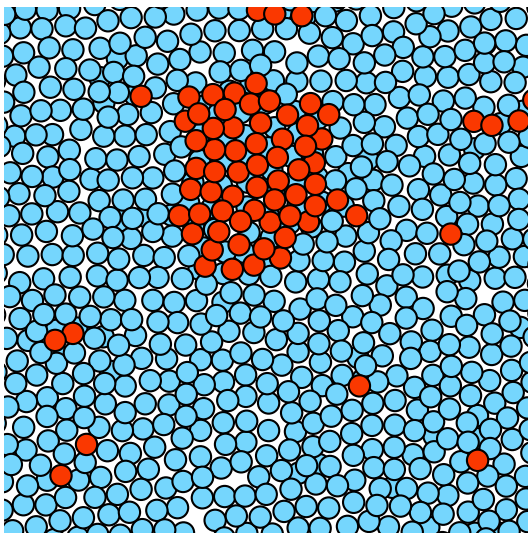


TOP VIEW

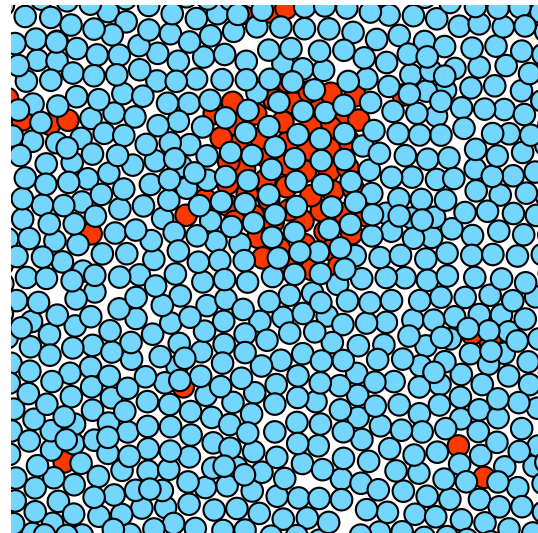


BOTTOM VIEW

Figure 6.20: (color) ( $t = 188ps$ ). Extra atoms expelled by the bottom layer when deconstruction to  $1 \times 1$  phase occurs broaden the upperlying island.



TOP VIEW



BOTTOM VIEW

Figure 6.21: (color) At  $t = 190ps$  the deconstruction under the island is almost complete.



# Chapter 7

## Theory of variable curvature MD

### 7.1 Introduction

There has been recently a reevaluation of the role of surface stress, as an important microscopic indicator of the state of a crystal surface. Recent experimental and theoretical aspects of issues related to surface stress have been reviewed by Ibach [66].

A good example of connection between micro- and macroscopic quantities is the determination of surface stress from the measurement of macroscopic deformations of a thin plate-shaped sample. According to elasticity theory [67], if a thin plate presents a stress difference between its two surfaces, it will bend in order to minimize its total free energy. In the limit of small deformations, a simple formula connects stress difference, thickness, curvature and elastic properties of the sample. Several methods have been recently used to measure the bending. They are mainly optical or based on scanning tunneling microscopy (STM)[66]. Flinn, Gardner and Nix [68] discussed a laser scanning technique to measure the stress-induced curvature, and presented experimental results for stress in Al-Si films as a function of temperature. Martinez, Augustyniak and

Golovchenko [69] measured surface-stress changes resulting from monolayer and sub-monolayer coverages of gallium on Si(111). They used LDA calculations of stress in the Ga-covered Si(111) for the first determination of stress in the Si(111)  $7 \times 7$  and Si(Ga) superlattice surfaces. Stress variations associated with deconstruction of Au(111) and Au(100) were obtained by STM [70, 71]. Moreover, the influence of adsorbates on surface stress has been exploited using the sample bending method for C/Ni(111) [72], S/Ni(111) [73], Co/Ni(100) [74], K/Pt(111) [75], Co/Pt(111) [76], Ag/Pt(111) [77].

An atomistic simulation method which controls the curvature of a sample as an extra degree of freedom has not been available so far, although this would seem a potentially useful tool. The situations in which surface stress varies when physical phenomena occur at interfaces are numerous: adsorbates, reconstructions, steps, phase transitions can change surface stress dramatically. All of these phenomena are, under some conditions, well described by suitable MD simulations. A simulation method where the slab curvature can be measured as a function of adsorbate coverage should represent a powerful connection between important microscopic and macroscopic quantities.

In this chapter we describe and demonstrate a scheme which is meant to fill this gap. It is a classical MD method, but it could in principle be extended to ab initio MD calculations. It is based on extending the usual concept of variable cell MD, pioneered by Andersen [78] and by Parrinello and Rahman [16], to a slab with variable curvature. In our formulation the curvature is a single, global Lagrangian degree of freedom. Surface stress can be extracted as a direct result of the calculation through elasticity equations [79], which will be described below.

The outline of the chapter is as follows: §7.2 will present the theory and geometric considerations underlying our simulation. In §7.3 the phenomenology of a bent plate is reviewed in order to extract the pertinent equations. In section §7.4 we present some initial applications of the method. Finally, section §7.5 is devoted to discussion and conclusions.

## 7.2 Theory

In ordinary variable-cell MD, the coordinates of an atom can be written as

$$\mathbf{r}_i = \hat{\mathbf{H}} \cdot \mathbf{s}_i, \quad (7.1)$$

where  $\mathbf{r}_i$  is the position vector of the  $i$ -th particle,  $\mathbf{s}_i$  are scaled coordinates ( $s_i^j, j = 1 \dots 3$  are held between  $-0.5$  and  $0.5$ ) and  $\hat{\mathbf{H}}$  is a matrix describing the space metric inside the cell. Supposing, as was done by Parrinello and Rahman [16], that the cell can vary in volume and shape, these variations can be accounted for by  $\hat{\mathbf{H}}$ , whose elements can be treated as an extra set of dynamical degrees of freedom. Our aim is to extend this kind of approach to the case of a bending plate, through a different choice of the metric  $\hat{\mathbf{H}}$ .

Let us start with a slab-shaped system, with two surfaces and lateral  $(x, y)$  periodic boundary conditions (PBC). Suppose we bend the slab cylindrically through a radius  $R$  (see Figure 7.1). A convenient choice of the transformation matrix, convenient to our problem, could be the following:

$$\mathbf{r} = \hat{\mathbf{H}}(\mathbf{s}, R) \cdot \mathbf{s}, \quad (7.2)$$

where  $\hat{\mathbf{H}}$ , depending parametrically on the radius of curvature  $R$ , is no longer uniform (as in the Parrinello-Rahman scheme), but rather depends on the point  $\mathbf{s}$ . This dependence is what originates the curvature. In Figure 7.1, for example,  $s_1$  goes from  $-0.5$  to  $0.5$  along  $x$ , which we choose to be unaffected by curvature,  $s_2$  goes from  $-0.5$  to  $0.5$  along direction  $y$  which follows the curvature, and  $s_3$  spans the sample from its inner to its outer surface.

From now on, we will use as reference surface an ideal “neutral cylinder” inside the slab, defined by  $s_3 = 0$ . In particular, we define the curvature  $k$  as the inverse radius of the neutral cylinder:

$$k = \frac{1}{R} \Big|_{s_3=0}. \quad (7.3)$$

In this way, if  $L_y$  is the linear dimension (arc) along the bending direction at  $k = 0$ , the total bending angle is given by  $\theta_M = L_y k$ . Whereas in the Parrinello-Rahman approach the whole matrix  $\hat{\mathbf{H}}$  is treated as a set of additional degrees of freedom, in our case  $\hat{\mathbf{H}}$  is completely determined by the single parameter  $k$  which we will include in the Lagrangian as an extra degree of freedom.

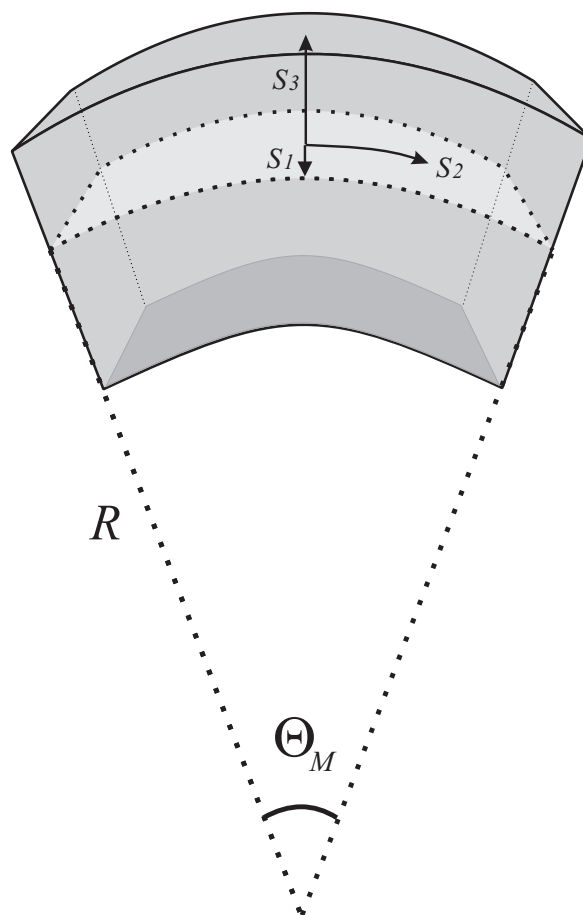


Figure 7.1: The geometry of a bent plate with curvilinear coordinates;  $s_1$  and  $s_2$  lie in the neutral plane (shown as lighter in the figure) whereas  $s_3$  is vertical.  $R$  is the curvature radius measured at  $s_3 = 0$ , and  $\theta_M$  is the bending angle.

### 7.2.1 Lagrangian

The next step is the construction of a Lagrangian. The general, classical Lagrangian for a  $N$ -particle interacting system is:

$$\mathcal{L} = \mathcal{T} - \mathcal{V} = \frac{1}{2} \sum_i m_i \|\dot{\mathbf{r}}_i\|^2 - \mathcal{V}(\mathbf{r}_1 \dots \mathbf{r}_N) \quad (7.4)$$

In Cartesian coordinates  $\dot{\mathbf{r}}_i = \hat{\mathbf{H}} \cdot \dot{\mathbf{s}}_i$  and  $\|\dot{\mathbf{r}}_i\|^2 = \dot{\mathbf{s}}_i^T \hat{\mathbf{G}} \dot{\mathbf{s}}_i$ , where  $\hat{\mathbf{G}} = \hat{\mathbf{H}}^T \hat{\mathbf{H}}$  is the metric tensor[16]. We now define an extended Lagrangian  $\tilde{\mathcal{L}}$  by including an artificial ‘‘curvature kinetic energy’’:

$$\tilde{\mathcal{L}} = \mathcal{L} + \frac{1}{2} W \dot{k}^2, \quad (7.5)$$

where  $W$  acts effectively as a ‘‘curvature inertial mass’’. The velocity of a particle can be written as:

$$\dot{\mathbf{r}} = \frac{d}{dt} (\hat{\mathbf{H}} \cdot \mathbf{s}), \quad (7.6)$$

or explicitly

$$\dot{r}^\alpha = \frac{d}{dt} (H_{\alpha\beta} s^\beta) = \dot{H}_{\alpha\beta}(\mathbf{s}, k) s^\beta + H_{\alpha\beta} \dot{s}^\beta = \left[ \frac{\partial H_{\alpha\beta}}{\partial s^\gamma} \dot{s}^\gamma + \frac{\partial H_{\alpha\beta}}{\partial k} \dot{k} \right] s^\beta + H_{\alpha\beta} \dot{s}^\beta. \quad (7.7)$$

The third term is the usual time derivative for the constant-cell motion, whereas the second term contains a time derivative of the extra degree of freedom  $k$ . As in the Parrinello-Rahman formulation [16], we will omit this term from the definition of the particle velocities. The kinetic energy of the system will therefore depend on  $\dot{k}$  only through the curvature kinetic energy,

$$\tilde{\mathcal{T}} = \frac{1}{2} W \dot{k}^2, \quad (7.8)$$

whose interpretation is discussed in Appendix A. Parrinello and Rahman [16] and Andersen [78], using a similar approach, showed that the equations of motion derived from their Lagrangian satisfy important requisites, leading in particular to correct thermodynamic averages (not dependent on the choice of  $W$ ), and to a correct balance between external and internal stress.

One can then cast (7.7) as

$$\dot{r}^\alpha = \frac{\partial H_{\alpha\beta}}{\partial s^\gamma} \dot{s}^\gamma s^\beta + H_{\alpha\beta} \dot{s}^\beta = \left[ \frac{\partial H_{\alpha\sigma}}{\partial s^\beta} s^\sigma + H_{\alpha\beta} \right] \dot{s}^\beta \doteq M_{\alpha\beta} \dot{s}^\beta. \quad (7.9)$$

The kinetic energy of a particle then becomes

$$\mathcal{T}_1 = \frac{1}{2}m \|\dot{\mathbf{r}}\|^2 = \frac{1}{2}m \dot{s}^\alpha N_{\alpha\beta} \dot{s}^\beta = \frac{1}{2}m \dot{\mathbf{s}}^\mathbf{T} \hat{\mathbf{N}} \dot{\mathbf{s}}, \quad (7.10)$$

where  $\hat{\mathbf{N}} \doteq \hat{\mathbf{M}}^\mathbf{T} \cdot \hat{\mathbf{M}}$ .

We need now to express the potential energy in terms of the scaled coordinates and of the metric. In the following, we will use mostly potentials (such as pairwise potentials or many-body potentials of the ‘glue’ form) which only depend on pair distances:

$$\mathcal{V} = \mathcal{V} \left( \left\{ \|\mathbf{r}_i - \mathbf{r}_j\|^2 \mid i \neq j; i, j = 1 \dots N \right\} \right). \quad (7.11)$$

It is therefore necessary to express  $\|\mathbf{r}_i - \mathbf{r}_j\|^2$  in the new coordinates [80]. Denoting the metric tensor as  $\hat{\mathbf{G}}(k, \mathbf{s}_i) = \hat{\mathbf{H}}^\mathbf{T}(k, \mathbf{s}_i) \cdot \hat{\mathbf{H}}(k, \mathbf{s}_i)$  we have

$$\|\mathbf{r}_i - \mathbf{r}_j\|^2 \equiv r_{ij}^2 = \mathbf{s}_i^\mathbf{T} \hat{\mathbf{G}}(k, \mathbf{s}_i) \mathbf{s}_i + \mathbf{s}_j^\mathbf{T} \hat{\mathbf{G}}(k, \mathbf{s}_j) \mathbf{s}_j - 2 \mathbf{s}_i^\mathbf{T} \hat{\mathbf{H}}^\mathbf{T}(k, \mathbf{s}_i) \cdot \hat{\mathbf{H}}(k, \mathbf{s}_j) \mathbf{s}_j. \quad (7.12)$$

We now have all the ingredients needed to write the  $3N + 1$  Lagrange equations

$$\begin{cases} W \ddot{k} + \frac{\partial \mathcal{V}}{\partial k} - \frac{1}{2} \sum_i m_i \dot{\mathbf{s}}_i^\mathbf{T} \frac{\partial \hat{\mathbf{N}}}{\partial k} \dot{\mathbf{s}}_i = 0 \\ m_l \hat{\mathbf{N}}(k, \mathbf{s}_l) \ddot{\mathbf{s}}_l + \frac{\partial \mathcal{V}}{\partial \mathbf{s}_l} - \frac{1}{2} m_l \dot{\mathbf{s}}_l^\mathbf{T} \frac{\partial \hat{\mathbf{N}}}{\partial \mathbf{s}_l} \dot{\mathbf{s}}_l + m_l \dot{\hat{\mathbf{N}}}(k, \mathbf{s}_l) \dot{\mathbf{s}}_l = 0, \quad l = 1 \dots N. \end{cases} \quad (7.13)$$

## 7.2.2 Construction of the $\hat{\mathbf{H}}$ matrix

To obtain an explicit form for (7.2) and (7.13) we write the expression for the Cartesian coordinates in a box with linear dimensions (at  $k = 0$ )  $L_x$ ,  $L_y$  and  $L_z$ :

$$\begin{cases} x = s_1 L_x \\ y = \left( \frac{1}{k} + s_3 L_z \right) \sin \theta \\ z = s_3 L_z \cos \theta + \frac{1}{k} (\cos \theta - 1). \end{cases} \quad (7.14)$$

where  $\theta$  is the angle running along the  $y$  direction,  $-\theta_M/2 < \theta < \theta_M/2$  (see Figure 7.1). With the help of simple trigonometric formulæ, we can express  $\theta$  in terms of  $s_2$  and  $k$ :

$$\sin \frac{\theta}{2} = 2 s_2 \sin \frac{k L_y}{4} \quad (7.15)$$

whence equations (7.14) become:

$$\begin{cases} x = s_1 L_x \\ y = 4 s_2 \left( \frac{1}{k} + s_3 L_z \right) \sin(k L_y/4) \sqrt{1 - 4 (s_2)^2 \sin^2(k L_y/4)} \\ z = s_3 L_z \left( 1 - 8 (s_2)^2 \sin^2(k L_y/4) \right) - \frac{1}{k} \left( 8 (s_2)^2 \sin^2(k L_y/4) \right) \end{cases} \quad (7.16)$$

By inspection, we see that a possible choice for  $\hat{\mathbf{H}}$  is ( $u = L_y/4$ ):

$$\hat{\mathbf{H}}(s_2, k) = \begin{pmatrix} L_x & 0 & 0 \\ 0 & 4 \frac{\sin(k u)}{k} \sqrt{1 - 4 (s_2)^2 \sin^2(k u)} & 4 s_2 L_z \sin \frac{k L_y}{4} \sqrt{1 - 4 (s_2)^2 \sin^2(k u)} \\ 0 & -s_2 \frac{\sin^2(k u)}{k} & L_z \left( 1 - 8 (s_2)^2 \sin^2(k u) \right) \end{pmatrix} \quad (7.17)$$

It can be easily shown that eq. (7.2) is verified and that, in the limit of zero curvature,  $\lim_{k \rightarrow 0} \hat{\mathbf{H}}(s_2, k) = \text{diag}[L_x, L_y, L_z]$ , that is, the Cartesian  $\hat{\mathbf{H}}$  matrix is recovered. Moreover, the same equations are exact in the limit of finite, fixed curvature.

The explicit form of  $\hat{\mathbf{N}}$  can be obtained by using equations (7.10) and (7.17):

$$N_{\alpha\beta} = \begin{pmatrix} L_x^2 & 0 & 0 \\ 0 & \frac{16(k L_z s_3 + 1)^2 \sin^2(k u)}{(1 - 4(s_2)^2 \sin^2(k u)) k^2} & 0 \\ 0 & 0 & L_z^2 \end{pmatrix}. \quad (7.18)$$

$\hat{\mathbf{N}}$  is diagonal as a consequence of the chosen cylindrical geometry.

### 7.2.3 Explicit form of the equations of motion

In this subsection, we will present the explicit form of the eq. (7.13) in the case of a glue potential whose form is the following:

$$\begin{aligned} V &= \frac{1}{2} \sum_{i,j} \Phi(r_{ij}) + \sum_i U(n_i) \\ n_i &= \sum_j \rho(r_{ij}). \end{aligned}$$

The first term we want to calculate is the first derivative of the potential with respect to the curvature  $k$ :

$$\frac{\partial V}{\partial k} = \frac{1}{2} \sum_i \left( \sum_j \frac{\partial \Phi}{\partial r_{ij}} \frac{\partial r_{ij}}{\partial k} \right) +$$

$$\begin{aligned}
& + \sum_i U'(n_i) \sum_j \frac{\partial \rho}{\partial r_{ij}} \frac{\partial r_{ij}}{\partial k} = \\
& \frac{1}{2} \sum_{i,j} \left( \frac{\partial \Phi}{\partial r_{ij}} + 2U'(n_i) \frac{\partial \rho}{\partial r_{ij}} \right) \frac{\partial r_{ij}}{\partial k};
\end{aligned}$$

at this point we recall the expression of  $r_{ij}$ :

$$r_{ij} = \left( \mathbf{s}_i^T \hat{\mathbf{G}}(k, \mathbf{s}_i) \mathbf{s}_i + \mathbf{s}_j^T \hat{\mathbf{G}}(k, \mathbf{s}_j) \mathbf{s}_j - 2 \mathbf{s}_i^T \hat{\mathbf{H}}^T(k, \mathbf{s}_i) \cdot \hat{\mathbf{H}}(k, \mathbf{s}_j) \mathbf{s}_j \right)^{\frac{1}{2}};$$

so we obtain

$$\begin{aligned}
\frac{\partial r_{ij}}{\partial k} &= \frac{1}{2r_{ij}} \frac{\partial r_{ij}^2}{\partial k} = \frac{1}{2r_{ij}} \left( \mathbf{s}_i^T \frac{\partial \hat{\mathbf{G}}(k, \mathbf{s}_i)}{\partial k} \mathbf{s}_i + \mathbf{s}_j^T \frac{\partial \hat{\mathbf{G}}(k, \mathbf{s}_j)}{\partial k} \mathbf{s}_j \right. \\
&\quad \left. - 2 \mathbf{s}_i^T \frac{\partial \hat{\mathbf{H}}^T(k, \mathbf{s}_i)}{\partial k} \cdot \hat{\mathbf{H}}(k, \mathbf{s}_j) \mathbf{s}_j - 2 \mathbf{s}_i^T \hat{\mathbf{H}}^T(k, \mathbf{s}_i) \cdot \frac{\partial \hat{\mathbf{H}}(k, \mathbf{s}_j)}{\partial k} \mathbf{s}_j \right).
\end{aligned}$$

The whole expression for  $\frac{\partial V}{\partial k}$  becomes, using the symmetry between  $i$  and  $j$  in  $U(n)$ :

$$\begin{aligned}
\frac{\partial V}{\partial k} &= \frac{1}{2} \sum_{i,j} \frac{1}{2r_{ij}} \left( \frac{\partial \Phi}{\partial r_{ij}} + \frac{\partial \rho}{\partial r_{ij}} [U'(n_i) + U'(n_j)] \right) \\
&\quad \left( \mathbf{s}_i^T \frac{\partial \hat{\mathbf{G}}(k, \mathbf{s}_i)}{\partial k} \mathbf{s}_i + \mathbf{s}_j^T \frac{\partial \hat{\mathbf{G}}(k, \mathbf{s}_j)}{\partial k} \mathbf{s}_j \right. \\
&\quad \left. - 2 \mathbf{s}_i^T \frac{\partial \hat{\mathbf{H}}^T(k, \mathbf{s}_i)}{\partial k} \cdot \hat{\mathbf{H}}(k, \mathbf{s}_j) \mathbf{s}_j - 2 \mathbf{s}_i^T \hat{\mathbf{H}}^T(k, \mathbf{s}_i) \cdot \frac{\partial \hat{\mathbf{H}}(k, \mathbf{s}_j)}{\partial k} \mathbf{s}_j \right).
\end{aligned}$$

the derivatives of  $\Phi$ ,  $\rho$  and  $U$  are obtained from a table, whereas the other derivatives are given here for reference:

$$\begin{aligned}
\frac{\partial H_{11}}{\partial k} &= 0 \\
\frac{\partial H_{22}}{\partial k} &= j(k, s_2) \left( L_y \frac{\cos\left(k \frac{L_y}{4}\right)}{k} - \frac{4 \sin(ku)}{k^2} \right) \\
&\quad - 4L_y \frac{\sin^2\left(k \frac{L_y}{4}\right)}{k} (s_2)^2 \frac{\cos\left(k \frac{L_y}{4}\right)}{j(k, s_2)}
\end{aligned}$$

$$\begin{aligned}
\frac{\partial H_{33}}{\partial k} &= -4 (s_2)^2 L_y L_z \sin\left(k \frac{L_y}{4}\right) \cos\left(k \frac{L_y}{4}\right) \\
\frac{\partial H_{23}}{\partial k} &= L_y L_z \left( \cos\left(k \frac{L_y}{4}\right) s_2 j(k, s_2) - 4 \frac{(s_2)^3 \sin^2\left(k \frac{L_y}{4}\right) \cos\left(k \frac{L_y}{4}\right)}{(s_2)^2} \right) \\
\frac{\partial H_{32}}{\partial k} &= -4 (s_2)^2 L_y L_z \sin\left(k \frac{L_y}{4}\right) \cos\left(k \frac{L_y}{4}\right) \\
\frac{\partial G_{11}}{\partial k} &= \frac{\partial G_{33}}{\partial k} = 0 \\
\frac{\partial G_{22}}{\partial k} &= \frac{32}{k^2} \left( \frac{L_y}{4} \cos\left(k \frac{L_y}{4}\right) - \frac{\sin\left(k \frac{L_y}{4}\right)}{k} \right) \\
\frac{\partial G_{23}}{\partial k} &= \frac{\partial G_{32}}{\partial k} = 8 s_2 L_z \left( L_y \frac{\sin\left(k \frac{L_y}{4}\right) \cos\left(k \frac{L_y}{4}\right)}{2k} - \frac{\sin^2\left(k \frac{L_y}{4}\right)}{k^2} \right) \\
j(k, s_2) &\doteq \sqrt{1 - 4 \sin^2\left(k \frac{L_y}{4}\right) (s_2)^2}.
\end{aligned}$$

All these expressions converge to finite limits for  $k \rightarrow 0$ . Now, we calculate the derivatives of the potential with respect to atomic coordinates:

$$\begin{aligned}
\frac{\partial V}{\partial \mathbf{s}_l} &= \frac{1}{2} \sum_{i,j} \frac{1}{2r_{ij}} \left( \frac{\partial \Phi}{\partial r_{ij}} + 2U'(n_i) \frac{\partial \rho}{\partial r_{ij}} \right) \frac{\partial r_{ij}^2}{\partial \mathbf{s}_l}; \\
\frac{\partial r_{ij}^2}{\partial s_{(l)}^\omega} &= \frac{\partial}{\partial s_{(l)}^\omega} \left( s_{(i)}^\alpha G_{\alpha\beta}(k, \mathbf{s}_i) s_{(i)}^\beta + s_{(j)}^\alpha G_{\alpha\beta}(k, \mathbf{s}_j) s_{(j)}^\beta \right. \\
&\quad \left. - 2 s_{(i)}^\beta H_{\alpha\beta}(k, \mathbf{s}_i) \cdot H_{\gamma\delta}(k, \mathbf{s}_j) s_{(j)}^\delta \delta_{\alpha,\gamma} \right) = \\
&\quad (\delta_{l,j} + \delta_{l,i}) \left( 2G_{\omega\beta}(k, \mathbf{s}_l) s_{(l)}^\beta + s_{(l)}^\alpha \frac{\partial G_{\alpha\beta}(k, \mathbf{s}_l)}{\partial s_{(l)}^\omega} s_{(l)}^\beta \right) + \\
&\quad - 2 \left( H_{\alpha\beta}(k, \mathbf{s}_j) s_{(j)}^\beta \delta_{l,i} + H_{\alpha\beta}(k, \mathbf{s}_i) s_{(i)}^\beta \delta_{l,j} \right) \\
&\quad \left[ \frac{\partial H_{\alpha\delta}(k, \mathbf{s}_l)}{\partial s_{(l)}^\omega} s_{(l)}^\delta + H_{\alpha\omega}(k, \mathbf{s}_l) \right];
\end{aligned}$$

so that the expression for the derivative of  $V$  with respect to  $s_{(l)}^\omega$  is:

$$\frac{\partial V}{\partial s_{(l)}^\omega} = \frac{1}{4} \sum_j \frac{1}{r_{lj}} \left( \frac{\partial \Phi}{\partial r_{lj}} + [U'(n_l) + U'(n_j)] \frac{\partial \rho}{\partial r_{lj}} \right).$$

$$\left( 4G_{\omega\beta}(k, \mathbf{s}_l) s_{(l)}^\beta + 2s_{(l)}^\alpha \frac{\partial G_{\alpha\beta}(k, \mathbf{s}_l)}{\partial s_{(l)}^\omega} s_{(l)}^\beta + \right. \\ \left. -4H_{\alpha\beta}(k, \mathbf{s}_j) s_{(j)}^\beta \left[ \frac{\partial H_{\alpha\delta}(k, \mathbf{s}_l)}{\partial s_{(l)}^\omega} s_{(l)}^\delta + H_{\alpha\omega}(k, \mathbf{s}_l) \right] \right).$$

$\hat{\mathbf{N}}^{-1}$ ,  $\frac{\partial \hat{\mathbf{N}}}{\partial k}$ ,  $\frac{\partial \hat{\mathbf{N}}}{\partial \mathbf{s}}$  and  $\dot{\mathbf{N}}$  are given here for completeness:

$$\hat{\mathbf{N}}^{-1} = \begin{pmatrix} \frac{1}{L_x^2} & 0 & 0 \\ 0 & \frac{k^2(1-4(s_2)^2 \sin^2(k\frac{L_y}{4}))}{16(kL_z s_3+1)^2 \sin^2(k\frac{L_y}{4})} & 0 \\ 0 & 0 & \frac{1}{L_z^2} \end{pmatrix}$$

$$\frac{\partial N_{22}}{\partial k} = 32 \frac{\sin(k\frac{L_y}{4})(kL_z s_3 + 1)}{k(4(s_2)^2 \sin^2(k\frac{L_y}{4}) - 1)^2} \cdot$$

$$\left( \frac{k \cos(k\frac{L_y}{4}) L_y - \sin(k\frac{L_y}{4}) + 4(s_2)^2 \sin^3(k\frac{L_y}{4})}{k^2} + \right.$$

$$\left. + \frac{L_y L_z}{4} s_3 \cos(k\frac{L_y}{4}) \right)$$

$$\frac{\partial N_{22}}{\partial s_2} = \frac{128 s_2 (kL_z s_3 + 1)^2 \sin^4(k\frac{L_y}{4})}{k^2 (4(s_2)^2 \sin^2(k\frac{L_y}{4}) - 1)^2}$$

$$\frac{\partial N_{22}}{\partial s_3} = \frac{32 L_z (kL_z s_3 + 1) \sin^2(k\frac{L_y}{4})}{k (4(s_2)^2 \sin^2(k\frac{L_y}{4}) - 1)}$$

$$\frac{d N_{22}}{d t} = \left( \frac{\partial N_{22}}{\partial s_2} \right) \dot{s}_2 + \left( \frac{\partial N_{22}}{\partial s_3} \right) \dot{s}_3 + \left( \frac{\partial N_{22}}{\partial k} \right) \dot{k}.$$

#### 7.2.4 Constrained molecular dynamics and PBC

The Lagrange equations are integrated using numerical methods. In particular, we will use a second order velocity Verlet algorithm, which is at the same time well-tested and simple. We found some problems due to the instability of the center of mass of the sample during the bending, which were overcome and will be commented just below.

Our starting geometry is an  $n$ -layer crystalline slab with PBC along the  $x$  and  $y$  directions. The periodicity is accounted for by the scaled coordinates  $s_1$

and  $s_2$ .

The choice of coordinates we have adopted requires a slightly different set of PBC with respect to usual slab simulations. In the  $x$  direction, nothing changes: the minimum images of a particle with scaled  $x$  coordinate equal to  $s_1$  have simply the coordinates  $(s_1 \pm 1)$ . In  $y$  direction (the bending direction) the requirement is that the angle  $\theta$  of the particle be correctly transformed to the angle  $(\theta \pm \theta_M)$ ; after requesting this condition the scaled  $y$  coordinate of the minimum image is:

$$s_2^{(F)} = \left( 2 \cos^2 \left( \frac{\theta_M}{4} \right) - 1 \right) s_2 + \cos \frac{\theta_M}{4} \sqrt{1 - 4 (s_2)^2 \sin^2 \frac{\theta_M}{4}}. \quad (7.19)$$

When a particle is folded to its image, there is also the requirement that its velocity remain unchanged, following in a suitable way the curvature of the sample. Since the components  $\dot{s}_1$  and  $\dot{s}_3$  do not change, the conservation of the velocity modulus is sufficient in determining  $\dot{s}_2^{(F)}$ :

$$\dot{s}^{(F)} \hat{\mathbf{N}}(\mathbf{s}, k^{(F)}) \dot{s}^{(F)} = \dot{s} \hat{\mathbf{N}}(\mathbf{s}, k) \dot{s}, \quad (7.20)$$

which leads to

$$\dot{s}_2^{(F)} = \dot{s}_2 \frac{N_{22}(\vec{s})}{N_{22}(\vec{s}^{(F)})} = \dot{s}_2 \frac{\sqrt{1 - 4 (s_2^{(F)})^2 \sin^2 \frac{\theta_M}{4}}}{\sqrt{1 - 4 (s_2)^2 \sin^2 \frac{\theta_M}{4}}}. \quad (7.21)$$

On the computational point of view, the quantities involved in these more complicated PBC are already available, since they appear frequently in the forces calculation subroutine; therefore, the simulation time is not further affected.

For  $k \neq 0$  the dynamics generated by (7.13) does not conserve the position of the center of mass of the slab along the radial direction  $s_3$ . To keep the center of mass fixed, we resort to a constrained MD scheme. Constrained MD is a well known technique, and we adopted the method used by Ryckært, Ciccotti and Berendsen [81] and Andersen [82] for simulations of rigid molecules. The main point to be kept in mind is that constraints must be verified *exactly* at every time step, otherwise instabilities will occur. Technical details on the practical implementation of this constraint are given in Appendix B.

The general MD protocol we apply consists of either constant energy runs or constant temperature runs (up to 300 K) obtained by velocity rescaling, followed

by quenching to  $T = 0$ . Occasionally, we also introduced a damping term in the curvature dynamics. We chose a typical time step of the order of  $10^{-14}$ s.

### 7.3 Phenomenology of a bent plate

Before moving on to the actual implementation, it is useful to recall some known results concerning the phenomenology, largely contained in the review by Ibach [66].

The definition of surface stress, according to Gibbs [83], as the “reversible work per unit area required to stretch a surface elastically”, points out the difference of this physical quantity with respect to the surface free energy, defined as the “reversible work per unit area to create a surface”. Stretching a *solid* surface implies modifying the substrate, whereas a simple increase of area does not: whence the difference.

Let us start with the bulk stress tensor, whose element  $\tau_{ij}$  is defined as the  $i$ -th component of the force per unit area acting on the side (with the normal to the surface parallel to the  $j$ -th direction) of a small cube in the sample. The corresponding surface stress tensor can be defined as the deviation of this quantity with respect to the bulk value, integrated along the surface normal:

$$\tau_{ij}^{(s)} = \int_{-\infty}^{+\infty} dz \left[ \tau_{ij}(z) - \tau_{ij}^{(b)} \right] \quad (7.22)$$

The integral gives non-zero contribution only where the value of the stress deviates from the bulk value, *i.e.* at the surface.

Let us consider a rectangular shaped sheet of thickness  $t$ , delimited by two identical (100) surfaces. For our purposes the following simplified construction can be put to use without loss of generality [68]. Schematize the plate at zero curvature as a “substrate” of thickness  $t$  and length  $L$  along  $x_1$ , plus two films adsorbed on it: film  $A$  on the lower part of the plate, and film  $B$  on the upper part. Let  $L_A$  the unconstrained length (along  $x_1$ ) of film  $A$ , and  $L_B$  the length of film  $B$ . Let  $L_B > L$  and  $L_A < L$ . In order to match the length  $L$  of the substrate, the film must be stretched (compressed) by an amount  $\Delta L_I = L - L_I$ , with  $I = A, B$ . The deformed film attached to an undeformed substrate does not represent a condition of minimum free energy; the free energy of the entire system can be lowered by deforming the substrate slightly so as to reduce the deformation of

the film. This deformation has two components: an overall compression of the substrate and a bending of the substrate.

It can be shown [68] that the neutral plane (*i.e.* the plane along which the strain is zero) can be set approximately in the middle of the sheet, and the deviations from this approximation are negligible for most cases. In the following, we will extract the conditions for the minimum free energy of the sheet, allowed to bend along a single direction. For simplicity, we will choose this to be the [100] direction (of course similar formulæ can be derived for any other choice). If we denote the coordinates along the non-bending direction, the bending direction and the normal to the surface with  $s_1$ ,  $s_2$  and  $s_3$  respectively, the situation is similar to the one depicted in Figure 7.1. Each element of the sample is subject to a strain  $\varepsilon_{22}(s_3)$ . The change in free energy per unit area associated to this strain, of an element at height  $s_3$  is:

$$u(s_3) = \int_0^{\varepsilon_{22}(s_3)} \tau_{22}(s_3) d\varepsilon_{22}. \quad (7.23)$$

The total free energy change of the bent sample (per unit area) is:

$$U = \int_{-\frac{t}{2}}^{+\frac{t}{2}} ds_3 \int_0^{\varepsilon_{22}(s_3)} \tau_{22}(s_3) d\varepsilon_{22}. \quad (7.24)$$

We can separate this integral into two surface parts and a bulk part:

$$U = U^{(s+)} + U^{(s-)} + U^{(b)} \quad (7.25a)$$

$$U^{(s+)} = \int_{+\frac{t}{2}-\alpha}^{+\frac{t}{2}} ds_3 \int_0^{\varepsilon_{22}(s_3)} [\tau_{22}(s_3) - \tau_{22}^{(b)}] d\varepsilon_{22} \quad (7.25b)$$

$$U^{(s-)} = \int_{-\frac{t}{2}}^{-\frac{t}{2}+\beta} ds_3 \int_0^{\varepsilon_{22}(s_3)} [\tau_{22}(s_3) - \tau_{22}^{(b)}] d\varepsilon_{22} \quad (7.25c)$$

$$U^{(b)} = \int_{-\frac{t}{2}}^{+\frac{t}{2}} ds_3 \int_0^{\varepsilon_{22}(s_3)} \tau_{22}^{(b)}(s_3) d\varepsilon_{22}. \quad (7.25d)$$

The first two terms lead to the definition of surface stress in the Gibbs sense, and can be written with good approximation:

$$U^{(s+)} + U^{(s-)} = \left( \tau_{22}^{(s)}(+)-\tau_{22}^{(s)}(-) \right) \left( \frac{kt}{2} \right), \quad (7.26)$$

where  $\pm kt/2$  are the strains at the upper and lower surfaces.

The bulk term can be expressed using the elastic constants of the crystal. Hooke's law relates strain and bulk stress tensor components in the following way:

$$\begin{aligned}\varepsilon_{11} &= \sigma_{11} \tau_{11} + \sigma_{12} \tau_{22} \\ \varepsilon_{22} &= \sigma_{12} \tau_{11} + \sigma_{11} \tau_{22}.\end{aligned}\quad (7.27)$$

In our case,  $\varepsilon_{11} = 0$ , therefore, after introducing Young's modulus  $Y$  and Poisson's ratio  $\nu$ :

$$\begin{aligned}Y &= \frac{1}{\sigma_{11}} \\ \nu &= -\frac{\sigma_{12}}{\sigma_{11}},\end{aligned}\quad (7.28)$$

one obtains [66]:

$$\varepsilon_{22} = \frac{1 - \nu^2}{Y} \tau_{22}.\quad (7.29)$$

If we substitute (7.29) into (7.25d) we obtain, after integration,

$$U^{(b)} = \frac{1}{24} \frac{Y}{1 - \nu^2} k^2 t^3,\quad (7.30)$$

the total free energy of the bent plate is then:

$$F = \left( \tau_{11}^{(s)} (+) - \tau_{11}^{(s)} (-) \right) \left( \frac{k t}{2} \right) + \frac{1}{24} \frac{Y}{1 - \nu^2} k^2 t^3.\quad (7.31)$$

Minimizing  $F$  with respect to the curvature, one obtains the equation relating the equilibrium curvature  $k_M$  to the difference in surface stress between upper and lower surface:

$$\Delta \tau^{(s)} = -\frac{Y}{6(1 - \nu^2)} k_M t^2\quad (7.32)$$

where  $Y$  is the Young's modulus,  $\nu$  the Poisson's number,  $k_M$  the curvature and  $t$  the thickness of the sample. This relation is known as Stoney's equation, and was first derived in 1909 (except for the biaxial nature of the stress [79, 66]). We stress that this formula is valid for a uniaxial bending, whereas for an isotropic bending in two directions the factor  $(1 - \nu^2)$  should be replaced by  $(1 - \nu)$ . Another limit of validity is that the plate must be infinitely large, relative to its thickness. In other words, there will be finite thickness corrections in  $(t/L)$

where  $L$  is the lateral  $(x, y)$  size. We did not make any attempt to find these corrections so far.

In the remainder of this section we present the simple derivation of the elastic constants two high symmetry surfaces: (100) bent along [011], and (111).

We start from the elastic stiffnesses  $C_{ij}$  which are related to the compliances  $\sigma_{ij}$  by the equations [84]:

$$\begin{aligned}\sigma_{11} &= \frac{C_{11} + C_{12}}{(C_{11} - C_{12})(C_{11} + 2C_{12})} \\ \sigma_{12} &= -\frac{C_{12}}{(C_{11} - C_{12})(C_{11} + 2C_{12})} \\ \sigma_{44} &= \frac{1}{C_{44}}.\end{aligned}\tag{7.33}$$

If the uniaxial bending is not along a [100] direction and for surface orientations other than (100), the compliances  $\sigma_{11}$  and  $\sigma_{12}$  which appear in (7.28) have to be replaced by effective elastic constants, which in the (100) case, with bending along a [011] direction, have the form:

$$\begin{aligned}\sigma'_{11} &= \sigma_{11} - \frac{1}{2} \left( \sigma_{11} + \sigma_{12} + \frac{1}{2}\sigma_{44} \right) \\ \sigma'_{12} &= \sigma_{12} + \frac{1}{2} \left( \sigma_{11} + \sigma_{12} + \frac{1}{2}\sigma_{44} \right),\end{aligned}\tag{7.34}$$

whereas in the (111) case have the form:

$$\begin{aligned}\sigma'_{11} &= \sigma_{11} - \frac{1}{2} \left( \sigma_{11} + \sigma_{12} + \frac{1}{2}\sigma_{44} \right) \\ \sigma'_{12} &= \sigma_{12} + \frac{1}{6} \left( \sigma_{11} + \sigma_{12} + \frac{1}{2}\sigma_{44} \right).\end{aligned}\tag{7.35}$$

## 7.4 Application to metal surfaces

### 7.4.1 Implementation

The first goal of the variable-curvature MD simulation is to obtain an equilibrium value for the curvature in order to extract the surface stress difference, according to equation (7.32). We can then compare the outcome with the surface stress difference calculated independently using Kirwood's formula [85, 3], and

assess the success of the method. We will also verify the validity of the approach by analyzing the behavior of the curvature as a function of the slab thickness.

We will present two different exemplifications. Far from being exhaustive, these results are only meant to show the feasibility of the method in view of later applications to surface physics.

First we simulated several Au slabs with (100) orientation and different types of reconstruction on the two sides. This test can show the sensitivity of the method: differences of the order of  $5 \text{ meV}/\text{\AA}^2$  can be appreciated. Next we examined the effect of isotropic or anisotropic adsorbates on the surface stress, as exemplified by Pb/Au(100).

All simulations were performed using many-body potentials of the glue type [13]. They have the general form:

$$\begin{aligned} V &= \frac{1}{2} \sum_{i,j} \Phi(r_{ij}) + \sum_i U(n_i) \\ n_i &= \sum_j \rho(r_{ij}), \end{aligned} \quad (7.36)$$

where  $n_i$  is a generalized atomic coordination.  $\Phi(r)$ ,  $U(n)$  and  $\rho(r)$  are empirically constructed, by fitting several properties of the system. Well tested glue potentials are available [86] for Au [13] and Pb [15]. This scheme can be extended to binary systems by introducing a mixed two-body potential  $\Phi_{AB}(r)$ , and assuming  $n_i$  to be a linear superposition of density contributions  $\rho_A$  and  $\rho_B$  supplied respectively by  $A$ - and  $B$ -type atoms to site  $i$  [87]:

$$\begin{aligned} V &= \frac{1}{2} \left[ \sum_{i \in A} \left( \sum_{j \in A} \Phi_{AA}(r_{ij}) + \sum_{j \in B} \Phi_{AB}(r_{ij}) \right) + \sum_{i \in B} \left( \sum_{j \in A} \Phi_{AB}(r_{ij}) + \sum_{j \in B} \Phi_{BB}(r_{ij}) \right) \right] \\ &+ \sum_{i \in A} U_A(n_i) + \sum_{i \in B} U_B(n_i), \end{aligned} \quad (7.37)$$

with

$$n_i = \sum_{j \in A} W_A \rho_A(r_{ij}) + \sum_{j \in B} W_B \rho_B(r_{ij}). \quad (7.38)$$

where  $W_A$  and  $W_B$  are suitable weights. In our case  $W_{\text{Au}} = 1.045$  and  $W_{\text{Pb}} = 0.957$ .

### 7.4.2 A clean surface: change of surface stress with reconstruction

We prepared a family of Au(100) slabs composed by about 600 atoms per layer ( $L_x = 28.78 \text{ \AA}$ ,  $L_y = 172.69 \text{ \AA}$ ), and different thicknesses of 8, 12, 16 and 20 layers, with [011] as the bending direction.

In order to extract numerical values for the surface stress from equation (7.32), we need the correct elastic constants for this case. For the case of Au (as described by the glue model), the elastic stiffnesses have been calculated [88], giving

$$\begin{aligned} C_{11} &= 2.203 \cdot 10^7 \text{ N/cm}^2 \\ C_{12} &= 1.603 \cdot 10^7 \text{ N/cm}^2 \\ C_{44} &= 0.600 \cdot 10^7 \text{ N/cm}^2. \end{aligned} \quad (7.39)$$

With these values, using (7.28) and (7.34), the Young's modulus and the Poisson's ratio for Au(100), with bending along [011], are  $Y_{(100)} = 1.322 \cdot 10^7 \text{ N/cm}^2$  and  $\nu_{(100)} = 0.1022$ .

Both (100) surfaces were prepared in the reconstructed state, characterized by a close-packed triangular overlayer on a square substrate. We chose a fixed reconstructed  $(1 \times 5)$  structure (six [011] rows on top of five) for the reference (lower) surface of the plate, and we changed the nature of the upper surface, ranging from  $(1 \times 3)$  (*i.e.* four surface rows over three substrate rows, a "compressive" situation) to a  $(1 \times 20)$  structure, (a "tensile" situation), touching the  $(1 \times 4)$ ,  $(1 \times 5)$ ,  $(1 \times 6)$ ,  $(1 \times 10)$ ,  $(1 \times 12)$ , and  $(1 \times 15)$  structures. In the  $(1 \times 5)$  case no bending was expected or observed, since the surfaces on the two sides were identical. We also considered  $(11 \times 3)$ ,  $(11 \times 4)$ ,  $(11 \times 5)$ , ... obtained by adding  $[01\bar{1}]$  rows. The lowest energy surface in the glue model is  $(34 \times 5)$ [12], in the experiment is close to  $(28 \times 5)$ , but all  $(M \times 5)$  surfaces differ very slightly in free energy [25, 89, 90, 24]. The essential point here will be that surfaces which differ only very little in energy, for example  $(1 \times 5)$  ( $102.3 \text{ meV/\AA}^2$ ) and  $(1 \times 12)$  ( $103.2 \text{ meV/\AA}^2$ ) may differ enormously in surface stress.

A typical snapshot of the simulation is shown in Figure 7.2.

Figure 7.3 shows the time evolution of the curvature  $k$ . Starting from zero, the slab curvature reaches the equilibrium value very rapidly. A damping term, although not really necessary, has been added in order to speed up the convergence.

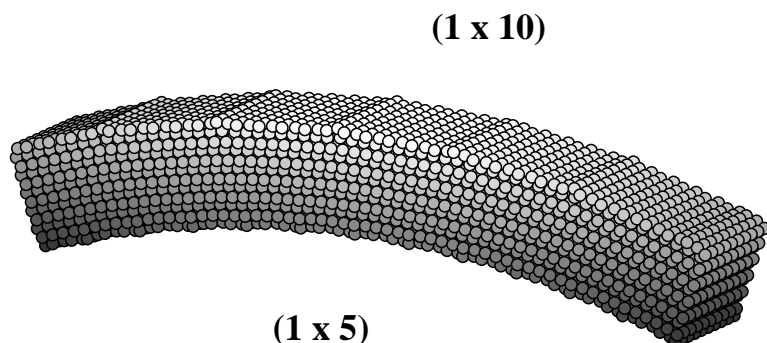


Figure 7.2: A typical snapshot of the simulation, with a positive value of the curvature. The top surface is a  $(1 \times 10)$  and the lower surface a  $(1 \times 5)$ , both hexagonally reconstructed Au(100). The corrugations of both surfaces are evident. This particular sample will invert its curvature during the simulation, and the equilibrium value of  $k$  will be negative.

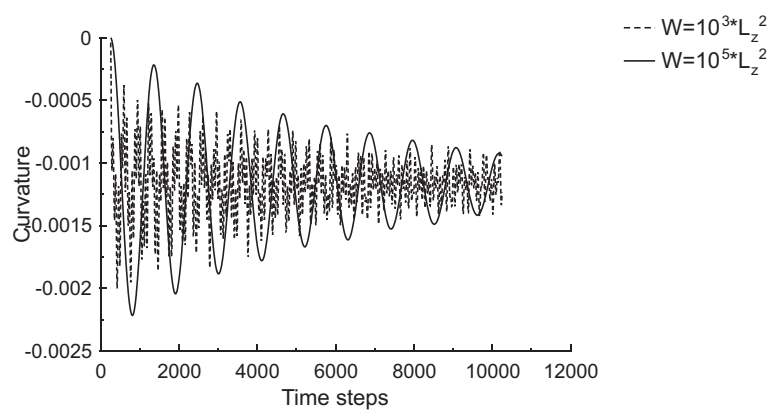


Figure 7.3: Time evolution of the curvature  $k$  for two different values of the 'mass'  $W$ . The curvature is expressed in  $\text{\AA}^{-1}$ .

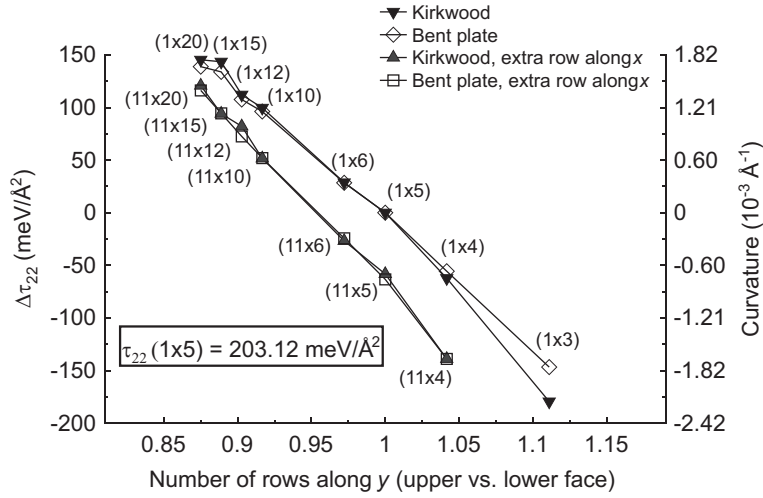


Figure 7.4: Comparison between variable curvature simulations and Kirkwood-Buff formula, with different structures at the upper surface of the sample. The lower surface is a  $(1 \times 5)$  in every case. Right y axis: equilibrium value for the curvature. Left y axis: corresponding difference in surface stress, according to Stoney's equation. In order to obtain the absolute value of the surface stress component  $\tau_{22}$  of the upper surface, the reference  $(1 \times 5)$  result ( $203.12 \text{ meV}/\text{\AA}^2$ ) has to be added.

We verified that, as it should be and as can be seen from the figure, the value of the mass  $W$  is irrelevant in determining the equilibrium value of  $k$ . In the  $(1 \times 3)$  and  $(1 \times 4)$  cases, the equilibrium  $k$  was positive, whereas in the other cases it was negative. The simulation was performed at low temperature (from a few degrees to 300 K). The difference in surface stress between upper and lower surface has been extracted using (7.32). The surface stress of the two isolated surfaces has been independently obtained from MD forces using the standard Kirkwood-Buff formula [3]. This formula essentially connects the stress tensor components from a particular integral of the internal forces, and it was extended from the pairwise potentials case to the glue potential [91]

The comparison of the stress differences is excellent, as can be seen from Figure 7.4, showing that the variable curvature method works. The only deviation is for  $(1 \times 3)$ , and clearly attributable to excessive curvature.

The calculation is repeated with a variety of different unit cells in the top surface; by adding a  $[01\bar{1}]$  row every ten, we obtain  $(11 \times 3)$ ,  $(11 \times 4)$ ,  $(11 \times 5)$ , ... unit cells instead of  $(1 \times 3)$ ,  $(1 \times 4)$ ,  $(1 \times 5)$ , ... The lower  $(1 \times 5)$  surface of the slab was left unchanged. The stress variations are clearly very large, both relative to the basic stress of  $(1 \times 5)$  ( $203.12 \text{ meV}/\text{\AA}^2$ ) and to the surface energy

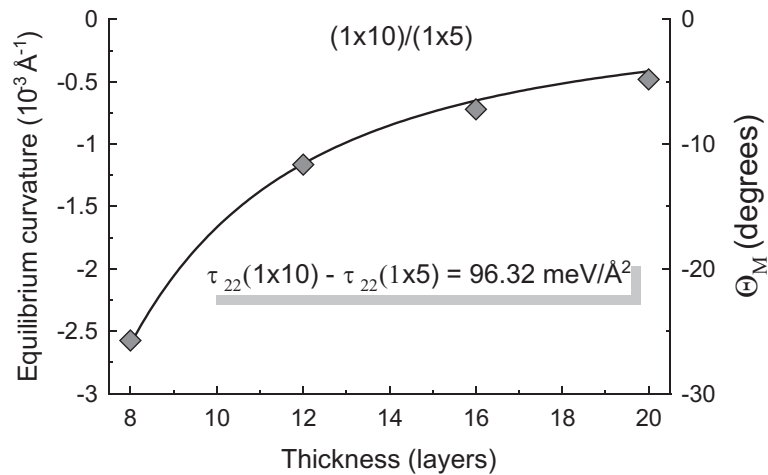


Figure 7.5: Dependence of the curvature upon thickness in the case of  $(1 \times 10)/(1 \times 5)$ . The inverse square dependence predicted by Stoney's equation is recovered, and the stress difference is extracted from the fit.

( $\sim 100 \text{ meV/\AA}^2$ ). We judge that the smallest surface stress difference detectable with our kind of simulation is of the order of  $10 \text{ meV/\AA}^2$ . This sensitivity should be very important in the study of phase transitions.

We have also verified the linear dependence of the curvature from the inverse square of the thickness predicted by equation (7.32). Figure 7.5 shows the fit with 8, 12, 16 and 20 layers, and the agreement is rather good.

### 7.4.3 Change of surface stress with adsorption

The surface stress is obviously a strong function of adsorption. As an example, we will consider here Pb on Au. Underpotential Deposition (UPD) [92] has been recently used together with STM techniques to exploit the formation of 2D phases of Pb on a substrate of Ag(100) and Au(100). Through different electrochemical potentials, one can obtain different phases, such as Au(100)- $c(2 \times 2)$  Pb, Au(100)  $c(3\sqrt{2} \times \sqrt{2}) R 45^\circ$  Pb, Au(100)  $c(6 \times 2)$  Pb. In particular, a close packed layer of lead shows a slight contraction in both  $[011]$  directions of the quadratic substrate lattice; the final structure is pinned to the substrate lattice at equivalent adsorption sites, leading to an Au(100)- $c(6 \times 2)$  moiré superstructure.

Using the potential in eq. (7.37), we found precisely this  $c(6 \times 2)$  superstructure as a local energy minimum, through quenching of a sample prepared with a perfect substrate of Au(100), and a triangular overlayer of Pb with the same

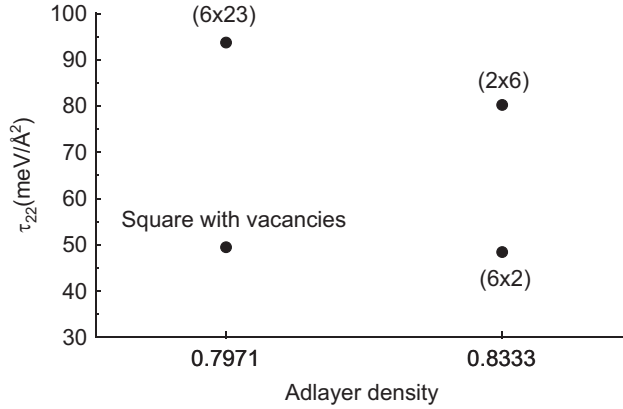


Figure 7.6: The surface stress component  $\tau_{22}$  for the Pb covered Au(100) surface in the for cases described in the text.

density of a bulk (111) layer. In the optimized structure, the  $(6 \times 2)$  pattern is evident (Figure 7.7(a)). Domain walls appear as the result of overlayer contraction. We were able to obtain a perfect  $(6 \times 2)$  (Figure 7.7(b)) by starting from an initial configuration with a denser overlayer. Deeper energy minima are obtained by the simple commensurate square overlayers with vacancies as in the case shown in Figure 7.7(c).

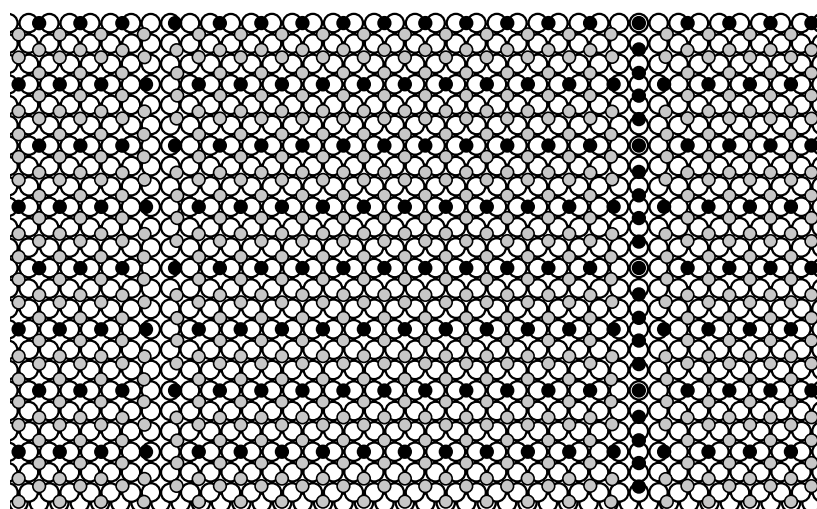
We performed variable curvature simulations on both the imperfect and the perfect  $c(6 \times 2)$ , and on the square overlayer with vacancies, with Au(100)  $(1 \times 4)$  as the reference ( $\tau_{22} = 147.52 \text{ meV}/\text{Å}^2$ ). For  $c(6 \times 2)$ , which is anisotropic, two different simulations were carried out in order to access separately  $\tau_{11}$  and  $\tau_{22}$  (the adlayer was rotated of 90 degrees, so as to keep  $\tau_{22}$  as reference).

These numerical results are summarized in Figure 7.6

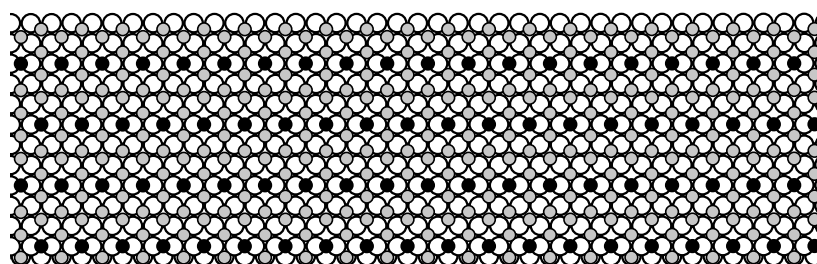
For the  $(6 \times 2)$  structure with domain walls we found  $\tau_{22} = 88.10 \text{ meV}/\text{Å}^2$  ( $\tau_{11}$  was not measured in this case), and for the perfect  $(6 \times 2)$  structure  $\tau_{11} = 72.41 \text{ meV}/\text{Å}^2$  and  $\tau_{22} = 38.52 \text{ meV}/\text{Å}^2$ . For the square structure with vacancies, we found  $\tau_{22} = 40.34 \text{ meV}/\text{Å}^2$ . The stress anisotropy is therefore large, and the effect of the domain walls is also remarkable.

## 7.5 Conclusions

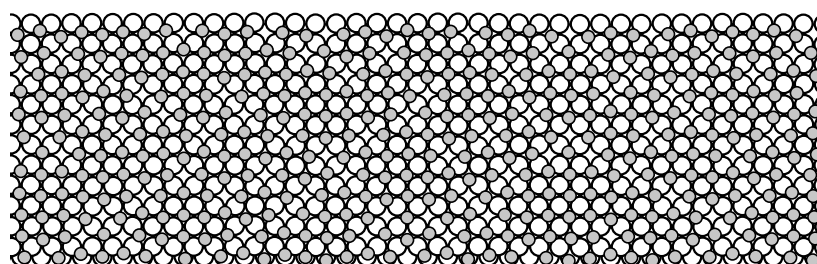
In this chapter we have introduced a variable curvature slab simulation method which represents a promising technique to study properties of crystal surfaces, in particular surface stress differences.



(a)



(b)



(c)

Figure 7.7: Different structures for the Pb overlayer (grey and black atoms) over a square Au(100) substrate (white atoms). (a):  $(6 \times 2)$  structure with domain walls. Black atoms are higher, two MD boxes are shown along  $x$ ; (b):  $(6 \times 2)$  without domain walls; (c) square adlayer with vacancies.

The first tests of the method, based on the comparison with known results, reveal a good accuracy, in the range of  $10 \text{ meV}/\text{\AA}^2$ , and easy applicability. We are now considering studies of a variety of phenomena, including surface phase transitions, using this approach.

## Appendix A. Interpretation of the fictitious kinetic energy of the curvature.

If the arc  $s_3 = 0$  is forced to have length  $L_y$  during the whole simulation, the volume  $\Omega$  of the sample is guaranteed to remain constant and equal to  $L_x L_y L_z$ . This is easily seen by performing the integral in polar coordinates.

The difference in surface area between upper and lower layer is of course:

$$\Delta A = L_x \left[ \theta_{MAX} \left( R + \frac{L_z}{2} \right) - \theta_{MAX} \left( R - \frac{L_z}{2} \right) \right] = L_x L_z \theta_{MAX} = L_x L_y L_z k = \Omega k. \quad (7.40)$$

The relative time variation of this area is

$$\frac{d}{dt} \left( \frac{\Delta A}{\bar{A}} \right) = \frac{V}{L_x L_y} \frac{d}{dt} k = L_z \dot{k} \quad (7.41)$$

Therefore, the fictitious kinetic energy term is:

$$\tilde{\mathcal{T}} = \frac{1}{2} W \dot{k}^2 = \frac{1}{2} \left( \frac{W}{L_z^2} \right) \left( \frac{d}{dt} \left( \frac{\Delta A}{\bar{A}} \right) \right)^2 = \frac{1}{2} \left( \frac{W}{\Omega^2} \right) \left( \frac{d}{dt} (\Delta A) \right)^2. \quad (7.42)$$

This result is simple but important because allows a connection with Andersen's constant pressure molecular dynamics [78]: whereas in Andersen's formulation the extra degree of freedom is the volume  $\Omega$  and the term  $\frac{1}{2} W \dot{\Omega}^2$  is the kinetic energy tied to volume variations, in this case there is a variation in the area difference between the two faces of the sample. The analogy could be brought further, adding to our Lagrangian a term  $-P k$ , which is the reversible work of a radial force decaying as the square of the curvature radius, acting identically on all particles, whereas the term  $-P \Omega$  in Andersen's formulation is the reversible work of the hydrostatic pressure during the variation of the cell volume. Such an external force, acting as a torque, could be used to force the equilibrium curvature to a different value from the one suggested by stress imbalance between the two surfaces. Applications of this point are presently under study.

## Appendix B. Constrained dynamics for fixing the center of mass

### 7.5.1 The velocity Verlet as a predictor-corrector.

Following [45], it is possible to cast a particular velocity Verlet algorithm as a predictor-corrector algorithm.

One can start from

$$\begin{aligned}\mathbf{r}_0(t + \delta t) &= \mathbf{r}_0(t) + \mathbf{r}_1(t) + \mathbf{r}_2(t) \\ \mathbf{r}_1(t + \delta t) &= \mathbf{r}_1(t) + \mathbf{r}_2(t) + \mathbf{r}_2(t + \delta t)\end{aligned}\quad (7.43)$$

where, as usual,

$$\mathbf{r}_n(t) = \frac{1}{n!} (\delta t)^n \frac{d^n \mathbf{r}_0}{dt^n}.\quad (7.44)$$

This can be written as a two stages predictor-corrector, with a force evaluation in between:

$$\begin{aligned}\mathbf{r}_0(t + \delta t/2) &= \mathbf{r}_0(t) + \mathbf{r}_1(t) + \mathbf{r}_2(t) \\ \mathbf{r}_1(t + \delta t/2) &= \mathbf{r}_1(t) + \mathbf{r}_2(t) \\ \mathbf{r}_0(t + \delta t) &= \mathbf{r}_0(t + \delta t/2) \\ \mathbf{r}_1(t + \delta t) &= \mathbf{r}_1(t + \delta t/2) + \mathbf{r}_2(t + \delta t)\end{aligned}\quad (7.45)$$

where  $\mathbf{r}_2(t + \delta t)$  is obtained by the equations of motion. In this case the predicted values for the positions coincide with the corrected ones, whereas the velocities are corrected (second-order, or three values, predictor-corrector).

When constraints are present, the forces acting on the  $i$ -th particle can be written as:

$$\mathbf{F}_i = \mathbf{f}_a + \mathbf{g}_a \approx \mathbf{f}_a + \mathbf{g}_a^{(x)}.\quad (7.46)$$

The constraints forces  $\mathbf{g}_a$  at each stage are approximated with  $\mathbf{g}_a^{(x)}$ , where  $(x) = r, v$ , so as to ensure that the positions and the velocities, respectively, satisfy the constraints, and the quantities at the various stages have to be corrected to keep into account the constraints forces.

### 7.5.2 The bent plate case.

In the case of varying curvature molecular dynamics, the bending leads to a drift towards the center of curvature of the center of mass. In order to fix the  $s_3$

component of the center of mass in the origin, the only constraint to be satisfied is (assuming all the particles to have the same mass for sake of simplicity)

$$\sigma \equiv \sum_{i=1}^N s_{3i} = 0 \quad (7.47)$$

where  $s_{3i}$  are the scaled coordinates in our curvilinear system (in this appendix,  $s$ ,  $\dot{s}$  and  $\ddot{s}$  are normalized according to (7.44)). The time derivative of the constraint equation gives a constraint on velocities:

$$\dot{\sigma} \equiv \frac{1}{\delta t} \sum_{i=1}^N \dot{s}_{3i} = 0. \quad (7.48)$$

The Lagrangian must then be completed with a term  $\lambda_R \sum_{i=1}^N s_{3i} + \lambda_V \sum_{i=1}^N \dot{s}_{3i}$ .

Two different approximations to the constraint forces have to be chosen so that positions and velocities satisfy the constraints exactly. In this particular case the forces turn out to be simple constants:

$$\begin{aligned} g_{3i}^{(r)} &= -\lambda_R \\ g_{3i}^{(v)} &= -\lambda_V \end{aligned} \quad (7.49)$$

The first equation, involving positions, is:

$$s_{3i}(t + \delta t) = s_{3i}(t) + \dot{s}_{3i}(t) + \ddot{s}_{3i}(t) - \frac{(\delta t)^2}{2m_i} \lambda_R \quad (7.50)$$

$\lambda_R$  has to be chosen in order to satisfy the position constraint at time  $t + \delta t$ :

$$\begin{aligned} \sum_{i=1}^N \left( s_{3i}(t) + \dot{s}_{3i}(t) + \ddot{s}_{3i}(t) - \frac{(\delta t)^2}{2m_i} \lambda_R \right) &= 0 \\ \lambda_R &= 2m_i \frac{\sum_{i=1}^N (s_{3i}(t) + \dot{s}_{3i}(t) + \ddot{s}_{3i}(t))}{N(\delta t)^2}. \end{aligned} \quad (7.51)$$

Therefore the former equation becomes:

$$s_{3i}(t + \delta t) = s_{3i}(t) + \dot{s}_{3i}(t) + \ddot{s}_{3i}(t) - \frac{\sum_{j=1}^N (s_{3j}(t) + \dot{s}_{3j}(t) + \ddot{s}_{3j}(t))}{N}. \quad (7.52)$$

The second equation, involving velocities, is:

$$\dot{s}_{3i}(t + \delta t) = \dot{s}_{3i}(t) + \ddot{s}_{3i}(t) - \frac{(\delta t)^2}{2m_i} \lambda_R + \ddot{s}_{3i}(t + \delta t) - \frac{(\delta t)^2}{2m_i} \lambda_V. \quad (7.53)$$

$\lambda_V$  must satisfy

$$\sum_{i=1}^N \left( \dot{s}_{3i}(t) + \ddot{s}_{3i}(t) - \frac{\sum_{j=1}^N (s_{3j}(t) + \dot{s}_{3j}(t) + \ddot{s}_{3j}(t))}{N} + \ddot{s}_{3i}(t + \delta t) - \frac{(\delta t)^2}{2m_i} \lambda_V \right) = 0$$

$$\lambda_V = 2m_i \frac{\sum_{i=1}^N (\ddot{s}_{3i}(t + \delta t) - s_{3i}(t))}{N(\delta t)^2}. \quad (7.54)$$

and the equation becomes

$$\dot{s}_{3i}(t + \delta t) = \dot{s}_{3i}(t) + \ddot{s}_{3i}(t) - \frac{\sum_{i=1}^N (s_{3i}(t) + \dot{s}_{3i}(t) + \ddot{s}_{3i}(t))}{N} \quad (7.55)$$

$$+ \ddot{s}_{3i}(t + \delta t) - \frac{\sum_{j=1}^N (\ddot{s}_{3j}(t + \delta t) - s_{3j}(t))}{N}.$$

## Chapter 8

# Molecular crystals: theory of surface rotational disordering

This Chapter is disconnected from all the previous ones. It deals with the disordering of a molecular crystal surface, and has been motivated by recent data by Modesti *et al.*[93] on the  $C_{60}$  (111) surface. It also differs in that we do not simulate, but rather build a mean-field theory.

The (111) fcc molecular crystal of  $C_{60}$  is well known to take place with a first order phase transition [94, 95] at  $T = 261K$ . Strikingly, the surface counterpart, apparently also first order, has been observed [93], with EELS and LEED measurements. It takes place at a temperature well lower than its bulk counterpart, *i.e.* at  $T = (225 \pm 3)K$ . In Figure 8.1 it can be seen the triplet exciton EEL spectrum, showing the abrupt character of the surface phase transition. In Figure 8.2, the intensity of the  $(1/2, 0)$  LEED spot versus temperature is shown. At  $T = 225 K$  there is the disappearance of the  $(2 \times 2)$  periodicity of the low temperature surface phase, and the surface becomes rotationally disordered.

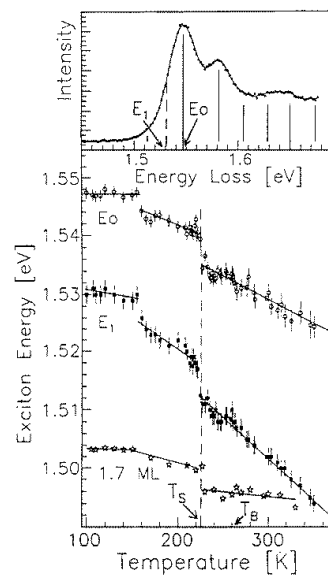


Figure 8.1: Fit to the triplet exciton EEL spectrum, showing the surface first order phase transition at  $T = 225\text{ K}$  (from [93]).

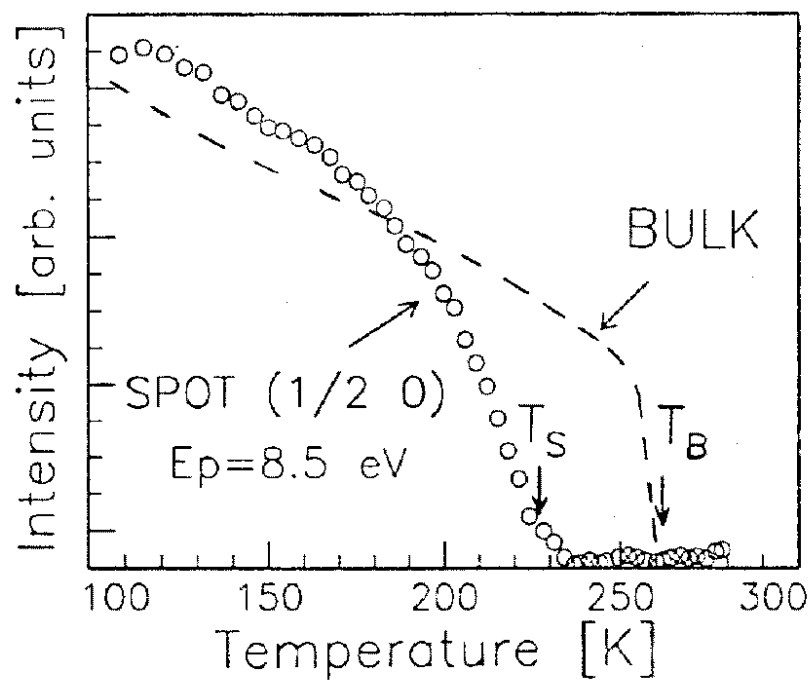


Figure 8.2: Intensity of the  $(1/2,0)$  spot vs temperature. The  $(2 \times 2)$  rotationally ordered structure of the surface disappears at  $T = 225\text{ K}$  (from [93]).

We present in this chapter a theory we developed in order to study surface phase transitions concerning rotational order in molecular crystals. For what concerns  $C_{60}$ , the conclusion of the theory is the disordering of the surface at a temperature which is in good agreement with the experimental one, whereas the order of the transition cannot be completely assured.

The starting point is a bulk theory of rotational order/disorder developed for crystalline  $C_{60}$  by Michel and coworkers ([96, 97]) which explains the bulk first order transition occurring at  $T = 260K$ .

Michel's model consists in a *fcc* lattice of molecules (truncated icosahedra) interacting through a first-neighbours potential depending on the orientational degrees of freedom;

$$\mathcal{V} = \frac{1}{2} \sum_{\mathbf{n}\mathbf{n}'} V(\mathbf{n}, \mathbf{n}'),$$

where  $\mathbf{n}$  and  $\mathbf{n}'$  are the orientations of two molecules and the interaction  $V$  is given by:

$$V(\mathbf{n}, \mathbf{n}') = \sum_P \sum_{A'A} V_{AA'}^P.$$

This expression consists in a sum of potentials between interaction centers on both molecules. The molecules are schematized as rigid bodies, with bond lengths extracted from experimental data and several kinds of interaction between atoms were included: repulsive, Coulombian and van der Waals- like (attractive).

After this, it is possible to expand the potential  $V$  in terms of Rotating Functions  $U$  which connect representations of the  $O_h$  group (cubic) and the identity representation of the group  $I_h$  (icosahedron) [96]:

$$V = \frac{1}{2} \sum_{\vec{n}\vec{n}'} \sum_{l,l'} \sum_{\tau,\tau'} J_{l,l'}^{\tau,\tau'}(\vec{n} - \vec{n}') U_l^{1,\tau}(\vec{n}) U_l^{1,\tau'}(\vec{n}') \quad (8.1)$$

$$(8.2)$$

where  $l$  is an angular momentum index (due to the high symmetry, concerning the low- $l$  terms, only  $l = 6, 10, 12$  terms are non-zero) and  $1, \tau$  indicate the identity representation of  $I_h$  and a particular representation of  $O_h$ , respectively.

A further refinement done by Michel and coworkers [98] was the diagonalization of the dynamical matrix of the problem, which brought to the following potential expansion:

$$\begin{aligned} V &= V_{RR} + V_{CF} \\ V_{RR} &= \frac{1}{2} \sum_{\vec{n}\vec{n}'} \sum_{m=1}^3 J_m(\vec{n} - \vec{n}') U_m(\vec{n}) U_m(\vec{n}') \\ V_{CF} &= \sum_{\vec{n}} \sum_l w_l U_l^{1A_{1g}}(\vec{n}); \end{aligned}$$

here  $U_m$  is a particular combination of rotator functions; moreover, a term with  $l' = 0$ , named *crystal field* was isolated; it corresponds to the interaction between a central molecule and its 12 nearest neighbours, the latter taken in spherical approximation. Because of the fcc structure assumed by the molecules in the high-temperature, almost-freely rotating (plastic) structure, this term has complete cubic symmetry: it has been therefore expanded in terms of rotating function belonging to the identity representation of  $O_h$ .

Michel's model has been shown to correctly reproduce a bulk first order transition between a rotationally ordered  $Pa_3$  phase and a rotationally disordered *fcc* phase. The low temperature phase corresponds to a simple cubic structure with a basis of 4 ordered sublattices (A, B, C, D), each of them with a ternary symmetry axis oriented along a different [111] cubic direction. In each sublattice the molecules are rotated of the same angle along that axis, yielding that orientation which is energetically more favourable: a pentagon in one molecule faces a 6 – 6 bond in the other molecule. In the *fcc* phase at  $T > T_{BULK}$  the four sublattices become rotationally disordered and indistinguishable. The role of the interaction  $V_{RR}$  is to break the symmetry between the sublattices.

## 8.1 Free energy, mean field and results

In this section we will describe the modifications which can be brought to Michel's model in the semi-infinite case, where the surface is a close-packed (111).

For this problem the so called ‘mean field’ hypothesis corresponds to consider the single molecule orientational distribution functions as *independent* of one another:

$$\rho(\omega_1 \dots \omega_N) = \prod_I \rho_I(\omega_I), \quad (8.3)$$

where  $\omega$  are the rotational coordinates of the single molecules. Having done this ansatz, and recalling that the two-body potential has been already factorized together with the rotation functions  $U_m$ , the free energy for the semi-infinite system can be written, neglecting intra-layer fluctuations, in the following way:

$$\begin{aligned} F = & \frac{N_L}{4} \sum_{k=1}^{\infty} \sum_{i=0}^3 \sum_{w \geq 1, w=k-1}^{k+1} \sum_{j \neq i} \frac{1}{2} J(2 - |w - k|) \text{Tr}(U_{m(i,j)} \rho_i^k) \text{Tr}(U_{m(i,j)} \rho_j^w) + \\ & + \frac{N_L}{4} \sum_{k=1}^{\infty} \sum_{i=0}^3 \text{Tr}(V_{CF}^k \rho_i^k) + \\ & + T \frac{N_L}{4} \sum_{k=1}^{\infty} \sum_{i=0}^3 \text{Tr}(\rho_i^k \ln \rho_i^k). \end{aligned} \quad (8.4)$$

In this expression,  $N_L$  is the number of molecules per (111) layer,  $i$  e  $j$  are two sublattices,  $k$  e  $w$  are layer indexes, ranging from 1 (surface) a  $\infty$  (bulk),  $\rho_i^k$  is the distribution function (factorized, as stated before, in the mean field approximation) of a molecule belonging to the  $i$ -th sublattice in the  $k$ -th layers;  $U_m$  are the particular combinations of rotating functions defined before:  $m$  can range from 1 to 3 with a dependence from  $i$  and  $j$  which is related to the particular symmetry of the *bulk* problem: the two body term  $V_{RR}$  has been left unchanged, neglecting surface relaxations.  $V_{CF}$  is the *crystal field* depending in this case on the layer:  $V_{CF}^1$  is the surface potential which is obviously different from  $V_{CF}^k$  with  $k \neq 1$ .

The traces  $\text{Tr}$  are defined as

$$\text{Tr}(A) \equiv \int_0^{2\pi} d\alpha \int_0^{\pi} d\beta \int_0^{2\pi} d\gamma \sin \beta A(\alpha, \beta, \gamma), \quad (8.5)$$

where  $\alpha$ ,  $\beta$  and  $\gamma$  are the Euler angles univocally identifying the molecule orientation.

At this point the free energy must be minimized, with the constraint that the functions  $\rho_i^k$  be normalized to 1; a necessary condition for an extremum is the stationarity with respect to the whole set of  $\rho$ :

$$\frac{\delta(F + \lambda_{i,k} \text{Tr}(\rho_i^k))}{\delta \rho_i^k} = 0 \quad \forall i, k, \quad (8.6)$$

where  $\lambda$  are Lagrange multipliers; this conditions lead to a chain of transcendental equations, defining in turn, implicitly, a chain of order parameters:

$$\eta_A^{(k)} = \frac{\int d\omega U_1(\omega) e^{-\beta G_1(k,\omega)}}{\int d\omega e^{-\beta G_1(k,\omega)}}$$

$$G_1(k, \omega) \doteq J((U_3(\omega) + U_2(\omega) - U_1(\omega)) (\eta_B^{(k-1)} + 2\eta_B^{(k)} + \eta_B^{(k+1)})) + V_{CF}^k(\omega)$$

$$\eta_B^{(k)} = \frac{\int d\omega U_3(\omega) e^{-\beta G_2(k,\omega)}}{\int d\omega e^{-\beta G_2(k,\omega)}}$$

$$G_2(k, \omega) \doteq J((U_1(\omega) + U_2(\omega)) (\eta_B^{(k-1)} + 2\eta_B^{(k)} + \eta_B^{(k+1)}) + -U_3(\omega) (\eta_A^{(k-1)} + 2\eta_A^{(k)} + \eta_A^{(k+1)})) + V_{CF}^k(\omega)$$

$$\begin{aligned} k &= 1 \dots \infty \\ \eta_A^{(0)} = \eta_B^{(0)} &= 0 \end{aligned} \quad (8.7)$$

with the boundary condition:

$$\lim_{k \rightarrow \infty} \eta_B^{(k)} = \lim_{k \rightarrow \infty} \eta_A^{(k)} = \eta_{BULK} \quad (8.8)$$

where  $\eta_{BULK}$  is the bulk value of the order parameter at temperature  $T$ .

The signs + and - appearing before the  $U_m$  allow to distinguish the different sublattices; in particular  $U_3 + U_2 - U_1$  denotes sublattice  $A$  whose order is described by the parameter  $\eta_A$ .

As it can be easily understood, three main difficulties are present at this stage with respect to the bulk problem:



Figure 8.3: (color) A molecule at the surface with its 9 first neighbours; if the central molecule belongs to sublattice A, 2 in-plane neighbours belong to B, 2 to C and 2 to D.

- due to the broken symmetry in the normal direction to the surface, the order parameter is now layer dependent;
- the crystal field changes for all molecules in the surface layer, which now have 9 neighbours instead of 12 (see Figure 8.3 ); we have subtracted from the bulk crystal field the contribution of the three upper neighbours absent at the surface: the resulting crystal field has a lower symmetry: Figure 8.4 shows the crystal field versus the rotation angle of a molecule around the  $[111]$  axis normal to the surface. In the bulk case, the equilibrium angle is the experimentally observed  $\theta_0 = 26^\circ$ ; it minimizes the bulk free energy at low temperatures. Due to minor coordination, the crystal field shows a maximum at the same angle  $\theta_0$ ; this ‘frustration’ encourages first layer disordering.
- two distinct order parameters are present at the surface: sublattice A, where the  $\{111\}$  molecular axis is perpendicular to the surface, is different from the other three sublattices ( $B, C, D$ ), where the  $\{111\}$  rotation axis forms an angle of  $\arccos(-1/3)$  with the surface normal (see Figure 8.5). We have therefore adopted two distinct order parameters ( $\eta_A$  and  $\eta_B$ ) for

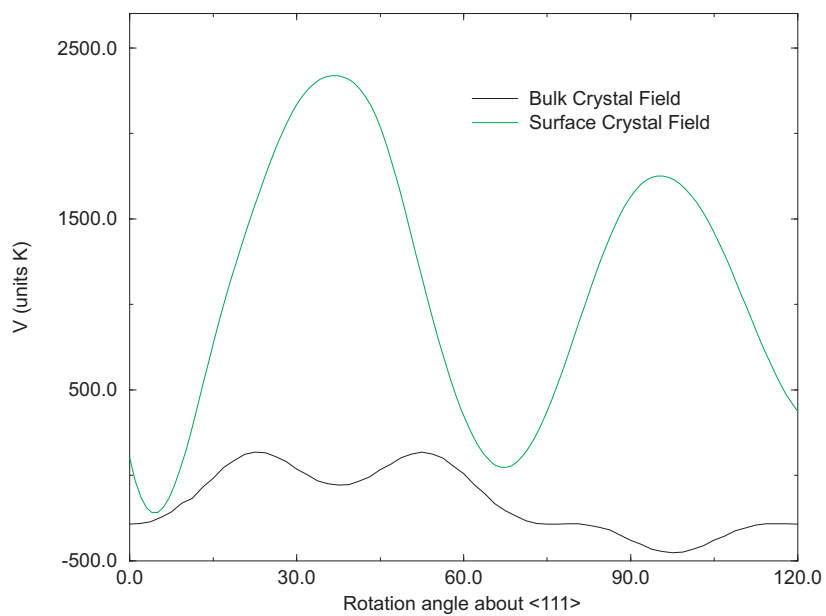


Figure 8.4: The crystal field in the bulk (lower line) and at the surface.

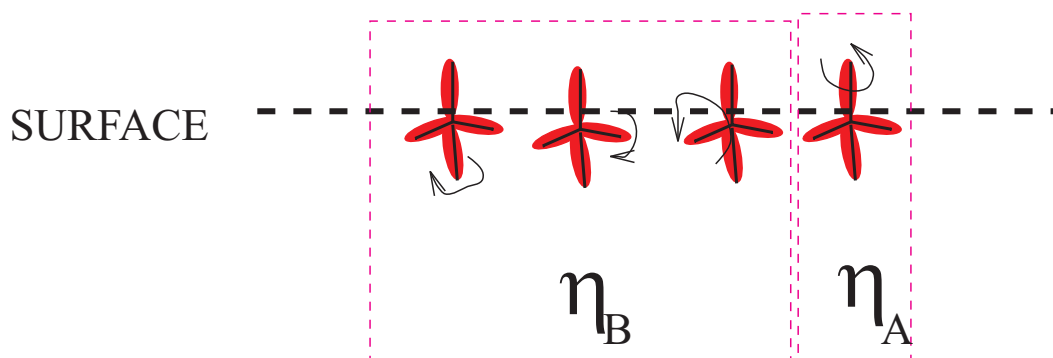


Figure 8.5: (color) The separation between two distinct order parameters at the surface.

each layer.

One should observe that even if only the surface layer is apparently affected by this symmetry breaking, the difference between  $\eta_A$  and  $\eta_B$  propagates to the inner layers, and only in the bulk limit the two parameters should coincide with the bulk value.

At this point it is possible to solve the chain of equations 8.7 using numerical methods; one starts with a pair of trial values for the parameters at the first layer; this is in turn sufficient for determining the whole chain of order parameter, at least implicitly; this trial will lead to a wrong value of  $\lim_{k \rightarrow \infty} \eta_X^{(k)}$ . By comparison of this value with the actual bulk order parameter the surface parameters are modified and a new trial is done until convergence is reached.

One of the difficulties of the problem resides in the extreme sensitivity to the surface values: variations of them smaller than 0.01% can induce fluctuation greater than 100% in the fourth or fifth layer.

An alternative method consists in assuming for the functions  $\rho_i^k$  an exponential form of the kind observed in (8.7), and then minimizing the free energy with respect to parameters  $\tilde{\eta}_A$  and  $\tilde{\eta}_B$  which will become the  $\eta_A$  and  $\eta_B$ , satisfying exactly (8.7) right at an extremum point.

It is possible to use simulated annealing method [99]; we have limited our calculations to four independent layers by fixing the fifth layer to the bulk value.

These two approaches allowed us to draw the following preliminary conclusions:

- the difference between the two order parameters at the surface is substantial: for example, for  $T = .75 T_{BULK}$ ,  $\eta_A^{(1)} \sim \frac{1}{6} \eta_{BULK}$ , whereas  $\eta_B^{(1)} \sim \frac{1}{2} \eta_{BULK}$ ;
- in the second layer both parameters are close to the bulk value, indicating that the disordering is almost completely a first layer phenomenon; this is in agreement with experimental data, which predict the surface transition even for a monolayer adsorbed on a substrate.
- the parameter  $\eta_A(1)$  drops until zero at  $T \simeq .84 T_{BULK}$ , a surface disordering temperature in reasonable agreement with experiments in  $C_{60}$ , where it takes place at  $\sim 0.9 T_{BULK}$  [93]

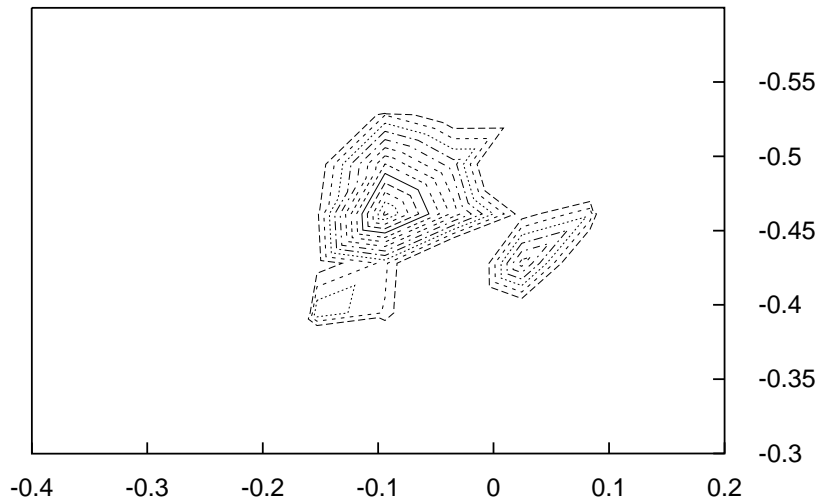


Figure 8.6: Level curves of a Monte Carlo run visiting statistics of local minima. The projection of the phase space on the bidimensional surface subspace is shown. There are at least two minima, indicating the possibility of a first order phase transition. The temperature is about  $0.75T_B$ . The bulk order parameter has an approximate value of  $-0.48$ . The parameter  $\eta_A$  is already depressed, while  $\eta_B$  is near the bulk value.

As an example of our calculation, we report the result of a Monte Carlo simulated annealing at a temperature of  $0.75T_B$  (Figure 8.6). Two distinct minima are present, and the order parameter  $\eta_A$  is already depressed. The bulk order parameter at this temperature is about  $-0.48$ . The negative sign of the bulk parameter is only due to particular parameterization chosen.

At present, we have as yet obtained no conclusive argument about the order of the transition. We would like to stress the role of the surface crystal field for at least two reasons: the subsequent separation of two distinct order parameters for each layer opens the possibility of several distinct paths towards the bulk, in analogy with *surface melting* [100], and therefore distinct minima in the free energy; moreover, the sublattice corresponding to  $\eta_A$  appears to be strongly disordered at the surface, and leads the whole first layer strongly towards the transition.

# Chapter 9

## Summary

We have considered in this thesis some topics concerning phase transitions occurring at the surfaces of crystals, mainly metallic, but including also rare gases and molecular crystals such as  $C_{60}$ .

For metallic surfaces the overall framework presented to the reader is varied: one ranges from the microscopic description of displacive reconstructions, such as the ones occurring at the Au(100) and (110) surfaces, the role of extended defects like steps, coming to a inspection of quantities accessible both experimentally and theoretically such as surface stress.

Concerning the reconstructed surface, the (100) face of gold undergoes orientational disorder through loss of coherence of locally hexagonally ordered domains.

The vicinal surfaces of this surface undergo faceting according to the phase separation curve described in Figure 3.20. We observed on these vicinals the step bunching, which is a precursor of faceting. The step on this surface has a particular behaviour due to the reconstruction of the zones left free by the shrinking of the step and to the deconstruction of the zones covered by it.

The density profile of a surface partially covered by another terrace (with

its step) shows a correlation length around the step. This correlation length has been connected with the critical growth of islands and craters on a reconstructed surface, whose onset is triggered by the structural changes of the zones under the islands or of the bottom of the crater. The influence of the island boundary over the deconstruction/reconstruction is measured by the above described correlation length, leading to a critical island/crater size of about 8/10 atoms.

This speculation leads to extending the results of King's group, concerning nonlinear growth of unreconstructed zones on  $O_2$ ,  $CO$  and  $H_2$  covered metallic surfaces, to the case of homoepitaxial growth, which we have mimicked in the canonical ensemble. Moreover, the connection between reconstructed and deconstructed zones has been also studied in a grand canonical framework to show the feasibility of our simulation methods, but we have not addressed dynamical growth simulations, which could in a future spread light on this interesting problem.

The Au(100) surface shows an interesting high temperature phenomenology ( $T < T_M$ ). Our evidences would lead to conclude that the high temperature state of this system is an incompletely melted (bilayer) surface; this structure does not explain, however, X-Ray data which would suggest a surface with incomplete coverage or, alternatively, a cumbersome high temperature return to the  $(1 \times 1)$  bulk structure.

The former hypothesis would lead to a sort of pre-roughening (PR) transition. We have no evidence of this scenario until now. Conversely, since the latter hypothesis would imply a change in the chemistry of gold at high temperatures, our glue potentials would not be able to predict a similar scenario. The discussion in this particular field is therefore open to further work and speculations in the future.

The PR framework has been studied in our group for the LJ(111) systems and two results have been found which are confirmed by experimental evidence. These two main results are the PR transition in the free surface case and the reentrant layering transition associated with preroughening in the substrate-adsorption case. The description of the latter, already available in the framework of lattice models, has been enriched with considerations about surface melting: the interplay between surface melting and preroughening is an interesting field of investigation for the future; we speculate, however, than the entropic term

---

lead by surface melting should bring to a lowering of PR temperature; moreover, the enriched scenario connected with this interplay could contribute to make the PR transition first order.

To address the different subjects of this thesis different tools have been used, which allowed to investigate a wide physical phenomenology.

Classical molecular dynamics (MD) in the canonical ensemble, with standard simulation algorithms, has been used as a tool to study the microscopic details of the hexagonal reconstruction on a flat (100) surface, the steps on the same surface, and the evolution and interplay with reconstruction of island and craters.

Particular periodic boundary conditions for studying a single step on a flat surface have been developed.

Grand canonical Monte Carlo simulations allowed to fix some aspects concerning phase transition with big density changes in metals; this method has been applied in our group to the reentrant layering transitions connected with pre-roughening in LJ rare gases, in particular Ar(111) crystals adsorbed on graphite and to the PR transition of the semi infinite crystal of the same kind.

Our assessment of the grand canonical MC as a method of surface simulation is positive: in our opinion, its peculiarities to be an off-lattice simulation method and to allow structural transitions involving density changes are precious and will yield interesting results for several physical systems in the future.

The framework of statistical mechanics within a mean field approach has been applied to the surface of a molecular crystal ((111) of  $C_{60}$  and to its rotational disordering. The broken symmetry along the surface normal has been kept into account explicitly by our model and the role of the so called “Crystal Field” in favouring the rotational disordering of the surface molecular lattice has been explained.

A new MD simulation method founded on an extended Lagrangian has been developed to describe the bending of a thin plate due to the stress difference between the two surfaces.

The idea sprang from two different sources: existing experiments carried out in the last few years and existing simulation methods developed for constant pressure simulation of bulk systems with a dynamically variable cell pioneered by Andersen and by Parrinello and Rahman.

Experimental method consists in the optical (or with STM) measuring of the bending angle of a slab whose two surfaces are different in some sense. To minimize its free energy, the slab bends towards a particular side, in order to extend the surface which has the largest tensile stress.

What we did was to extend to this geometry the same variable cell ideas used by Andersen and Parrinello-Rahman for bulk problems.

It sounded clear that a simulation which allow such a geometry would have allowed the connection between the dynamic microscopic aspects and experimentally available quantities.

The simulation techniques to which we inspired ourselves are those included in the variable cell and constant external pressure (stress) pioneered by Andersen and developed by Parrinello and Rahman.

One introduces additional degrees of freedom (accounting for variable cell geometry) which equilibrate with the atomic ones through the simulation. In our approach the only additional degree of freedom (we considered only the unidimensional bending) is the inverse of the curvature radius.

We have developed this method and we applied it to cases we could simply compare with elasticity theory and force integration formulæ. The first results are encouraging and we plan to adopt widely this technique in a set of interesting cases in the near future.

---

## Acknowledgments

Three years of SISSA... and four years of life, for an interruption due to conscientious objection in my home town. It is of course a long period through which I met different people, from whom I received support, friendship, joy and scientific skills, and for whom I hope to have been a good friend.

First of all, I want to thank Erio Tosatti. Ok, everybody thanks his supervisor at the end of the thesis, but wait... he has believed in me more than myself. It is to me still unclear whether I have to consider him a source of scientific wisdom or a friend; maybe a blend of the two. I often trusted his help when I was scared and discouraged, and I have always found an open door. He has a particular and very efficient way to transmit his opinion or his wishes, and who knows him needs no further explanation on this point! Living together with his strong voice in the nearest room is a, sometimes hard, but always stimulating experience.

Next, I thank Furio Ercolessi for teaching me the secrets of molecular dynamics simulations; simulation and physics are deeply connected, even if not everybody is convinced of it in the scientific community! I have learnt this lesson from my experience with Furio. Moreover, he has an enormous patience and he is always ready for a joke. His answers to my fears and doubts, especially during the first part of my PhD, have always been encouraging and calm.

My friend Franck Celestini deserves a mention for his work and help in the field of Monte Carlo simulation. His contribution to this thesis is fundamental.

Guido Chiarotti shares every problem and every success from the deep of his heart: he is a good friend, a researcher with the spirit of a student and the skills of a leader. I have appreciated, in particular, his support through the “hot” August, 1998!

Next, I thank all the other people who helped me on the scientific point of view: Giuseppe Santoro, Annalisa Fasolino, K. H. Michel, Silvio Modesti, Ugo Tartaglino, Giorgio Mazzeo and Andrea C. Levi (which deserves of course a special mention, since he has introduced me in the field of Surface Physics).

Continuing towards big friends, mArCo sAiTtA (I have written in this way, so he will not easily find his name in this chapter, when editing the file!), Antonino for the friends... friend and brother; we have started an enormous friendship four years ago, and there is no sign of decaying even through miles of oceanic water.

Alice Ruini is a wonderful friend and a wonderful person. She knows me so deeply, and I got so much help from her in these years.

Claudio Tebaldi has shared with true participation the first two years spent in Trieste both in Sissa and in “Villa Elena” (he is an outstanding physicist, too!).

Giovanni Fossati and Cecilia Clementi were my best friends in this last year of pieccdi (and so will be in ze fiucciur!), and we have shared (together with Chiara) amazing moments, giochs, naits, and suimin auars. Livin es e cappol in Sissa is not isi, and ai zinc ui ev elped iic ozer in overcamin difficultis.

*translation for literates:*

*Giovanni Fossati and Cecilia Clementi have been my best friends in this last year of PhD (and so will be in the future!), and we have shared (together with Chiara) amazing moments, jokes, nights, and swimming hours. Living as a couple in Sissa is not easy, and I think we have helped each other in overcoming difficulties.*

I thank also Carlo Cavazzoni, Stefano Tex Martinelli (with Daniela) and Franz Saija, valid home mates and friends, for their support.

A special thank goes to Franz Di Tolla, which I should include among the scientific collaborators, friends, room mates, system managers. He is one of the most independent person I ever met, and I consider him an example in several fields (“in verità !!!”). Moreover, if you ask Franz something, the question is not “Will Franz have time enough for my question?”, but “Will I have time enough for Franz’s answer?”; this gives an idea about his generosity.

I want to thank Nicola Manini for his kindness, Orion Ciftja (‘una forza della natura’) and Lu Zhong-Yi, my room mates two years ago, and all the people which contributed to make these years a agreeable period: in no particular order, Matteo Calandra, Sabrina Gustin with Pietro Donatis, Alessandro Laio (with whom I hope to continue a scientific collaboration), Lorenzo De Santis, Antonella Malatesta, Giannino Settanni, Marco Canepari, Marco Chiaberge, Davide Gabrielli, Valentina D’Odorico, Stefano e Paola Liberati Roncaglia, Stefano Lise, Stefano Giovanazzi, Antonio Trovato, Barbara Montanari, Leonardo Guidoni, Katia La Valle, and I apologize for possible oversights.

I thank Riccardo Iancer, Andrea Parma (Bibí and Bibó), Alexandra Meehan Porretti, Claudia Parma (Alice and Ellen Kessler) and all the secretariat ‘for their kindness and efficiency’ (of course) and for being so nice with boring

people (us!).

I also thank all the Computer Staff, in particular Fabio, Roberto, Luisa, Marina and Davide for their patience. A particular mention to the ‘problem solver’ Franco Viviani.

A special mention goes to Franco, Celide and Pepita for their great support.

Finally, I want to thank my family and my parents Alberto and Silvia for pluridecennial support, help and love, and I would like to remember in particular my grandfather Maurizio.

My last thoughts are for Chiara, the most limpid heart I ever met; she loved me continuously through these years, in spite of all difficulties. Her help was invaluable, and I bring it as a treasure in my mind; I will not seek here more needless words to express my inner feelings.



# Bibliography

- [1] B. N. J. Persson, Surf. Sci. Rep. 15(1992)1-135.
- [2] A. Hopkinson, Xing-Cai Guo, J. M. Bradley, and D. A. King, J. Chem. Phys. **99**(1993)1.
- [3] J. G. Kirkwood and F. P. Buff, J. Chem. Phys. **17**(1949)338.
- [4] D. Passerone, F. Ercolessi and E. Tosatti, Surf. Sci. **377-379**(1997)27.
- [5] F. Celestini, D. Passerone, F. Ercolessi and E. Tosatti, Surf. Sci. **402-404**(1998)886.
- [6] F. Celestini, D. Passerone, F. Ercolessi and E. Tosatti, to appear.
- [7] D. Passerone and E. Tosatti, Surf. Rev. and Letters 4(1997)859.
- [8] D. Passerone, E. Tosatti, G. L. Chiarotti and F. Ercolessi, submitted to PRB, preprint SISSA 60/98/CM/SS.
- [9] R. Car and M. Parrinello, Phys. Rev. Lett., **55**, 2471 (1985).
- [10] M. S. Daw and M. I. Baskes, Phys. Rev. B **29**, 6443 (1984).
- [11] M. W. Finnis and J. E. Sinclair, Phil. Mag. A **50**, 45 (1984); Phil. Mag. A **53** (Erratum), 161 (1986).
- [12] F. Ercolessi, E. Tosatti, and M. Parrinello, Phys. Rev. Lett **57** (1986) 719; F. Ercolessi, M. Parrinello, and E. Tosatti, Surf. Sci. **177** (1986) 314.
- [13] F. Ercolessi, M. Parrinello and E. Tosatti, Phil. Mag. A **58**, 213 (1988).
- [14] F. Ercolessi and J. B. Adams, Europhys. Lett. 26, 583 (1994).

- [15] H. S. Lim, C. K. Ong and F. Ercolessi, *Surf. Sci.* **269/270**, 1109 (1992).
- [16] M. Parrinello and A. Rahman, *J. Appl. Phys.* **52**(1981)7182.
- [17] F. Ercolessi, *PhD Thesis*, International School for Advanced Studies - Trieste (1987).
- [18] F. D. Di Tolla, *PhD Thesis*, International School for Advanced Studies - Trieste (1995).
- [19] N. W. Ashcroft and N. D. Mermin, *Solid State Physics*, (Rhinehart and Winston, Holt 1976).
- [20] K. W. Jacobsen, J. K. Nørskov and M. J. Puska, *Phys. Rev. B* **35**, 7432 (1987).
- [21] See, e.g., R. O. Jones and O. Gunnarson, *Rev. Mod. Phys.* **61**, 689 (1989).
- [22] P. Carnevali, F. Ercolessi, and E. Tosatti, *Phys. Rev. B(RC)***36**, 6701 (1987).
- [23] S. Hagstrom, H. B. Lyon, and G. A. Somorjai, *Phys. Rev. Lett.* **15** (1965) 491; D. G. Fedak and N. A. Gjostein, *Phys. Rev. Lett.* **16** (1966) 171; P. W. Palmberg and T. N. Rhodin, *Phys. Rev.* **161**(1967)586.
- [24] G. Binnig, H. Rohrer, Ch. Gerber, and E. Stoll, *Surf. Sci.* **144**(1984)321.
- [25] K. Yamazaki, K. Takayanagi, Y. Tanishiro and K. Yagi, *Surf. Sci.* **199** (1988) 595.
- [26] Y. F. Liew and G. C. Wang, *Surf. Sci.* **227** (1990) 190.
- [27] S. G. J. Mochrie, D. M. Zehner, B. M. Ocko, and D. Gibbs, *Phys. Rev. Lett.* **64** (1990) 2925; D. Gibbs, B. M. Ocko, D. M. Zehner, and S. G. J. Mochrie, *Phys. Rev. B* **42** (1990) 7330; B. M. Ocko, D. Gibbs, K. G. Huang, D. M. Zehner, and S. G. J. Mochrie, *Phys. Rev. B* **44** (1991) 6429.
- [28] D. L. Abernathy, D. Gibbs, G. Grübel, K. G. Huang, S. G. J. Mochrie, A. R. Sandy, and D. M. Zehner, *Surf. Sci.* **283** (1993) 260.

- [29] J. F. Annett and J. E. Inglesfield, *J. Phys.: Cond. Matt.* **1** (1989) 3645; N. Takeuchi, C. T. Chan, and K. M. Ho, *Phys. Rev. Lett.* **63** (1989) 1273; V. Fiorentini, M. Methfessel, and M. Scheffler, *Phys. Rev. Lett.* **71** (1993) 1051.
- [30] G. Bilalbegović and E. Tosatti, *Phys. Rev. B* **48**(1993)11240.
- [31] D. L. Abernathy, S. G. J. Mochrie, D. M. Zehner, G. Grübel and Doon Gibbs, *Phys. Rev. B* **B45**(1992)9272.
- [32] See, e.g., *Bond-orientational order in condensed matter systems*, K. Strandburg (Ed.), Springer, New York, 1992; K. Strandburg, *Rev. Mod. Phys.* **60**, 161 (1988).
- [33] A. Bartolini, *Ph.D. Thesis* and A. Bartolini, F. Ercolessi and E. Tosatti, *Phys. Rev. Lett.* **63**(1989)872.
- [34] R. Lipowsky, *Phys. Rev. Lett.* **49**(1982)1575.
- [35] R. Lipowsky and G. Gompper, *Phys. Rev. B* **29**(1984)5213.
- [36] R. Lipowsky, D. M. Kroll and R. K. P. Zia, *Phys. Rev. B* **27**(1983)4499.
- [37] N. C. Bartelt, T. L. Einstein and E. D. Williams, *Surf. Sci. Lett* **240**(1990)L591.
- [38] J. S. Ozcomert, W. W. Pai, N. C. Bartelt and J. E. Reutt-Robey, *Phys. Rev. Lett.* **72**(1994)258.
- [39] S. Song and S. G. J. Mochrie, *Phys. Rev. Lett.* **73**(1994)995.
- [40] G. Bilalbegović F. Ercolessi and E. Tosatti, *Europhys. Lett.* **17**(1992)333.
- [41] G. M. Watson, Doon Gibbs, D. M. Zehner, M. Yoon and S. G. J. Mochrie, *Phys. Rev. Lett.* **71**(1993)3166.
- [42] G. M. Watson *et al.*, G. M. Watson, Doon Gibbs, D. M. Zehner, M. Yoon, and S. G. J. Mochrie, *Surf. Sci.* **407**(1998)59.
- [43] Y. Samson *et al.*, *Surf. Sci. Lett.* **315**(1994)L969.

- [44] R. J. Phaneuf and E. D. Williams, Phys. Rev. Lett. **58**(1987)2563.
- [45] M. P. Allen and D. J. Tildesley, Computer Simulation of University Press, New York 1992.
- [46] L.A. Rowley, D. Nicholson and N. G. Parsonage, J. Comput. Phys. **26**, 66 (1975).
- [47] M. Mezei, Mol. Phys. **40**, 901 (1980).
- [48] A. Sokal, Monte Carlo methods, Troisième Cycle de la Physique en Suisse Romande, 1993.
- [49] N. Metropolis, A. W. Rosenbluth, M. N. Rosenbluth, A. H. Teller and E. Teller, J. Chem. Phys. **21**(1953)1087.
- [50] G. E. Norman and V. S. Filinov, High Temp. (USSR) **7**(1969)216-22.
- [51] see, *e.g.*, A. C. Levi, in *Phase Transitions and Surface Films 2*, Eds H. Taub, G. Torzo, H. J. Lauter and S. C. Fain, Jr. (NATO ASI series, Series B, Physics, v. 267), p. 327; L. Pietronero and E. Tosatti, Solid State Comm. **32**(1979)255.
- [52] H. Van Beijeren and I. Nolden, in *Structure and Dynamics of Surfaces II*, Eds. W. Schommers and P. von Blanckenhagen (Springer-Verlag, Heidelberg, 1987) p. 259.
- [53] K. Rommelse and M. den Nijs, Phys. Rev. Lett. **59**, 2578 (1987); M. den Nijs and K. Rommelse, Phys. Rev. B **40**, 4709 (1989).
- [54] G. B. Hess, in *Phase Transitions and Surface Films 2*, *op. cit.*, p. 357.
- [55] H. S. Youn and G. B. Hess, Phys. Rev. Lett. **64**, 918 (1990), H. S. Youn, X. F. Meng and G. B. Hess, Phys. Rev. B **48**, 14556 (1993).
- [56] P. B. Weichman, P. Day and D. Goodstein, Phys. Rev. Lett. **74**, 418 (1995).
- [57] S. Prestipino and E. Tosatti, Phys. Rev. B, accepted.

- [58] J. M. Phillips, Q. M. Zhang and J. Z. Larese, Phys. Rev. Lett. **71**, 2971 (1993), Comment on "Preroughening and Reentrant Layering Transitions on Triangular Lattice Substrates", Phys. Rev. Lett. **75**, 4330 (1995).
- [59] S. Prestipino, and E. Tosatti, Surf. Sci. **377-379**, 509, (1997).
- [60] C. S. Jayanthi, S. Prestipino, F. Ercolessi and E. Tosatti, Surf. Rev. and Letters **4**, 843 (1997).
- [61] B. K. Peterson and K. E. Gubbins, Mol. Phys. **62**, 215 (1987).
- [62] S. Prestipino, G. Santoro and E. Tosatti, Phys. Rev. Lett. **75**, 4468 (1995).
- [63] A. T. Pasteur, St. J. Dixon-Warren, and D. A. King, J. Chem. Phys. **103**(1995)2251.
- [64] T. Ali, A. V. Walker, B. Klötzer, and D. A. King, Surface Science, submitted.
- [65] J. J. Mortensen, T. R. Linderoth, K. W. Jacobsen, E. Lægsgaard, I. Stensgaard, F. Besenbacher, Surf. Sci. **400**(1998)290.
- [66] H. Ibach, Surf. Sci. Rep. **29**(1997)193.
- [67] L. Landau, Theory of Elasticity, Pergamon Press.
- [68] Paul A. Flinn, Donald S. Gardner, William D. Nix, IEEE Trans. on Elec. Devices **34**(689)1987.
- [69] R. E. Martinez, W. A. Augustyniak and J. A. Golovchenko, Phys. Rev. Lett. **64**(1990)1035.
- [70] C. E. Bach, M. Giesen, H. Ibach and T. L. Einstein, Phys. Rev. Lett. **78**(1997)4225.
- [71] H. Ibach, C. E. Bach, M. Giesen and A. Grossmann, Surf. Sci. **375**(1997)107.
- [72] A. Grossmann, W. Erley and H. Ibach, Surf. Sci. **337**(1995)183.
- [73] M. Foss, R. Feidenhansl, M. Nielsen, E. Findeisen, R. L. Johnson, T. Bulaps, I. Stensgaard and F. Besenbacher, Phys. Rev. B **50**(1994)8950.

- [74] A. Grossmann, W. Erley and H. Ibach, *Surf. Sci.* 313(1994)209.
- [75] A. Grossmann, Thesis, RWTH Aachen D80 (1996).
- [76] A. Grossmann, W. Erley and H. Ibach, *Surf. Rev. Lett.* 2(1995)543.
- [77] A. Grossmann, W. Erley, J. B. Annon and H. Ibach, *Phys. Rev. Lett.* 77(1996)127.
- [78] H. C. Andersen, *J. Chem. Phys.* 72(1980)2384.
- [79] G. G. Stoney, *Proc. R. Soc. London Ser. A* 82(1909)172.
- [80] The extension to potentials with angular dependence, such as Tersoff potentials, requires of course the derivation of more cumbersome equations of motion, but is in principle possible.
- [81] J. P. Ryckært, G. Ciccotti and H. J. C. Berendsen, *J. of Comp. Phys.* 23(1977)327.
- [82] H. C. Andersen, *J. of Comp. Phys.* 52(1983)24.
- [83] J. W. Gibbs, *The Scientific Papers of J. Willard Gibbs*, vol. 1 (Longmans-Green, London, 1906) p. 55.
- [84] C. Kittel, *Introduction to solid state physics*, 7th ed., Wiley, New York, 1996.
- [85] see, *e.g.* O K Rice, "Statistical Mechanics, Thermodynamics and Kinetics", (Freeman, San Francisco, 1967), ch. 13.
- [86] These potentials can be downloaded at the URL <http://www.sissa.it/~furio/potentials/>.
- [87] F. Ercolessi, O. Tomagnini, S. Iarlori, and E. Tosatti, in *Nanosources and Manipulation of Atoms Under High Fields and Temperatures: Applications*, NATO-ASI Series E, Vol. 235, ed. by Vu Thien Binh, N. Garcia and K. Dransfeld, (Kluwer, Dordrecht 1993), p. 185.
- [88] F. Ercolessi, M. Parrinello and E. Tosatti, *Philos. Mag. A*, 58(1988)213.

- [89] P. W. Palmberg and T. N. Rhodin, *J. Chem. Phys.* **49**(1968)134.
- [90] T. Hasegawa, N. Ikarashi, K. Kobayashi, K. Takayanagi and K. Yagi, in *Proc. II Int. Conf. on the Structure of the Surfaces*, Amsterdam 1987, ed. by J. F. Van der Veen and M. A. Van Hove (Springer, Berlin, 1988) p. 43.
- [91] F. Ercolessi, unpublished.
- [92] U. Schmidt, S. Vinzelberg and G. Staikov, *Surf. Sci.* **348**(1996)261.
- [93] A. Goldoni, C. Cepek and S. Modesti, *Phys. Rev. B* **54**(1996)2890.
- [94] R. Sachidanandam and A. B. Harris, *Phys. Rev. Lett. (Comments)* **67**(1991)1467; P. A. Heyney *et al.*, *Phys. Rev. Lett. (Reply)* **67**(1991) 1468.
- [95] W. I. F. David *et al.*, *Nature* **353**(1991)147.
- [96] K. H. Michel, J. R. D. Copley and D. A. Neumann, *Phys. Rev. Lett.* **68**(1992)2929.
- [97] K. H. Michel, *J. Chem. Phys.* **97**(1992)5155.
- [98] K. H. Michel and J. R. D. Copley, to be published on *Phys. Rev. Lett.*
- [99] A. Bosin, 'Minimizzazione di funzioni reali a molte variabili con il metodo del Simulated Annealing', Technical Report, Dip. Scienze Fisiche Università di Cagliari, 1993.
- [100] A. Trayanov and E. Tosatti, *Phys. Rev. Lett.* **59**(1987)2207.